QUANTUM DEGENERACY IN AN ATTRACTIVE BOSONIC
SYSTEM

A DISSERTATION
SUBMITTED TO THE DEPARTMENT OF PHYSICS
AND THE COMMITTEE ON GRADUATE STUDIES
OF STANFORD UNIVERSITY
IN PARTIAL FULFILLMENT OF THE REQUIREMENTS
FOR THE DEGREE OF
DOCTOR OF PHILOSOPHY

Mingchang Liu
September 2007

I certify that I have read this dissertation and that, in my opinion, it is fully adequate in scope and quality as a dissertation for the degree of Doctor of Philosophy.

_____

(Mark Kasevich)   Principal Adviser

I certify that I have read this dissertation and that, in my opinion, it is fully adequate in scope and quality as a dissertation for the degree of Doctor of Philosophy.

_____

(Alexander Fetter)

I certify that I have read this dissertation and that, in my opinion, it is fully adequate in scope and quality as a dissertation for the degree of Doctor of Philosophy.

_____

(Yoshihisa Yamamoto)

Approved for the University Committee on Graduate Studies.

Abstract

Bose-Einstein condensate (BEC) is a new state of matter formed by boson cooled very close to absolute zero. Since the first realization of BEC in 1995, there have been tremendous amount of experimental and theoretical studies on this phenomenon. A lot of new observations have been made and have extended people's understanding about quantum mechanics.

To achieve BEC state, one major approach is to use an efficient magnetic trap as the working horse for evaporative cooling, which is one of the key steps. A well-designed trap with good performance can make an experiment relatively easy and can also make some "impossible" possible. In our experiment, we designed and implemented a millimeter-scale Ioffe-Pritchard trap, Mini-Trap. This is not only a new instrument to achieve BEC but a novel concept since it is a different solution from the traditional gigantic magnetic trap and micro-trap.

It is well known that ^7Li is hard to approach BEC state. Its features like small collisional cross section, negative scattering length and absence of sub-Doppler cooling, bring a huge challenge on the experimental side. Yet, with our new mini-trap design, we were able to realize quantum degeneracy for Lithium. In this thesis we also present a simple double well implementation and collisional dynamics in such a trap. The capability demonstrated by Mini-Trap for Lithium scales well for other alkalic particles. Our versatile design and compact setup proved to be a good choice as a platform for a portable interference measurement system.

Lithium's unique feature of negative scattering length also makes a candidate for Schrodinger cat state. Schrodinger cat has been studied by photons, ions and superconductors. Atomic Schrödinger cat could be more interesting for research study and future applications because of the easy quantum control and extremely long coherence time.

The research explores the characteristics for ^7Li atoms in quantum degeneracy regime. And the study of the atomic Schrödinger Cat state is also another main subject for this thesis.

In the first chapter, I will explain and describe the basic theory and techniques for BEC research, followed by the apparatus design and setup in the second chapter. The third chapter contains the experimental measurements for single well and double well

in quantum degeneracy regime. Finally, theoretical discussion, experimental setup and preliminary data will be discussed for atomic Schrödinger cat state in the forth chapter.

Acknowledgement

I want to take this opportunity to express my gratitude to those who have supported, inspired, and encouraged me throughout my whole graduate study.

It has been a great privilege to work Prof. Kasevich. He has been both an advisor and a friend to me. His continuous support and guidance is the key for me to succeed.

Thanks to my lab mates, Olaf Mandel, Mike Minar, Nick Cizek, Ruquan Wang and Francesco Minardi, for their help and discussion during experiment. It is not desirable to work in a dark room day in and day out. However, these nice people has made it quite fun.

Thanks to those who have given me a lot of insights and technical help, including Peter Hommelhoff, Wei Li, Ari Tuchman, Grant Biedermann, Ken Takase, Catherine Kealhofer, Hui-Chun Chien, Xinan Wu, Nate Gemelke, Edina Sarajlic, Sheng-Wey Chiow.

To our secretary, Ping Feng. Her hard work has made my life much easier in last five years.

Many thanks to my colleagues in Prof. Kasevich's group, Prof. Chu's group and Prof. Bucksbaum's group and all my friends in Stanford. Thank you for being there for me.

I am greatly grateful to my parents and my family back in China for their love, care and support.

Thanks to Ron and Hanne,like my parents, they have been an important part of my life in last 5 years. Their love has been the sustaining power in both my life and my study.

Last but not least, special thanks to my beautiful and thoughtful wife, for her belief in me and refuse to give me up.

Contents

List of Tables

List of Figures

Chapter 1

Bose Einstein Condensation

1.1   A Brief History

Bose-Einstein condensate(BEC) was first predicted by Bose and Einstein in the 1920s [1]. After 70 years, it was finally realized in the mid-1990's with dilute gases [2, 3, 4]. As one of the milestones in atomic experiments, the success of the experiments not only confirmed quantum statistics in a new way but also opened the door to a new quantum regime where macroscopic behavior of millions of atoms can be studied in a relatively simple and easily controllable system.

During the many years of pursuing BEC, helium [5] and spin-polarized hydrogen [6] have been proposed to be the candidates. Due to the too strong interaction for helium and easy formation of molecules for hydrogen, their success waited until late 1990s [7]. It is the combination of laser cooling technology developed in the 1980s [8] and the evaporative cooling of magnetically trapped atoms in hydrogen experiment that makes Alkalis the best candidates for BEC experiment.

Since the birth of BEC, tremendous amount of experimental and theoretical breakthroughs have been achieved. This has devoloped people's understanding of quantum mechanics [9, 10, 11] and inspired research and application in atom optics and atom interferometry. For instance, the discovery of interference of BEC [12], BEC in optical lattice and squeezed state [13, 14], Mott insulator and phase revival [15, 16], BEC

with molecules [17], matter wave interference on a chip [18, 19], macroscopic tunneling and self trapping [20] ,bright soliton [21], vortex pining [22], superfluid phase transition [23], precise measurement of gravity with interferometry [24]...

1.2 Ground State Properties in Harmonic Trap

1.2.1 Bose Statistics
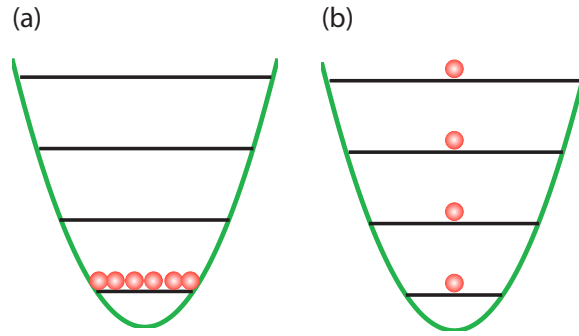
Figure 1.1: Quantum statistics. (a) Boson; (b) Fermion

Bosons are particles with integer spin, $0\hbar$, $\hbar$, $2\hbar$, $3\hbar$... while Fermions have half integer spin, $0.5\hbar$, $1.5\hbar$, $2.5\hbar$... At high temperature, their behaviors are like classical particles which satisfy Boltzmann distribution. When the temperature is low enough, their quantum behavior appears. For a system with discrete quantum state as in Fig. 1.1, the Bosons can stay on the same quantum level while Fermions will occupy different quantum state. This property makes it possible for macroscopic occupance of a single quantum state for Bosons. ^7Li, for instance, is a boson and ^6Li is a fermion.

Quantitatively the distributions for different particles can be written as [25]:

$$n_i = \begin{cases} \dfrac{1}{exp\left(\frac{\varepsilon_i - \mu}{k_B T}\right) - 1} & \text{Bose-Einstein distribution} \\[3ex] \dfrac{1}{exp\left(\frac{\varepsilon_i - \mu}{k_B T}\right) + 1} & \text{Fermi-Dirac distribution} \\[3ex] \dfrac{1}{exp\left(\frac{\varepsilon_i - \mu}{k_B T}\right)} & \text{Maxwell-Boltzmann distribution} \end{cases}$$

where n_i counts for average number of atoms that occupy state i with energy ε_i and μ is the amount energy needed to add one more particle to that state, which is often called chemical potential. In the limit of $\varepsilon_i = \mu$, n_i will diverge. This condition corresponds to a macroscopic occupance of that state.

Quantum statistics [25] predicts that for an ideal non-interacting gas in a three dimensional box, there is a critical temperature:

$$T_c = \frac{2\pi\hbar^2}{k_B m} \left(\frac{n}{2.612}\right)^{2/3}$$

where n is the density of the cloud.

According to wave-particle duality, an atom has an associated wavelength, the deBroglie wavelength:

$$\lambda_{dB} = \left(\frac{h^2}{2\pi m k_B T}\right)^{1/2}$$

If we define the phase space density(PSD), $\rho = n\lambda_{dB}^3$, then the critical condition can be written as:

$$\rho_c = n\lambda_{dB}^3 = 2.612$$

When temperature is lower than T_c or PSD is higher than ρ_c, the average distance among atoms is comparable with deBroglie wavelength. Phase transition will take place with macroscopic amount of atoms staying at ground state. This phase transition is called Bose-Einstein condensation(BEC).

In BEC experiments, dilute vapor is non-uniform and stored in a trap, which is normally harmonic. The critical temperature can then be calculated as [26]:

$$T_c = \frac{0.94\hbar\overline{\omega}}{k_B}(N)^{1/3}$$

where $\overline{\omega}$ is the geometric average of trapping frequency. For a BEC cloud with temperature T, the condensate fraction can be written as [26]:

$$\frac{N_{bec}}{N} = 1 - \left(\frac{T}{T_c}\right)^3$$

1.2.2 Dilute Gas

At the BEC temperature, the equilibrium state would be solid state. To observe BEC it is important to keep the system in the meta-stable gas phase where the 3 body recombination is a rare event and the gas phase can be sufficiently long. It is for this reason, the alkalis BEC is realized in dilute gases. The reduction of density is offset by the ultra-low temperature so that the PSD can be higher than the critical value.

Typically BEC cloud has a density of $10^{13} - 10^{15} \ cm^{-3}$. The density of air at room temperature is about $10^{19} \ cm^{-3}$ and the density of liquid and solid will be around $10^{22} \ cm^{-3}$.

In such a system, when the temperature is low enough, the major interaction among atoms is through S wave elastic collision, which is can be characterized by scattering length a [25]. The magnitude of a represents the strength of the interaction and the sign determines whether the interactions are effectively attractive $(a < 0)$ or repulsive $(a > 0)$. The weakness of this interaction ensures that to be used as a perturbation of the system Hamiltonian so that a mean field approach is possible.

1.2.3 GPE equation

Due to the interaction among atoms, the non-interacting wavefunction is not ground state for the system. The mean field potential links with scattering length by coupling constant $g = 4\pi\hbar^2 a/m$. The Schrödinger equation in an external field $V_{ext}(\overrightarrow{r}, t)$ can be written as [27, 28]:

$$i\hbar\partial_t \Psi(\overrightarrow{r}, t) = \left(-\frac{\hbar\nabla^2}{2m} + V_{ext}(\overrightarrow{r}, t) + g|\Psi(\overrightarrow{r}, t)|^2 \right) \Psi(\overrightarrow{r}, t) \qquad (1.1)$$

When thermal equilibrium is established, we can define $\Psi(\overrightarrow{r}, t) = \psi(\overrightarrow{r}) exp(\mu t/i\hbar)$ where μ as the chemical potential. We will then have

$$\mu\psi(\overrightarrow{r}) = \left(-\frac{\hbar\nabla^2}{2m} + V_{ext}(\overrightarrow{r}) + g|\psi(\overrightarrow{r})|^2 \right) \psi(\overrightarrow{r}) \qquad (1.2)$$

If the kinetic energy is small enough compared with the interaction energy,

$$|\psi(\overrightarrow{r})|^2 = n(\overrightarrow{r}) = \frac{\mu - V_{ext}(\overrightarrow{r})}{g}$$

This is called Thomas-Fermi approximation.

When $a > 0$, there will be a stable solution for equation 1.2. When $a < 0$, if the interaction term is too large, there will be no stable solution in a free space, BEC collapses even before it is formed. In a trap, the kinetic energy due to Heisenberg uncertainty can balance the attractive interaction so as to put an upper limit for number of atoms in BEC state. This number is numerically calculated to be [29]:

$$N_c \cong 0.57 \frac{\sqrt{\hbar/(m\overline{\omega})}}{|a|} \tag{1.3}$$

with $\overline{\omega}$ as the geometric average of trapping frequency for a harmonic trap.

1.3 Neutral atoms in magnetic field

1.3.1 Hyperfine structure

According to quantum mechanics, in the limit of weak magnetic field, the orbital angular momentum **L** for outer electron and its spin angular momentum **S** are good quantum numbers. The fine structure is the result of the coupling between **L** and **S**. Under the weak field assumption, **LS** coupling dominates. The total electron angular momentum is given as:

$$\mathbf{J} = \mathbf{L} + \mathbf{S}$$

where the coupled quantum number **J** has the value between $|L - S|$ and $L + S$. For ^7Li, $S = 1/2$. Since the ground state has the quantum number $L = 0$ we have $J = 1/2$. The first excited state has $L = 1$ so we have $J = 1/2$ and $J = 3/2$. In the external magnetic field, the value of J characterizes the energy level. The transition from $L = 0$ to $L = 1$ is called D line. $D1$ line is the transition from $J = 1/2$ to $J = 1/2$ and $D2$ line is from $J = 1/2$ to $J = 3/2$.

The same model applies to the hyperfine structure which is the coupling between total electron angular momentum $\mathbf{J}$ and the total nuclear angular momentum $\mathbf{I}$. The new coupled quantum number is defined as:

$$\mathbf{F} = \mathbf{J} + \mathbf{I}$$

where, as before, $|J-I| \leq F \leq J+I$. For ^7Li the nuclear angular momentum $I = 3/2$ so we have $F = 0, 1$ for $J = 1/2$ and $F = 0, 1, 2, 3$ for $J = 3/2$. The transition structure for Lithium atom is plotted in Fig. (1.2). In that figure we listed both the fine structure and hyperfine structure. Due to the fine and hyperfine coupling, the energy levels are shifted and split, which can be clearly seen in the figure. The amount of energy shift depends on the magnetic dipole momentum, electric quadruple momentum and quantum number of that state.
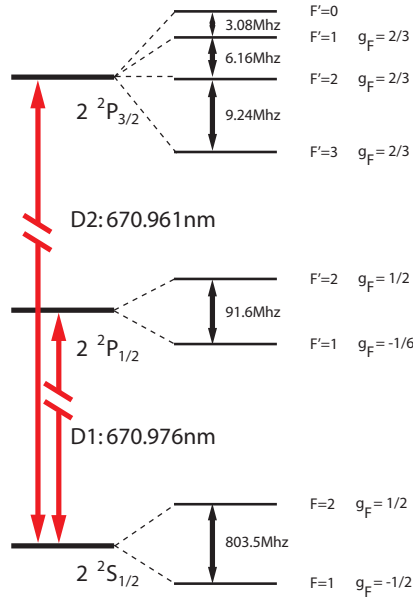
Figure 1.2: ^7Li transition line

For a typical BEC experiment, current commercial lasers can resolve the hyperfine transition. Although our dye laser only has 300kHz bandwidth, due to the natural

linewidth of the transition, it cannot resolve the excited state for D2 line. This imposes a lot of limitation on the experiment which we will discuss later.

1.3.2 Interaction with external static magnetic field

When the external magnetic field is zero, the hyperfine energy level is degenerate. The presence of magnetic field will break the degeneracy and split each hyperfine F state to $2F+1$ magnetic sub-level. The energy level shift induced by interaction with the external magnetic field, *anomalous Zeeman effect*, can be written as:

$$\begin{aligned}
\triangle E &= \frac{\mu_B}{\hbar}(g_S\mathbf{S} + g_L\mathbf{L} + g_I\mathbf{I}) \cdot \mathbf{B} \\
&= \frac{\mu_B}{\hbar}(g_S S_z + g_L L_z + g_I I_z) \cdot B_z
\end{aligned} \tag{1.4}$$

where we have assumed the direction of the local magnetic field is along z direction. $g_S \approx 2$, $g_L \approx 1$, g_I are the electron spin, electron orbital and nuclear "g-factor".

In the weak coupling limit, when the energy shift is smaller than fine splitting, J is a good quantum number to characterize the total effects of electron spin and orbital angular momentum. Equation (1.4) can be simplified as:

$$\triangle E = \frac{\mu_B}{\hbar}(g_J J_z + g_I I_z) \cdot B_z \tag{1.5}$$

where the *Landé factor* g_J can be calculated as [30]:

$$\begin{aligned}
g_J &= g_L \frac{J(J+1)-S(S+1)+L(L+1)}{2J(J+1)} + g_S \frac{J(J+1)+S(S+1)-L(L+1)}{2J(J+1)} \\
&\simeq 1 + \frac{J(J+1)+S(S+1)-L(L+1)}{2J(J+1)}
\end{aligned}$$

This form can be continuously simplified when the energy shift is smaller than the hyperfine splitting so that F is also a good quantum number. We then will simplify equation 1.5 as:

$$\triangle E = \mu_B g_F F_z B_z = \mu_B g_F m_F B_z \tag{1.6}$$

Where $m_F = F \times cos\theta$. Classically θ is the angle between magnetic momentum and magnetic field and it remains constant because of the fast processing of magnetic momentum around the magnetic field. In the quantum mechanics picture, this means

that during trapping the quantum number m_F is constant. The new *Landé* g_F can be similarly calculated by:

$$
\begin{aligned}
g_F &= g_J \frac{F(F+1)-I(I+1)+J(J+1)}{2F(F+1)} + g_I \frac{F(F+1)+I(I+1)-J(J+1)}{2F(F+1)} \\
&\simeq g_J \frac{F(F+1)-I(I+1)+J(J+1)}{2F(F+1)}
\end{aligned}
\tag{1.7}
$$

where the approximate that $g_J \gg g_I$ has been applied so that the second part of the calculation is ignored.

The g_F factor is calculated and listed in Fig. 1.2 for ^7Li. Equation 1.6 and 1.7 are used to approximate energy shift in the experiment.

1.4 Laser Cooling

Laser cooling relies on selectively exciting transitions for different atomic sub-state. Propagating direction, frequency and polarization of a laser beam are used to control the set up. It was proposed in the late seventies by Theodor W. Hänsch and Arthur Leonard Schawlow. 1980s observed great progress for laser cooling techniques: doppler cooling, sub-doppler cooling, sub-recoil cooling, Raman cooling, . . . Nowadays this matured technology lays the foundation for cold atom application and research.

1.4.1 Doppler Cooling

Figure 1.3: Simple doppler cooling scheme

The principle of doppler cooling can be simply illustrated by Fig. 1.3. Two counter propagating laser beams, which are red-detuned relatively to the atomic transition, shines on the atom. When an atom moves toward one of the beams, in the coordinate of the atom, doppler shift will move the frequency of that beam closer to resonance while the other beam farther out of resonance. This increases the probability to absorb

a photon opposite with the atom's moving direction. After the photon absorption, the atom will be in excited state, which will spontaneously decay with random direction. After many of such cycle, the average effect is that the atom absorbs a momentum kick $\hbar k$, which will slow the motion down. These two laser beams are called optical molasses.

The force of laser beam with detuning $\Delta = \omega - \omega_0$ on an atom traveling with speed v can be written as [31]:

$$F_{total} = \frac{\hbar k \Gamma}{2} \left[\frac{I/I_{sat}}{1 + I/I_{sat} + \frac{4}{\Gamma^2}(\Delta + kv)^2} \right] - \frac{\hbar k \Gamma}{2} \left[\frac{I/I_{sat}}{1 + I/I_{sat} + \frac{4}{\Gamma^2}(\Delta - kv)^2} \right] \quad (1.8)$$

where $k = \frac{2\pi}{\lambda}$ is the wave vector, Γ is the excited state natural linewidth, I is the intensity of the laser beam and

$$I_{sat} = \frac{hc\pi\Gamma}{3\lambda^3}$$

In low speed limit this can be written as:

$$\begin{aligned} F_{total} &= -\beta v \\ &= -\left(-4\hbar k^2 \frac{2I}{I_{sat}} \frac{2\Delta/\Gamma}{(1 + (2\Delta/\Gamma)^2)^2} \right) v \end{aligned} \quad (1.9)$$

The above calculation clearly shows that when the laser is red detuned, $\Delta < 0$ so that $\beta > 0$, there will be a restoring force for the atom as we have discussed in previous simple physics model.

During the laser cooling process, the atom performs a random walk in momentum space due to spontaneous emission. This constitutes a heating effect, which counteracts the cooling process and imposes a limit on the temperature to which the atom can be cooled with Doppler cooling. This temperature limit is called doppler temperature [32]:

$$T_{Doppler} = \frac{\hbar\Gamma}{4}$$

For all Alkalic isotopes, the ground state has more than one hyperfine states. During Doppler cooling, atoms at excited state may decay into the so-called dark state which will not absorb any photon. If all atoms are in dark state, the laser

cooling will cease. A repumping beam is normally needed in such a case to pump atoms out of such a state so that Doppler cooling can continue to work.

1.4.2 Sub-Doppler Cooling

To cool atom below the Doppler temperature, sub-Doppler cooling, also called "sisyphus cooling", can be used. For this kind of cooling, optical pumping among ground states of multi-level is spatially dependent. This is normally realized by polarization gradient. It can also be achieved by a standing wave with constant polarization in a magnetic field. The direction of the bias magnetic field is different from the quantum axis defined by the polarization of light field. In both cases, moving atom responses non-adiabatically to the light field. During optical pumping, light is absorbed at lower frequency than the spontaneous emission so as to dissipate energy to the radiation field [33, 34].

Sub-Doppler cooling can cool atoms down to $10\mu K$ level but it doesn't work well for Lithium. The linewidth of cooling transition between $|2,2\rangle$ and $|3,3\rangle$ is $\Gamma/2\pi = 5.9 Mhz$ while in Fig. 1.2, we can see that the excited state of Lithium cannot be well separated with such an optical light. This means that optical pumping, the key driver for sub-Doppler cooling, will not work well easily for Lithium.

1.5 The optical dipole trap

Laser cooling can slow atoms down but it cannot store them. Most of trapping scheme for neutral atoms are magnetic trapping, optical trapping or combination of both. Magnetic trapping arises from interaction between permanent magnetic dipole momentum of atoms and external magnetic field. We will discuss this in next section. Optical trapping is realized by the dispersive interaction between induced atomic electric dipole momentum and the intensity gradient of the light field [31].

There are two kinds of optical forces, radiative and dipole. Radiative optical trap [35] can only be set up with optical pumping between different sub-levels of complicated atoms. It can be quite deep while its attainable temperature and density

are also limited due to the resonant light field. Optical dipole trap [36], on the other hand, is realized with far-off-resonance light(FORT). The potential in such trap is conservative and all internal states of atoms can be trapped. With the far-detuned light, the excitation photon-scattering is extremely low so that it does not have the limitation as radiation-pressure traps. The price pays for such a good feature is that the optical dipole trap is normally very shallow compared with radiative optical trap.

The potential and scattering rate for an optical dipole trap can be calculated by considering the atom as a simple oscillator in the classical radiation field of laser light or using dressed state picture. The potential of a ground state with total angular momentum F and magnetic quantum number m_F can be written as [37]:

$$U_{dip}(\mathbf{r}) = \frac{\pi c^2 \Gamma}{2\omega_0^3} \left(\frac{2 + P g_F m_F}{\Delta_{2,F}} + \frac{1 - P g_F m_F}{\Delta_{1,F}} \right) I(\mathbf{r}) \tag{1.10}$$

where Γ is the natural linewidth, ω_0 is the transition frequency, $\Delta_{2,F} = \omega - \omega_{D2}$ and $\Delta_{1,F} = \omega - \omega_{D1}$ is the detuning with respect to D2 and D1 line, and $P = 0, \pm 1$ for linearly and circularly $\sigma^\pm$ polarized light respectively. This is valid as long as optical detunings are large compared with excited state hyperfine spilt.

When the detuning is much larger than the fine split $|\Delta F, 1|, |\Delta F, 2 \gg \Delta'_{FS}$, consider detuning Δ with respect to D-line doublet, we will have approximately:

$$\begin{aligned} U_{dip}(\mathbf{r}) &\approx \frac{3\pi c^2 \Gamma}{2\omega_0^3 \Delta} \left(1 + \frac{1}{3} P g_F m_F \frac{\Delta'_{FS}}{\Delta} \right) I(\mathbf{r}) \\ &\approx \frac{3\pi c^2 \Gamma}{2\omega_0^3 \Delta} \end{aligned} \tag{1.11}$$

We can see that when the detuning greatly exceeds fine splitting, all magnetic sub-states see roughly the same trap. The scattering rate for such large detuning can also be calculated to be [37]:

$$\begin{aligned} \hbar \Gamma_{sc} &= \frac{\Gamma}{\Delta} U_{dip} \\ &\Longrightarrow \\ \Gamma_{sc} &= \frac{3\pi c^2}{2\hbar \omega_0^3} \left(\frac{\Gamma}{\Delta} \right)^2 I(\mathbf{r}) \end{aligned} \tag{1.12}$$

From equation 1.11, we can see that when the laser is red detuned relative to the atomic transition, $\Delta < 0$, the potential is negative. In such a case, the interaction will attract atoms to the potential minima with maximum intensity. When $\Delta > 0$, the potential is repulsive and the interaction will repel the atom away from intensity maximum.

For a single gaussian shape beam with beam waist w_0 we have:

$$I(\mathbf{r}) = I_0 \frac{exp\left[-\frac{2r^2}{w(z)^2}\right]}{1 + \left(\frac{z}{z_R}\right)^2}$$

where z and r are the longitudinal and radial coordinate, $z_R = w_0^2 \pi / \lambda$ $w(z) = w_0\sqrt{1 + (z/z_R)^2}$. If the laser power is P, we have $I_0 = 2P/(\pi w_0^2)$.

When we know the power of a gaussian beam, using equation 1.11 and 1.5, we can calculate the trap potential.

1.6 Magnetic trapping

The trapping force of a magnetic trap comes from the interaction with non-uniform static magnetic field. This means that we can design trapping configuration to provide such kind of non-uniformity.

According to the Maxwell equation, the divergence of static magnetic field is zero. This means that there will be no magnetic maximum in the free space. So a static magnetic trap can only trap a weak field seeking state. By equation 1.6 we can conclude that only the states with $g_F m_F > 0$ can be possibly trapped.

Since only the weak field seeking states can be confined in a static magnetic trap, if the atom makes a transition to a strong field seeking state during the trapping it will get lost. When the atom moves inside a trap, it will see changes of magnetic fields. The trapping can only be stable when the atom's magnetic momentum can follow the directional change of the magnetic field. So we have the adiabatic condition:

$$\frac{d\theta}{dt} < \frac{\mu_m |\mathbf{B}|}{\hbar} = \omega_{Larmor} \tag{1.13}$$

where is the change of the field direction and μ_m is the magnetic momentum. $d\theta/dt$ has the trapping frequency as the upper bound. From this equation we can see that the amplitude of magnetic field for a stable trap has to be big enough so that the *Larmor* frequency is higher than the trapping frequency. The loss when the amplitude of magnetic field is close to zero is called "Majorana flops".

For an atom trapped inside a magnetic trap, when the adiabatic condition is satisfied, the particle remains in the Zeeman sub-level. This means that the spin is always aligned with the local magnetic field so that B_z in the equation 1.6 is actually the magnitude of the trapping field. This is important when we consider the design of a new trap.

1.7   Magneto-Optical Trap(MOT)

MOT is one of the most important inventions for cold atom research. Combining laser cooling and magnetic trapping concept, MOT makes it possible for people to study spatially trapped cold atom ensemble. For BEC experiments, MOT collects atoms from the vapor environment and performs initial cooling.

Mechanics for MOT to work is demonstrated in Fig. 1.4. For simplicity, let's consider a tow-level system with $F = 0$ as ground hyperfine state and $F = 1$ as the excited state. The 1-D cross section of the configuration is also shown on the figure. Z axis is the quantum axis along which the laser polarization and magnetic quantum number m_F are defined. The magnetic field is defined to be positive when it is aligned with the z axis.

Let's focus on the regime where $B > 0$ in Fig. 1.4(b). For an atom in magnetic sub-state $m_F = 1$, when it moves along Z axis, it feels the restoring force from the magnetic trap since its potential energy will rise up. For an atom in the sub-state $m_F = -1$, when it also moves along Z axis, it will get closer to be on resonant with the red detuned laser beam due to Doppler shift. Since σ^-/σ^+ will drive the transition of $\Delta m_F = -1/\Delta m_F = 1$, there is more probability that the atom will absorb a photon from σ^- beam than from σ^+ beam. The momentum transferred by the photon will push the atom back to the center of the trap. This is like a restoring force too. The
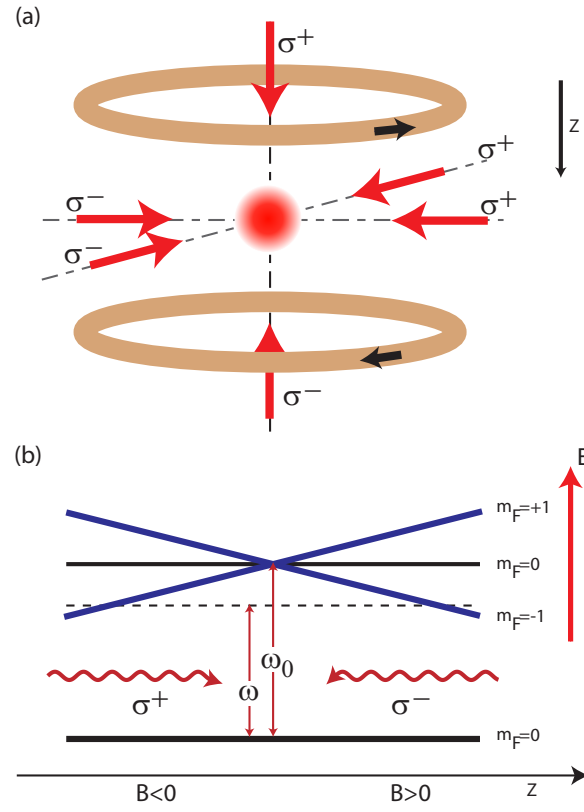
Figure 1.4: MOT setup. (a) 3D configuration; (b) 1D cross section along Z axis. ω_0 is the atomic transition frequency and ω is the red-detuned MOT laser frequency.

similar argument applies to the regime where $B < 0$. In both regimes, there are restoring force to trap atoms.

It is easy to extend our argument to 3D and to more complicated transitions where $F_g \to F_e = F_g + 1$.

The first MOT was demonstrated in 1987 [38]. A typical MOT has a capture range of $10m/s$ which corresponds to roughly $10mK$. A MOT normally traps 10^9 atoms with temperature of a few hundred μK. Due to the closeness of laser frequency to transition frequency, the temperature cannot be driven arbitrarily low. Its phase space density is normally about 10^{-6}. It is not possible to achieve BEC in a MOT.

1.8 Evaporative cooling
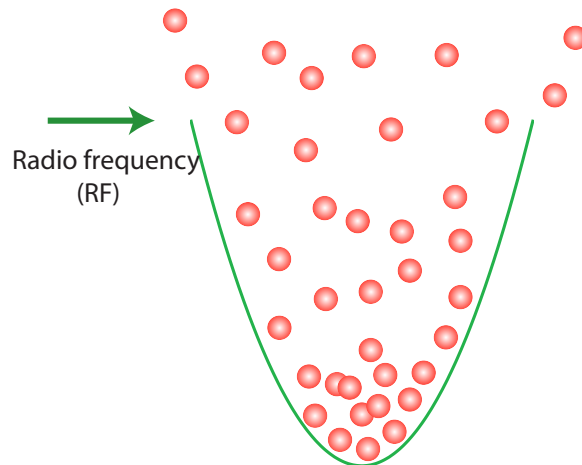
Figure 1.5: RF forced evaporative cooling for trapped atoms

Laser cooling itself cannot improve the phase space density for atomic cloud to BEC regime. When the cloud is dense enough, the scattered photon could be absorbed by other atoms before escaping so that we will cannot lower the ensemble's energy. On the other hand, the presence of excited state will increase inelastic collisions which will generally heat the cloud and produce atom loss. The way out is to use evaporative cooling.

1.8.1 How does evaporative cooling work

The evaporative cooling depends on removal of the atoms with higher-than-average energy from the thermal distribution spectrum. The atoms left will re-thermalize to a lower temperature due to elastic collisions. This can be achieved by continuously lower the trap depth by moving RF level which has been shown in Fig. 1.5. The atoms with higher energy will be RF-flipped to un-trapped state and get lost. The process is called forced evaporative cooling. The RF cut energy level and cloud temperature has the relation $E_{cut} = \eta k_B T$, where η is typically between 5 and 10.

A few assumptions are made for evaporative cooling [39]:

- Motion of atoms is sufficiently ergodic and gas can be described by classical statistics

- Temperature of cloud is low enough so that only S-wave collision [40] is possible with collision cross section $\sigma = 8\pi a^2$ where a is the scattering length.

- Thermalization is much faster than the speed of cooling

The speed of evaporation is important for efficient cooling. If the cutting speed is two fast, there is no time for the cloud to re-thermalize. The cooling efficiency will be low. Experimentally it was shown that at least 2.7 collisions per second are necessary for re-thermalization [41]. If the cutting is too slow, very long trapping lifetime is required, which could be experimentally impossible. Experimentally, η is normally kept at constant.

For Alkali atoms in a trap, the major loss is background collision. As we said, evaporation replies on elastic collisions with rate $\gamma elastic = \bar{n}\sigma v$ where $\bar{n}$ is the average density of the cloud and v is the mean velocity. let's define $R = \gamma_{elastic}/\gamma_{loss}$ as the ratio of good to back collisions. γ_{loss} is the rate for loss rate due to background collisions and $\gamma_{loss} \approx 1/\tau_{trap}$ with τ_{trap} as the trapping lifetime. It is pointed out in [42] that there is a minimum, roughly 200, for R. When R is higher than the minimum, the system can stay in "runaway" regime where evaporation is in constant or increasing collision rate. Generally, the tighter trap and the longer trapping lifetime, the better chance to get into "runaway" evaporation.

1.8.2 Loss in a magnetic trap

Although the background collision is the major loss channel, it is not the end of story. Several other losses in the magnetic trap, which is what we will use for evaporation cooling, could also hurt the experiment [43].

- Majorana flops loss, An atom could flip state when it goes through magnetic zero. This can be reduced by using non-zero magnetic field.

- Spin-exchange collision loss. Atom can exchange angular momentum during collision, which may produce un-trapped states. For instance, collision of two $|2,1\rangle$ atoms could produce $|2,2\rangle$ and $|2,0\rangle$ or $|2,2\rangle$ and $|1,0\rangle$. Both $|2,0\rangle$ and $|1,0\rangle$ are un-trapped states. Even worse, the hyperfine energy released by the pair $|2,2\rangle$ and $|1,0\rangle$ will heat up the cloud. Fortunately, this can be avoided by using doubly polarized spin state.

- Three body collision loss. At a very high density, two-atoms collision can form a molecule and the excess energy is absorbed by a third atom. This also leads to loss and heating. The probability for this kind of event is proportional to n^2

- Dipolar collision loss. This is due to magnetic dipole-dipole interaction, which has less severe selection rules like spin exchange. Lower hyperfine multiplet has less probability for this kind of loss due to Fermi Golden rule. It is linearly dependent on the cloud density n.

1.9 Quantum degeneracy for Lithium

As an Alkali, ^7Li was one of the first few candidates to achieve BEC. It seems to be a good choice because ^6Li, which is Fermion, has almost identical energy level. It would save a lot work to trap the two isotopes with similar optical set up. It turns out that achieving quantum degeneracy for ^7Li itself is much harder than other atoms like ^{87}Rb. Here we will talk about the reasons for that and what we want to do with ^7Li.

1.9.1   Properties of Lithium

As we have discussed during magnetic trapping, only weak field seeking state can be magnetically trapped. From Lithium's energy level, Fig 1.2, the magnetic sub-state that can be trapped are $|2, 2\rangle$, $|2, 1\rangle$ and $|1, -1\rangle$. Our discussion for loss in magnetic trap shows that only doubly spin polarized states are not suffered from spin exchange loss so that $|2, 2\rangle$ and $|1, -1\rangle$ are then the only two choices for magnetic trapping.

BEC can be achieved by laser cooling followed by evaporation cooling. Since sub-Doppler cooling cannot apply to Lithium, the initial condition for evaporation cooling is with high temperature and low phase space density. On the other hand, evaporative cooling depends on elastic collision rate which is proportional to S wave collision cross section $\sigma \propto a^2$. For $|2, 2\rangle$ state, $a = -27a_0$, where $a_0 = 0.5nm$ [44]. For $|1, -1\rangle$, $a = 5.1a_0$. These values are much smaller than what are available for Rubidium, Cesium and etc.

The limit of collision-cross-section is the key reason for the difficulty to achieve BEC for Lithium. As we discussed in evaporative cooling. There is a minimum requirement for good to back collision ratio, R, which should be at least around 200 for run-away. For small collision-cross-section species, it is only possible to either use tight confinement to increase elastic collision rate or use ultra long trapping lifetime to reduce inelastic collision rate. Prof. Hulet from Rice University used permanent magnetic trap with a trapping lifetime of 5 minutes. Even with such a device, it can only work with $F = 2$ state but not $F = 1$ state. We are looking for a trapping scheme that can provide good trapping confinement and long trapping time.

Now the only ground state we can choose is $|2, 2\rangle$. Although it also has small collision cross section σ, that is still 25 times larger than $|1, -1\rangle$, which is impossible for direct evaporation to work. We will discuss at the end of the thesis that it could be possible to achieve BEC at $|1, -1\rangle$ state. This could be done by spin-flip $|2, 2\rangle$ to $|1, -1\rangle$ at the end of evaporation of $|2, 2\rangle$ when phase space density is high enough.

It is possible to increase the elastic collision rate by tightly confining the atoms. This will normally heat up atom cloud. For $|2, 2\rangle$ state, the collision cross section drops down to zero when the temperature is at $6.6mK$ [43] due to the negative sign of scattering length for this state. This negative sign also limits the number of atom

that can be in BEC state as we have discussed before.

In a summary, to achieve BEC for Lithium with evaporative cooling, we need a magnetic trap that has large volume and trap depth so that we can load more atoms into it for evaporation. The trapping frequency should be high enough so the cloud can be reasonably compressed to increase the collision rate. It is also important to have long trapping lifetime.

1.9.2   single well and double well

Pursuing quantum degeneracy is a hard task for Lithium. On the other hand, our capability to do that with our apparatus, especially our magnetic trap, marks great achievements. If our system can work well for Lithium, it scales well for other Alkalis like Rubidium and Sodium.

At the same time, using a versatile combination with a optical dipole trap, we will see that a double well can be realized because of the excellent optical access of the apparatus. Such a system can achieve a textbook-simple atomic-Schrödinger-cat state due to attractive interaction for $|2, 2\rangle$, which we will discuss in the last chapter. On the other hand, a double well is a simpler system than multi-well like optical lattice for theoretical model and calculation.

Chapter 2

Experimental apparatus

In this chapter we will present the apparatus set up, some of the key techniques used in the experiment, design and realization of a unique magnetic trapping scheme—Mini-Trap. The last part is the main discussion.

2.1 Vacuum system

Good vacuum system is critical for BEC experiments. Although creating and maintaining an ultra-high vacuum system has been a mature technology, it is still a challenging job which needs extra care at the beginning of the experiment. A good design is the starting point and attention to details is required.

2.1.1 A two-chamber system

Most newly designed BEC experiments would apply a double-chamber scheme if possible, although it is more complicated. The reason is to keep a high vapor pressure area to collect more atoms for MOT while maintain a high vacuum area for better trapping lifetime to create BEC. The high vacuum chamber is normally called science chamber.

For Lithium, unlike Rubidium, it's vapor pressure under room temperature is too low for MOT to work. Actually since Lithium's melting point is $180.54^{o}C$, we have

(a) trimetric side view

Diode ion pump

Precooling
cube

Small
ion pump

Science
chamber

Triode ion pump

(b) top view

Lithium
source

negative
current lead

Positive
current lead

Differential
pumping

Titanium sublimation pump
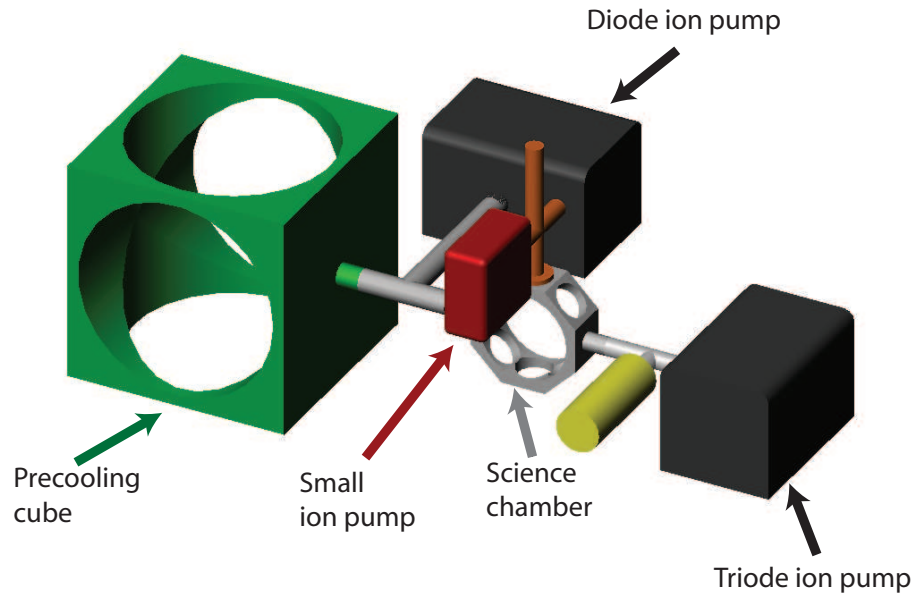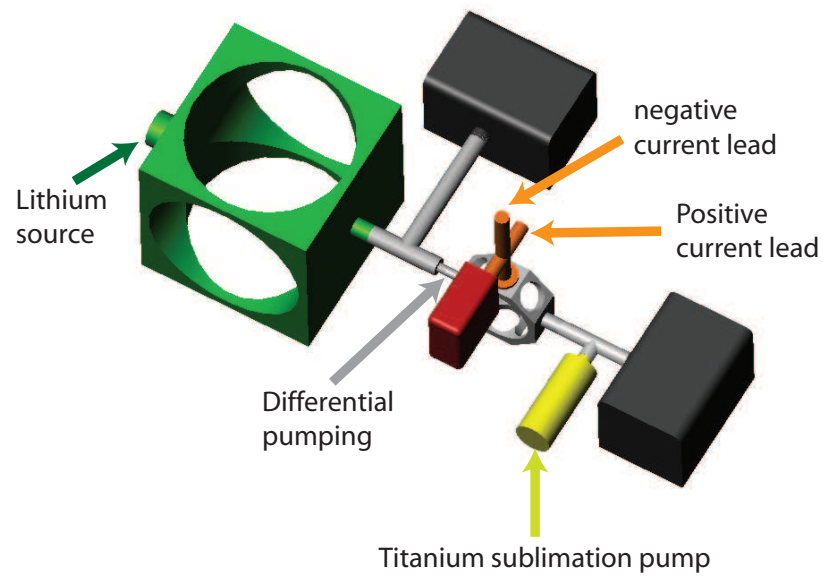
Figure 2.1: Two chamber vacuum system. (a) trimetric view (b) top view. Precooling chamber with heated Lithium source is green; Ion pumps are black and red; Science chamber is silver; Cross for current to feed in is orange

to heat the atom source up to about 290^oC to generate enough flux. With such a high temperature source in vacuum, it is even not possible for a good MOT to be in the same chamber. To solve this problem, we use a two chamber system as shown in Fig. 2.1. One is called pre-cooling cube and the other is the science chamber where MOT and Mini-Trap stay.

Because we don't need to open the vacuum chamber often, a complete ion pumped vacuum system is worry-free when it works. With the help of a Turbo pump, which is not shown in the figure, vacuum is pumped down. After the valve is closed, the Turbo pump is taken away. The $30l/s$ diode pump keeps $10^{-9}mbar$ vacuum level in the cube where heated Lithium travels from the source through the chamber cube. The Lithium flux is pre-cooled by a zigzag 2-D molasses beams, which we call it transverse cooling [45].

Pre-cool chamber, the cube, connects the science chamber through a differential pumping tube,which is shown on the fig 2.1(b). A two order of magnitude vacuum level difference is achieved. Before differential pumping, a mechanical shutter is inserted to make sure no extra flux is fed into the science chamber when MOT loading is finished.

On the other side of the science chamber, there are a $20l/s$ triode ion pump and a Titanium sublimation pump, which are standard equipments in BEC experiment.

On top of the science chamber, there is a vacuum cross for current to feed in. With so much degassing area, if we leave it alone, "dirt" will get into the science chamber and deteriorate the vacuum level. To address this problem, an $8l/s$ diode ion pump is mounted on the top.

2.1.2 Oven Bake Out

To achieve ultra-high vacuum, we had baked out the system to reduce the degas from the inner surface of the chamber. Aluminium foil and heating tapes were used to wrap up the apparatus.

Most part of the apparatus was baked up to $200/250^oC$. Since the science chamber is sealed by indium whose melting point is 156^oC, we controlled the temperature on

the window area below $70^{o}C$. For such a control, water cooling to isolate the science chamber had been used. In the end we found that air cooling was good enough and it also helped to degas the vacuum connection with the chamber.

A few key steps should be observed during the baking-out procedure:

- After baking for a few days, Titanium sublimation pump need to degas at $10A$ for hours. During the whole baking out, it also needs to sputter several times at $50A$ for 1 minute. One sign of good vacuum is that when it sputters we shouldn't see much change of current in ion pump.

- Lithium source also needs to be baked out at about $30-50^{o}C$ above operation temperature. Like Titanium sublimation pump baking out, this is finished when we don't observe a change in ion pump current when baking is on.

- In the end of baking, the current in all the ion pumps should be close to a few μA level. When change the current scale scale of ion pumps, we shouldn't see much change on the current level.

RGA, Residual Gas Analysis, is connected through Turbo pump to monitor the partial pressure of each gas component. In the end of backing, majority pressure is coming from H_2. After the Turbo pump is taken away, the apparatus is continue to bake for a few days until ion pump current reading doesn't drop.

Leaking current of ion pump could mislead our judgement. Leaking current can be observed by taking off the magnet around the ion pump. If we see a current reading change then there is leaking current for this ion pump and it should be sputtered.

After baking is completed and system is cooled down, the current reading on the two big ion pumps should be below resolution and the current in the top small ion pump is about a few μA.

A good vacuum after baking is indicated by the the lifetime of MOT, which was measured to be about $240s$. This implies that the vacuum level in our science chamber is below $10^{-10}mbar$.

2.2   Laser System

For the Lithium experiment, we work with D1 and D2 transition, which is about $671nm$. At this wavelength, currently the only commercial choice is to use DYE laser which can produce enough laser power. In the experiment, we use coherent 899 dye ring laser which is pumped with argon ion laser Innova Sabre. We manage to generate about $700mW$ power with $300kHz$ resolution from the dye laser using about $5W$ pumping power. Most laser beam is divided and redistributed from this beam.

The laser system can be divided into four parts. One is frequency/power preparation, which prepares MOT/molasses/repumping/probe beams. The second part is frequency lock loop which locks the laser to the atomic transition. The third part is power redistribution that redistributes laser to feed in different vacuum ports. The forth part is optical pumping diode laser system. In the end of this section we will discuss briefly an efficient MOT loading scheme.

2.2.1   Frequency and power preparation

As shown in Fig. 2.2, a polarized laser comes out from the dye laser and is divided with beam splitter $C1$. $30mW$ power is sent to frequency lock loop and the other is fed into the frequency/power preparation part. There are essentially three paths in this part. One is the path for MOT beam. The second path is for molasses and probing beam. The third path is for repumping beam.

AOM, Acousto-optic modulator A1 and A2 will split power from the main path when they are on. During MOT loading period A1 and A2 are off. So most power will go through EOM, Electro-optic modulator, E1/E2 on the figure. This is the MOT beam path. EOM2 is deeply driven so that it will print a frequency comb of the MOT beam, which we will call now a comb beam. The bounced back beam through E2 will go through the comb-beam-protection tube, which is used to get rid of stray light, and then be expanded to about $30mm$ diameter to be used as MOT beams.

Molasses/probing path is generated when A2 is on. A2 is also used as a switch. The -1 order beam which is $75Mhz$ red tuned, will be guided to a beam splitter C2 and then through a double path where A3 will be used to adjust the frequency
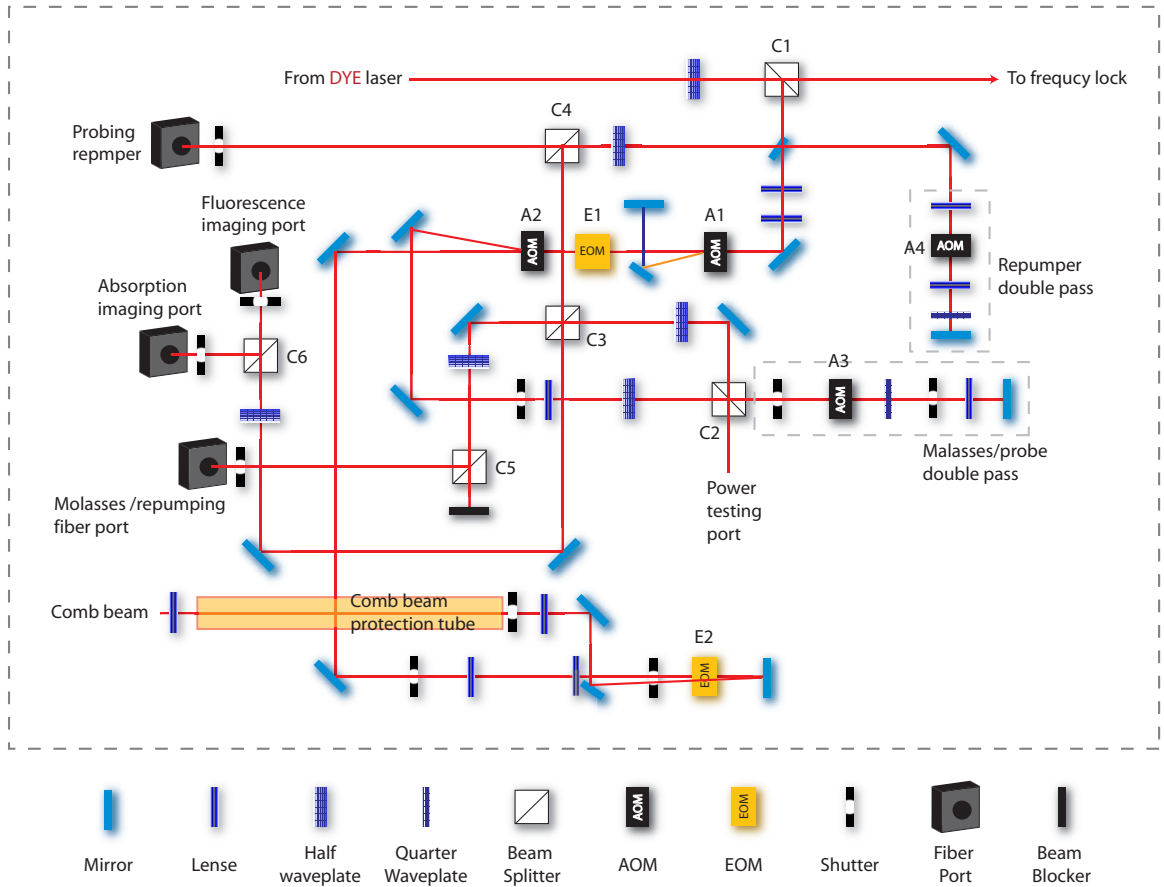
Figure 2.2: Main optical table

for molasses or probe beam. The half-wave plate before C3 will be used to split the power. The beam goes through the cube is the molasses beam and the beam being reflected is the probe beam. Molasses beam is fed into the fiber port and the probe beam is divided by beam splitter C6 for fluorescence and absorption imaging.

Repumping path is on when AOM A1 is turned on. It is a double path through A1 and will get into another double path with AOM A4. A1 and A4 is frequency controlled by the same source with about $200Mhz$ and we use the +1 order of both. With the two double paths, we generate the $800Mhz$ repumping frequency difference to repump atoms from $F = 1$ state back to $F = 2$ state. The reason to have such an independent repumping scheme instead of using the EOM, which is what we have done for MOT beam, is to have fully and precisely control of the power and frequency of the repumping beam during cooling and probing. This turns out to be very important. The half-wave plate before beam-splitter C4 is used to divide some power that will be used as repumping during absorption imaging.

One thing needs to be emphasized is that the repumping beam during cooling and molasses beam are coupled to the same fiber port when they are combined on beam splitter C3. This is necessary since it will automatically align the two beams during doppler cooling step and we save the time to align them.

2.2.2 Frequency lock loop

Doppler free saturation spectroscopy is used to lock the laser frequency to be $75Mhz$ below D_2 transition from $|2, 2\rangle$ to $|3', 3'\rangle$. The saturation beam is about $150Mhz$ blue detuned relative to the probe beam which is of the same frequency with the DYE laser. The detuning is achieved by the AOM which is frequency modulated. A lock-in amplifier is used to pick up signals from the photodiode. Dispersion signal is displayed on laser control box and used to feedback lock the dye laser.

2.2.3 Power redistribution for vacuum port

The chamber and optics around it are enclosed by a dark box which is used to prevent stray light. The prepared laser beam feeds into the black box through comb beam
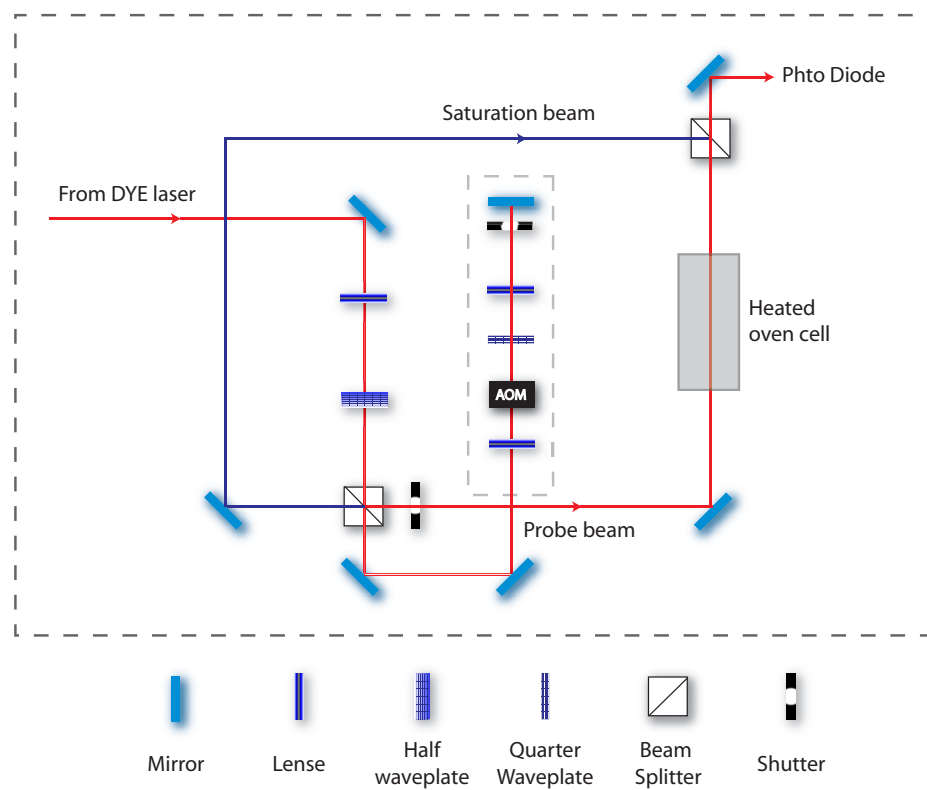
Figure 2.3: Dye laser frequency lock loop. Saturation beam is coded with blue color and probing beam is coded in red.
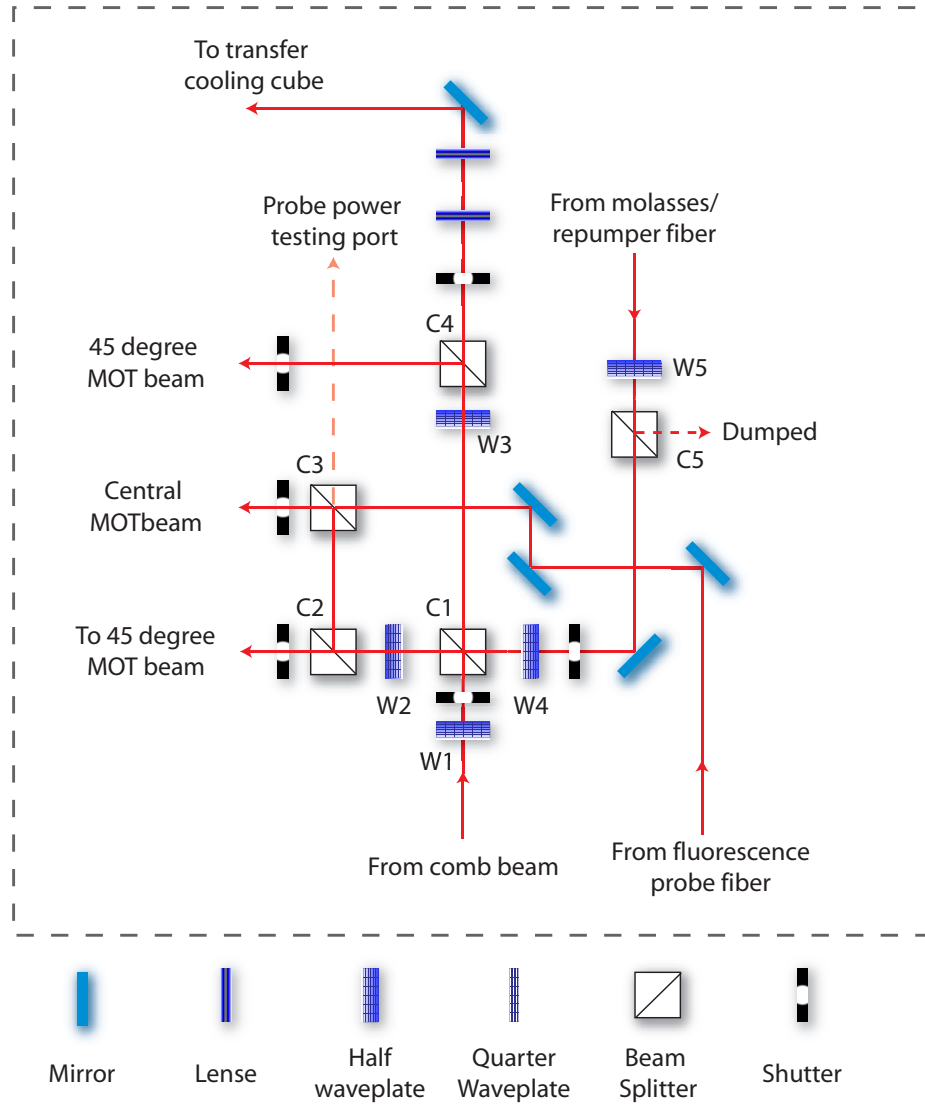
Figure 2.4: Laser power distribute before getting into chamber

ports and fibers. The comb beam is divided to be used as MOT beams and transverse cooling beams. Other laser beams from fiber are guided to the ports for the chamber.

Fig. 2.4 illustrates how laser is divided and guided in the black box. Half-wave plate W1 with beam splitter C1 split the comb beam power roughly half and half. W2, C2, C3, W3 and C4 evenly split the beam also. In the end a quarter of the comb beam power will go to transverse cooling and other three quarters will be divided by the three MOT beam. Molasses and probing beams are fed in similarly through W4 and C1. Although we used polarization maintaining fiber, we use another cube, C5, to clean the polarization after the fiber to ensure the stability.

The power balance for the three MOT beams is an important issue especially during cooling time. In the experiment we managed to achieve better than 10% balance for molasses beam. With this setting for comb beam, we can only balance the two 45^oC MOT beams due to the unclean polarization of the input comb beam.

Fluorescence probe beam path is also displayed on the figure. Absorption imaging beam is fed in with another fiber which is not plotted in the figure.

2.2.4 Optical pumping

For $F = 2$ state, as we will discussed in magnetic trapping, both $|2, 2\rangle$ and $|2, 1\rangle$ magnetic sub-state can be trapped in the magnetic trap. Due to the spin relaxation loss, we only want to work with $|2, 2\rangle$ state. We could either get rid of $|2, 1\rangle$ or convert it to $|2, 2\rangle$. The later option makes more sense since the more atoms trapped the easier for evaporative cooling. To convert a $|2, 1\rangle$ to a $|2, 2\rangle$, we need to apply optical pumping.

The optical pumping is realized by using the D1 transition with a σ^+ laser. This laser will pump $|2, 1\rangle$ to the D1 excited state $|2, 2\rangle$, which will decay back to $|2, 2\rangle$ on the ground state. Of course, some atoms will fall to $F = 1$ ground state so repumping light has to be present during the whole process. Actually we keep repumping light roughly $50 \mu S$ longer than the pumping beam to make sure no $F = 1$ ground state exists. This repumping beam is the same as we used during molasses cooling.

A homemade diode laser

Optical pumping beam is generated by a homemade external-cavity diode laser with a logic circuit that can automatically lock the laser. Two-Piezo control is used. One is not in the servo loop. This one is thick, sensitive, multi-stacked with broad scan range. It is driven with highly low-passed filter to get rid of noise. Since it is not in the servo loop, its response bandwidth is not a problem. The other is a thin insensitive small scan range Piezo which is in the servo loop to lock. Since it is insensitive, circuit noise is not a big problem and response bandwidth can be large. Both Piezo are mounted on a modified mirror holder which ensures tweaking stability and avoid looseness and hysteresis. Technical design details can be found at [46]. This diode laser system provides easy lock and stable operation.

Optical pumping setup and measurement

Aligning the optical pumping laser follows three-step procedure. First, we had to make sure the frequency was roughly right. To do this, we expanded the laser beam size big enough to cover the cloud and then we tweaked the resonance frequency by changing the magnetic bias current. Optical pumping, when it works, will increase the number of atoms that are transferred into the Mini-Trap. The number of atoms transferred into Mini-Trap was monitored and the laser frequency that could maximize this number was taken as the rough frequency.

After finding the rough frequency, we used a collimator lens to change the beam size to about $1 - 2mm$ diameter. This beam was then sent along with central MOT beam. A reflective mirror on the other side of the chamber was used to keep balance. Modulation on the MOT repumping by turning the big EOM, E1, on and off was applied while MOT had been fully loaded. At this time, we would see the repumping beam punch a hole through the center of the MOT. Fine tune the alignment and pumping laser frequency. Finally, the last step is to replace the collimator lens with a new lens that create a beam with about $1cm$ diameter. With such a big size, we can ensure that the whole MOT cloud, which is about $5mm$ diameter, is covered.

Optical pumping is applied before atoms are transferred to magnetic trap and after

laser cooling has finished. In the experiment, we observed about 60% more atoms were transferred into the final magnetic trap with optical pumping than without. This is tremendous amount of gain since evaporative cooling is an exponential process, the more atoms to start with the faster the process will be. Actually, experimentally we found that without optical pumping, we cannot drive the system into quantum degeneracy regime.

2.3 Radio frequency system

As we have discussed before, evaporation is one of the key steps for the BEC experiment. To achieve evaporation, we need a RF system which can provide frequency around $800Mhz$ for hyperfine transition and around $100Mhz$ for Zeeman transition within each hyperfine state.

2.3.1 RF frequency generation

A VCO, Voltage-controlled oscillator, is feedback controlled through a phase lock loop(PLL) with a arbitrary waveform generator HP8770A to generate the required RF frequency. Experimentally we set scan range of $200Mhz$, between $800Mhz$ and $1Ghz$ [46]. The RF signal is amplified by a $15W$ amplifier and feed into our antenna. The ramping sequence is programmed by PC through HP8770A with GPIB interface and the RF power can be adjusted by combination of different attenuator. The bandwidth of the output signal is below $10kHz$. Recently we adopted a newly designed RF system backed up by FPGA. The new system works equally well with resolution below kHz.

2.3.2 Antenna

To reduce the distance between the antenna and the Mini-Trap in which evaporative cooling will happen, we homemade a simple round loop antenna using isolated copper wires. The antenna is placed against the science chamber window and it is only a few centimeter away from the Mini-Trap center. Since the impedance of the antenna is

too small to match with the RF output from the power amplifier, an isolator is used to make sure the reflected power will not get back into the amplifier. Our simple setup works quite well for most experimental purposes.

2.4 Optical imaging

Almost all data in our experiment is taken by CCD camera with different imaging schemes.

2.4.1 Fluorescence Imaging
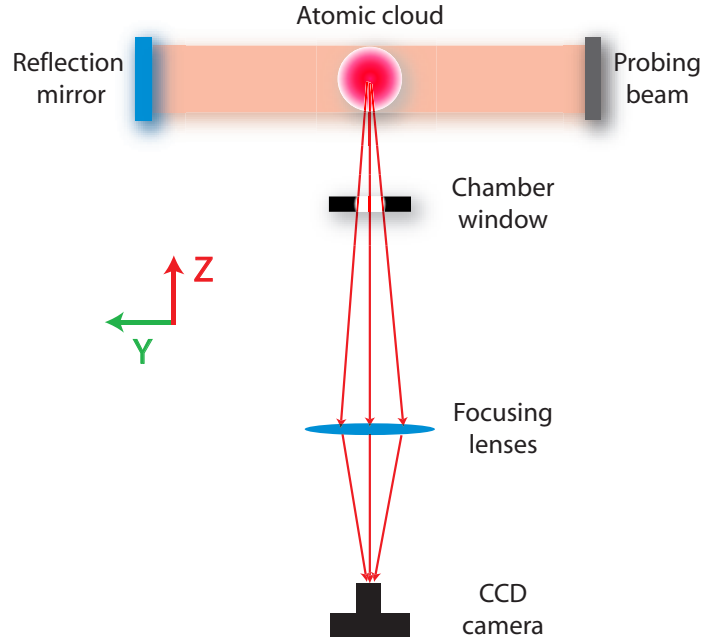
Figure 2.5: Scheme for fluorescence imaging

A saturation fluorescence imaging scheme is shown in Fig. 2.5. For MOT imaging, a $1/e^2$ diameter of $2cm$ probing beam which has about $100mW$ power is shined on the atoms. A reflective mirror ensures the balance so that we don't push the atom along Y direction. Camera is put under the science chamber with a lens to collect the

fluorescence scattering photons. The optical amplification of the lens is about 0.53 and the solid angle is determined by the size of the window on the chamber. Normal detection time will be set around 20-50 μS.

Two important steps should be taken for this imaging scheme to work. First, calibration of the camera has to be done off-line to link the integral signal on the camera with the number of atoms. They should be linear relation for fixed setup. Second, since the picture is taken in an abounding stray light environment, it is important to get rid of the background light by taking another picture without atoms. After subtracting this background image, a true fluorescence image only for atoms will be obtained.

Similar setup can also be achieved in the Mini-Trap and this has been used to calculate the transfer efficiency between coils.

Compared with other schemes, fluorescence imaging is easy to setup and maintain. On the other hand, since it uses very strong probing beams, it heats up the cloud so much that it will result in atom loss during probing. It is also limited by the solid angle of observation window in our experiment.

2.4.2 Absorption Imaging
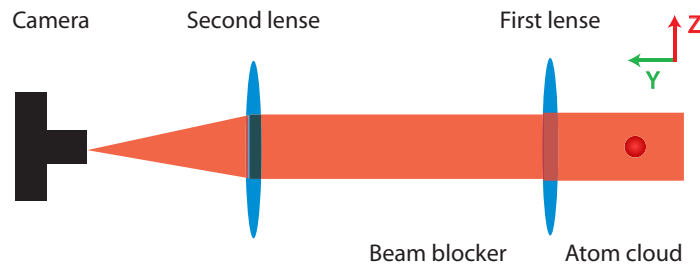
Figure 2.6: Scheme for absorption imaging

During absorption imaging, light from probe beam is resonantly scattered by atoms and the reduced intensity of the probe beam is measured, which will result a shadow on the CCD camera. Exponentially decayed intensity can be written as $I = I_0 e^{-OD}$, where I_0 is the original intensity and OD is optical density which can

be expressed as $OD(\vec{r}) = \int n(\vec{r}, \vec{y})\sigma_0 d\vec{y}$ with n as density of the cloud, σ_0 as the optical scattering cross section and y as the imaging axis.

The scheme of imaging is shown in Fig. 2.6. Probe beam is collimated to be big enough to cover the whole could. The probing intensity is about saturation level. Two magnification lens are used in $f - 2f - f$ setup to amplify the image that will be taken by the CCD camera. The amplification is $25/9$ and the pixel size is 8μ. This put our camera resolution to be around $3\mu m$, which is already smaller than optical resolution.

Since the probe beam is never perfectly flat with uniform power, we need to take a reference frame where atom does not exist. At the same time, after taking into account the stray light that may hit the camera with a dark ground image, we will have:

$$
\begin{aligned}
OD_{measure} &= -ln\left(\frac{I_{with\_atom} - I_{dark\_ground}}{I_{without\_atom} - I_{dark\_ground}}\right) \\
&= \sigma \int n(\vec{r}, \vec{y})d\vec{y}
\end{aligned}
\tag{2.1}
$$

where

$$
\sigma = C^2 \frac{\lambda^2}{2\pi}\left[1 + \left(\frac{\delta}{\gamma}\right)^2\right]
$$

with the Clebsch Gordon coefficient $C^2 = 1$ for σ^+ probing, natural linewidth $\gamma = 5.9 Mhz$, and detuning $\delta = 0$ in the experiment.

In each experimental cycle, we will take 4 imaging shots. Immediately after the imaging shots with atom, we will take one dark ground image for it. After the reference shots for the case without atom, we will take another dark ground shot for it too. Using frame transfer concept by blocking two third of the imaging zone, the first two shots are separated by ms level and after a few hundred ms saving time, the other two shots will be taken.

A typical absorption image is shown in Fig. 2.7, which corresponds to $6\mu K$ atom cloud with peak optical density of 3. This peak optical density indicates that about 95% of light has been absorbed. Immediately after transfer into the Mini-Trap, we have optical density about 4.
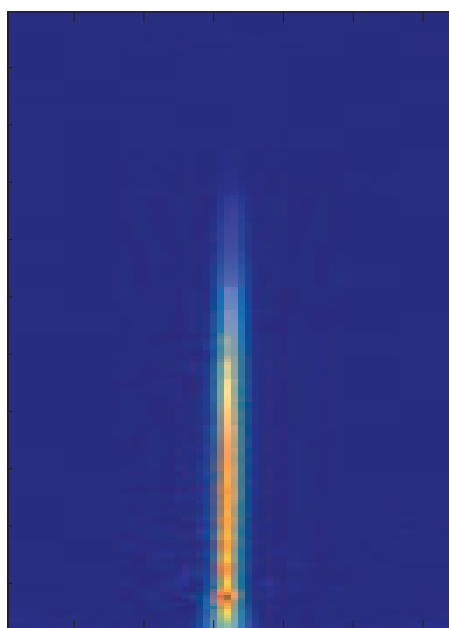
Figure 2.7: A typical absorption imagine at RF=805Mhz

2.5 Mini-Trap design and realization

To realize BEC and study its quantum behavior, a conservative trap is needed to compress and hold the dilute cloud. In the early time of neutral atom trapping, influenced by plasma confinement and ion trapping, people have tested different trapping configurations, for instance, DC/AC magnetic fields, microwave field and far off resonant laser trap. DC magnetic trap combined with RF evaporative cooling has been quite popular and proved to be major working horse to achieve BEC. This is because of its feature like long lifetime, large volume, deep trapping depth, reasonable confinement, versatile design for different purposes and easy setup. Our Mini-trap is one of the DC magnetic trap. In this chapter, by comparing with other schemes, we will present the unique design of Mini-trap and propose that it is an excellent candidate as a trapping platform for a portable system.

2.5.1 Different magnetic trapping schemes

In Chapter 1 we have discussed the interaction between neutral atoms and external static magnetic field. We have also discussed the principle for magnetic trapping. Here we will review a few different trapping schemes.

Quadruple trap

The simplest magnetic trap is quadruple trap. It can be realized by two anti-Helmholtz coils, see Fig. (2.8). The trap is linear in the center and it offers superior confinement compared with other parabolic traps. As can be seen on the figure, in the center of the trap, the magnetic field is close to zero so quadruple trap suffers from Majorana loss. Due to this reason, it is impossible to use a quadruple trap alone to create BEC since whenever an atom settles to the ground state in the trap center it will get lost easily. Many remedies have been tested to plug in the hole, for instance, with blue detuned dimple laser to push atoms away from the zero field [4], with time averaged orbiting potential (TOP) [47] and with nonzero trap bottom harmonic trap —Ioffe-Pritchard(IP) trap [48, 49].

Although the quadruple trap is not good for trapping BEC, it is widely used to spatially transfer the atomic cloud. It has the advantage of large volume and easy implementation for long distance relocation. The Majorana loss in quadruple trap during transfer can be ignored since the transfer normally happens in the time scale of a few hundred ms. In our experiment we have used two pairs of rectangular quadruple traps to move the cloud for a few centimeters.

TOP Trap and IP trap

Two major magnetic traps for BEC experiments are TOP and IP traps.

TOP trap uses a rotating field to move the center of a pair of quadruple trap. The rotating frequency is much higher than the trapping frequency so that the atoms feel a time averaged magnetic field. The rotating frequency is lower than Larmor frequency so that moving atoms can follow the local field change. The instantaneous minimum of field rotates around a central point and this forms the "circle of death", where the magnitude of magnetic field is zero and atoms will lose due to Majorana loss. The time-averaged potential is harmonic to the lowest order at the center of the trap, which can be written in a longitudinal coordinate as:
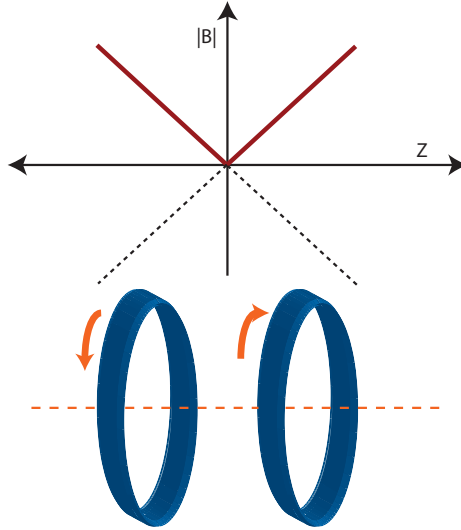
Figure 2.8: Quadruple trap set up and effective magnetic field

$$U_{TOP} = \frac{\mu_m}{2}\left(B''_\rho\rho^2 + B''_z z^2\right) \tag{2.2}$$

$$B''_\rho = \frac{B'^2}{2B_0} \quad B''_z = \frac{4B'^2}{B_0} \tag{2.3}$$

where B' is the linear gradient, B_0 is the magnitude of rotating field and $\rho^2 = x^2 + y^2$.

It can be shown[46] that the trap depth of TOP, $U_{TOP} = \mu_m B_0/4$, is proportional to the rotating field while the trapping frequency is reversely proportional to the rotating field. This means there will be a compromise between deep trap and tight trap for TOP. For ^7Li, due to the lack of sub-doppler cooling, it is important to have deep trap to load enough atoms into the trap and tight confinement to keep efficient evaporative cooling. Experimentally, a TOP trap has been tried for ^7Li and it was proved not to work.

An IP trap includes four Ioffe bars and a pair of pinch coil, Fig 2.9. Four Ioffe bars provide the radial confinement and the pinch coil provides the axial confinement. The Helmholtz setup of the pinch coil also provides the nonzero magnetic field along the axial direction in the center of the trap. If necessary, additional bias coil can be used to tweak the magnetic magnitude in the center to change the trapping frequency.

When the the cloud temperature $k_b T \gg \mu_m B_0$, the IP trap is close to a linear trap and it is called linear regime. When the cloud is cold enough, $k_b T \ll \mu_m B_0$, the atomic cloud are in harmonic regime. In the center of the IP trap, to the lowest order, the effective trapping potential can be written as anisotropic harmonic potential:

$$U_{IP} = \mu_m\left(B_0 + \frac{1}{2}B''_r(x^2 + y^2) + \frac{1}{2}B''_z z^2\right) \tag{2.4}$$

where B''_z is the curvature in axial direction and $B''_r = \frac{B'^2_r}{B_0} - \frac{B''_z}{2}$ is the effective curvature in the radial direction with B'_r as the gradient in the radial direction. In most situations, $\frac{B'^2_r}{B_0} \gg \frac{B''_z}{2}$ we then have the radial curvature

$$B''_r \approx \frac{B'^2_r}{B_0} \tag{2.5}$$

Ignore the ineffective constant B_0 in equation 2.4, we can write the potential of an IP trap as:

$$U_{IP} = \frac{1}{2}m\left(\omega_x^2 x^2 + \omega_y^2 y^2 + \omega_z^2 z^2\right) \tag{2.6}$$

where the trapping frequency can be expressed as:

$$\begin{aligned}
\omega_x &= \omega_y = \sqrt{\frac{B_r''\mu_m}{m}} \\
\omega_z &= \sqrt{\frac{B_z''\mu_m}{m}}
\end{aligned} \tag{2.7}$$

From equations 2.5 and 2.7, we can see that the trapping frequency in the radial direction can be changed by tweaking the trap bottom B_0 which is generated by the pinch coil. In the experiment, in order to keep the confinement in axial direction, instead of reducing the current in the pinch coil, we put a bias coil parallel to the pinch coil plane. The current in the bias coil is running in an opposite direction to pinch coils. The bias coil is place far away so that the bias field can be viewed as constant in the center of the trap and the trap can be still considered as harmonic.

The motion of atom in a harmonic trap can be considered separable [42] so that energy is conserved in each direction. For a thermal cloud, according to Boltzmann
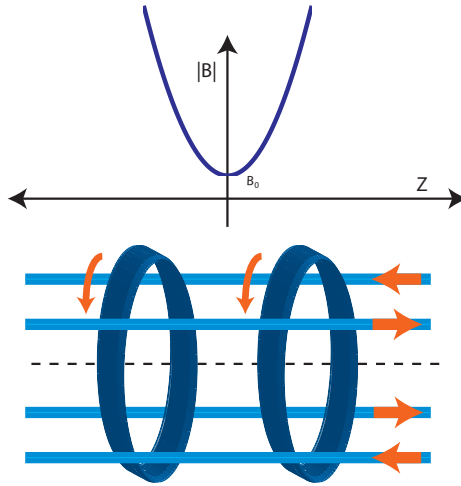
Figure 2.9: Standard Ioffe-Pritchard trap setup and effective magnetic field

distribution, atoms with temperature T in such a potential will distribute as:

$$
\begin{aligned}
n_{harmonic}(\overrightarrow{r}) &= n_0 exp\left(-\frac{U_{harmonic}(\overrightarrow{r})}{k_B T}\right) \\
&= n_0 exp\left(-\frac{x^2}{\sigma_x^2} - \frac{y^2}{\sigma_y^2} - \frac{z^2}{\sigma_z^2}\right)
\end{aligned}
\tag{2.8}
$$

where

$$
\begin{aligned}
\sigma_x &= \sigma_y = \sqrt{\frac{k_B T}{\mu_m B_r''}} = \frac{1}{\omega_r}\sqrt{\frac{k_B T}{m}} \\
\sigma_z &= \sqrt{\frac{k_B T}{\mu_m B_z''}} = \frac{1}{\omega_z}\sqrt{\frac{k_B T}{m}}
\end{aligned}
\tag{2.9}
$$

In the experiment, equations 2.8 and 2.9 are used to fit the cloud to get the temperature.

Micro-Trap

Due to the success of micro-fabrication, people has been pursuing to put BEC on a chip [50]. Micro-trap is also a kind of IP trap. Different from traditional gigantic trap which will normally dissipate kilo-watts, the power dissipation for Micro-trap is very low yet it provides very high confinement due to the close layout of the wires. With such kind of confinement, a few seconds' evaporation results in BEC for Rb. On the other hand, the trapping volume and trapping depth for Micro-Trap are very low. Apparently, it cannot be an option for ^7Li since it would need quite a lot of hot atoms to start evaporation.

2.5.2 Magnetic trap design consideration: scaling law

To work well with RF evaporative cooling, the performance of a magnetic trap depends on local parameters and global parameters. The local parameters, such as the gradient and curvature of the trap, determine the efficiency of evaporative cooling and the global parameters, such as the trapping depth and volume, will effect the number of atoms that can be loaded into the trap.

Local parameters

As we have discussed, in a typical cylindrically symmetric IP trap, the trap confinement is related to the radial magnetic field gradient that scales as $B_r' \sim I/r^2$ and axial field curvature that scales as $B_z'' \sim I/r^3$, where r is the magnitude of distance between the wire and the center of the trap and $I \sim jr^2$ is the current in the wire with j as the current density. This means that $B_r' \sim j$ and $B_z'' \sim jr$. So theoretically smaller trap with smaller r can only increase the axial curvature. In practice, due to cooling consideration, smaller trap can always maintain much higher density than big trap. For instance, the micro-trap has-orders-of-magnitude larger current density than traditional large multiple winding traps. This is why micro-trap normally has much higher trapping frequency.

Global parameters

The trap depth of an IP trap scales as jr ad the trapping volume scales as r^3. To load a large portion of atoms into the magnetic trap, the trap depth must be larger than the average energy of the cloud. On the other hand, volume of the trap should also be close to the size of the loading cloud so that there is no much spatial cut loss. Although for a small trap, we can increase the trap depth by increasing the trapping current, the overhead of required cooling will also increase much faster to maintain a good vacuum. By this argument, apparently a large trap is better with global variables.

2.5.3 Mini-Trap Realization

With the scaling law in mind, we are trying to find an optimized solution that combines the merit of large and small traps and can be used in most situations especially for interferometry in a portable system. The mini-trap consists of two parts, the *main body* and the micro-fabricated *ceramic chip*. The trap was manufactured by a company called Omley Industries in Oregon state, http://www.omley.com/

Main body: copper tube

The main body of the mini-trap is machined form a solid piece of oxygen free copper. The copper alloy has high electric conductivity. As shown in Fig. (2.10), the length of the trap is $17mm$, the outer diameter of the trap is $8mm$ and the inner diameter is $5mm$. This is where the name of mini-trap comes from, a millimeter trap.
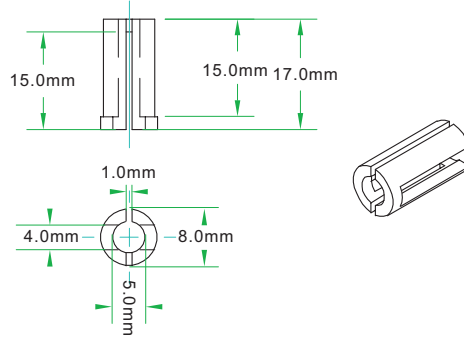
Figure 2.10: Copper tube: main body of IP trap structure

The two perpendicular cuts leaves four Ioffe bars and a residual arc at the bottom of the trap. One of the cuts opens a slot of $4mm$ wide, which is used for optical imaging. The other slot is $1mm$ wide. The reason for the asymmetry is to maintain high confinement while leaving a large enough solid angle for imaging.

Smaller geometry, such as reduced height, offers higher axial confinement. In our case, the trap size is chosen to be comparable with the size of 5×10^8 Lithium atoms that we can transfer into the trap after laser cooling. For other alkalis, which can be better prepared before evaporation, the size of the trap can be reduced.

Ceramic chip with DBC technology

The main copper tube provides the four Ioffe bars and one of the pinch coils in an IP trap. The tube is brazed to the lower side of a ceramic chip. The second pinch coil sits on the upper side the ceramic chip, Fig. (2.11)(a).

The chip is manufactured with direct bond copper(DBC) technology. $0.3mm$ thick Cu foil is bounded to both sides of the $0.6mm$ alumina ceramic substrate in N_2 gas
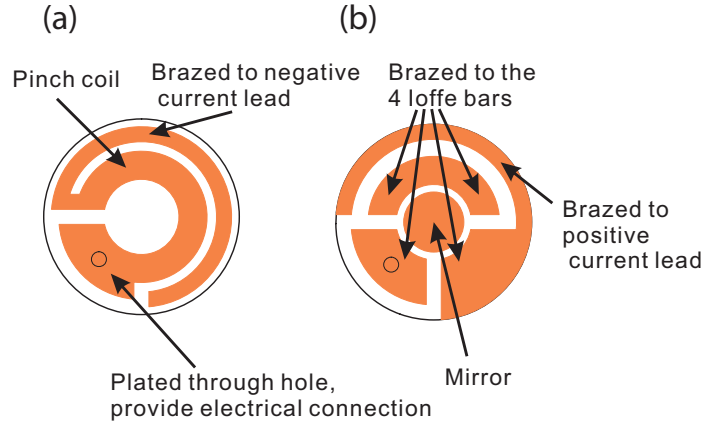
Figure 2.11: Ceramic chip structure: (a) Upper side of the chip; (b) Lower side of the chip

environment at $1069^{o}C$ to $1072^{o}C$. The chemical reaction compounds form strong bond in the vicinity of the interface of Cu and alumina. The pattern is created by chemical etching. Compared with other micro fabrication process, such as thin/thick film process, DBC provides the best thermal conductivity and allows for the biggest carrying current on the copper layer. This property is proved to be important for our system since only simple water cooling overhead is placed in our apparatus to maintain a good trapping lifetime.

The outer side ring of the upper side of the chip, Fig. (2.11)(a), is brazed to the negative current lead. The current is fed through the ceramic chip using Via technology as shown with a dark circle on the chip. The inner side ring have the same size as the copper tube and it is used to generate the second pinch coil field. The two rings run against each other. This will reduce the strength of the field. By simulation and experiment, it turns out this is not major problem since this is not the lowest saddle point for the trap.

The lower side of the chip, Fig (2.11)(b) looks a little complicated. The outer ring is brazed to the positive current lead. The black circle is the position for Via. Top of the copper tube is connected to the four points shown on the figure. A polished gold coated mirror sits in the center. This is left as a reflective mirror for optical lattice

experiment.

Mini-trap assembly
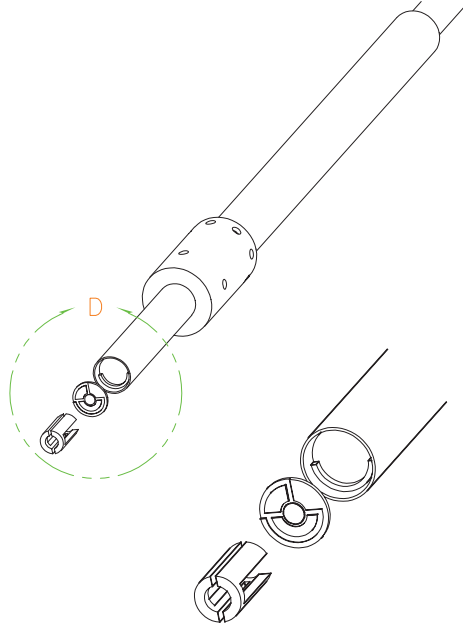
Figure 2.12: Assembly for the mini trap

The copper tube, DBC chip and current leads are brazed in a high-temperature (700^oC) vacuum environment. Fig. (2.12) clearly shows the relative relation between the three parts.

Cooling water flows from top in a hollow and blind copper tube with about $5mm$ to the chip. This short distance ensure a good thermal contact. This tube is also used as negative current lead. The positive current lead is coaxial with the negative lead so as to minimize distortion of the magnetic field. Ceramic spacers between the two leads are used to ensure that they are not shortly connected. Fig. 2.13 illustrates the 3D appearance of the whole structure.

The whole ensemble is connected to a conflate flange with ceramics to ensure electric insulation and ready to be connected to other vacuum parts on the apparatus.

Simulation for magnetic trapping field in Mini-trap

To get a quantitative characterization of our trap, we run a simulation of the effective
magnetic field for atoms. Although a more accurate model could be used to calculate
the field distribution, for the purpose of rough estimation, we used a simple single
wire model for the simulation. Since the size of the Ioffe bars and pinch coils are
relatively smaller than the size of the trap and we only want to consider the field in
the center of the trap, the effective magnetic field of the Ioffe bar can be approximated
by a single wire and each of the two pinch coils is each approximated by four wires.
The extra ring on the top of the ceramic chip, as shown in Fig. 2.11, is integrated
as a round coil. The simulation result for trapping current of 100A is indicated in
Fig. 2.5.3.

A few observation should be made from the simulation results:

1. The gradient in x and y direction is roughly the same about 500G/cm and the
   gradient along z direction is close to zero.

2. The trap depth in x direction is much higher than y direction which is because
   y axis is the imaging axis and there is wider opening along y direction.
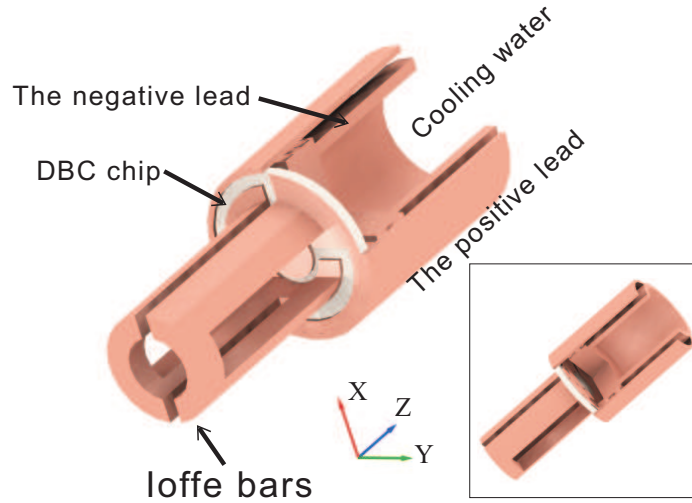
Figure 2.13: Assembly for the mini trap after rendering

3. The magnetic field on the upper side along z direction is much higher than the lower side. This is due to the effect of extra ring on the top of the ceramic chip.

4. The trap depth is about 70G which is determined by the saddle point along y axis.

5. The trap bottom is much higher than zero. To have tight confinement we need a bias field to change it.

6. The trapping frequency along z direction is calculated to be around 60Hz

From the simulation results, in linear regime, we can see that the field gradient along x direction is about $800G/cm$ and it is about $400G/cm$ along the y direction. Close to the center, the gradients in x and y direction are both calculated to be about $510G/cm$ and the gradient along z direction is close to zero.

2.6 Mini-Trap characterization

In this section, after we finished the discussion of experimental sequence, I will present measurements that characterize the Mini-Trap.
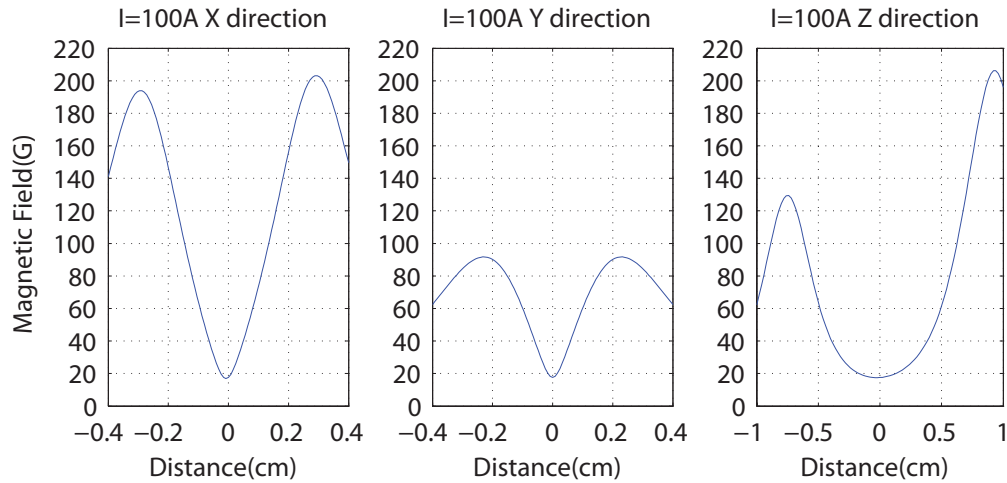
Figure 2.14: Simulation of magnetic field for Mini-trap

2.6.1 Transfer between traps and experimental sequence

Transfer efficiency is a big issue in our experiment because for ^7Li to have run-away evaporation we need a good number of atoms to start with. High efficiency ensures that we can fully optimize the experimental sequence.

As we have discussed before, we use a zigzag broadband optical beam to pre-cool and guide the atoms into the science chamber where the vacuum is maintained at $10^{-10} mbar$ level. Most optical and magnetic devices sit around this silver hexagonal chamber as shown in Fig. 2.15.

The MOT coils, the big yellow coils on the figure, are aligned roughly coaxial with the chamber. With 6 optical beams, they are used to collect atoms from the vapor environment which is supplied by the collimated Lithium beam. The blue and orange rectangular shape quadruple traps are transfer coils to move atoms vertically from the MOT area to the center of the Mini-Trap, the copper color tube sitting on the top area of the science chamber.

The experiment would include four parts:

- Load atoms to the MOT

- Doppler cooling and optical pumping to prepare state

- Transfer from MOT to quadruple, quadruples to quadruples, and quadruple to Mini-Trap

- Evaporation and scientific experiment in the Mini-Trap

The timeline of the experiment is shown in Fig. 2.16. Since we have discussed molasses cooling and optical pumping in Chapter 1, in this section, we will concentrate on the transfer between coils.

Transfer from MOT to quadruple trap

The inner diameter of MOT coil is about the same size of the chamber windows. This is to ensure that we have good optical access. The close placement of MOT ensures good confinement. The current running in MOT during loading period is about $7A$.
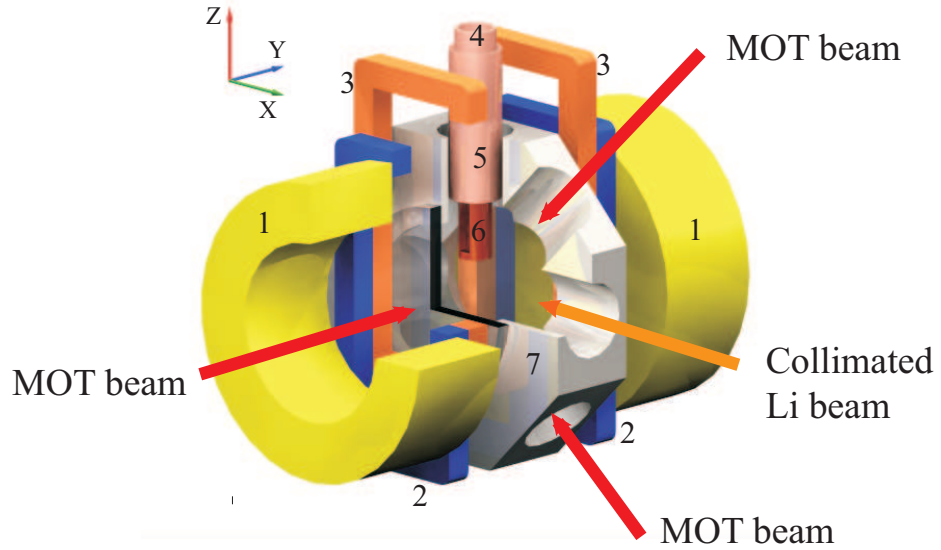
Figure 2.15: The scientific chamber setup: 1.MOT coils 2.Lower rectangular coils 3.Upper rectangular coils 4.The negative lead of the Mini-Trap 5.The positive lead of the Mini-Trap 6.Mini-Trap 7.Vacuumm chamber

The heat created by the MOT heats the chamber a little bit. In the experiment, we tried to run different water cooling schemes for MOT coils. In the end, for simplicity and practical reasons, we only use air cooling by putting the coil on a metal holder.

After the MOT loading period, atoms in the MOT are transferred to the round quadruple trap created by the MOT coil itself. This is done by turning of the laser beams and raising up the current to about $50A$ using a boost circuit. It is important to align the center of the MOT with the center of the quadruple trap so that during transfer the atom will not be spatially dragged and heated. This transfer process should be finished as soon as possible. Although MOT and quadruple trap has similar trapping structure, The majorana loss of the quadruple trap will lose the cold atom quickly if we ramp the current slowly. In the experiment we manage to raise the current up within $1ms$.

The circuit manages the currents are shown in Fig. 2.17. The MOT coil has two input sources. One is generated by $P3$ to provide current during MOT loading period. The other source is generated by a boost circuit which provides the snap-on trapping
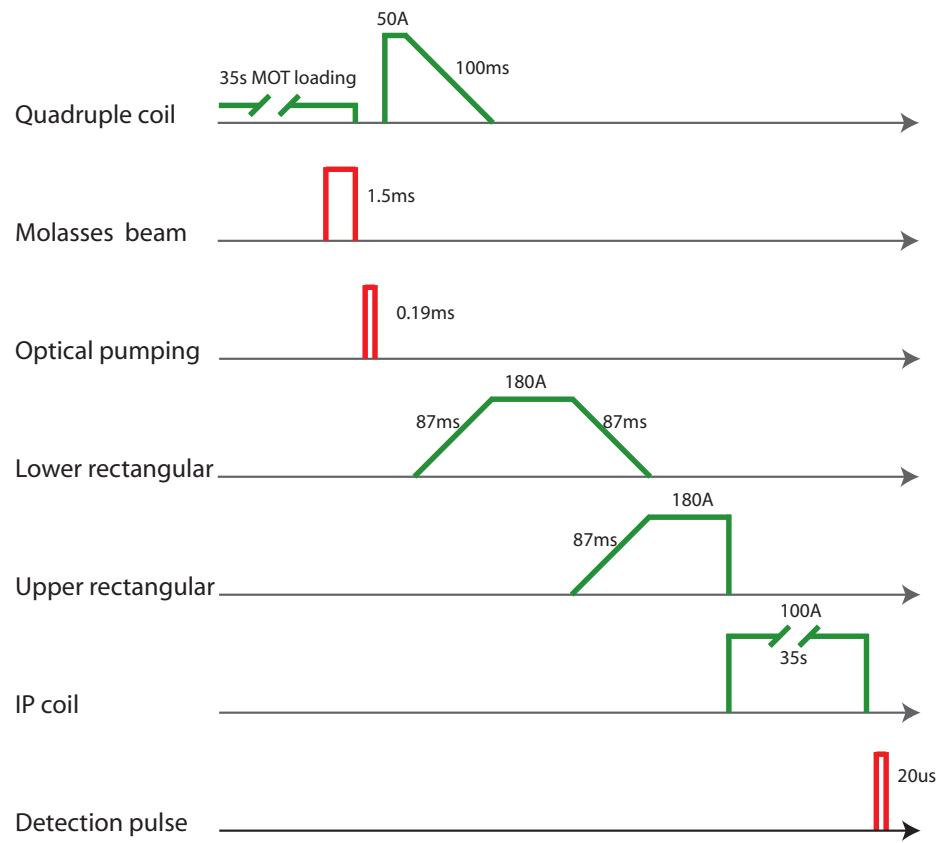
Figure 2.16: Experimental sequence

current to transfer atoms from MOT to the round quadruple coil. The boost circuit also has two parts. One is a feedback loop controlled by regulation waveform to provide ramping for transfer between MOT quadruple and lower rectangular quadruple. The other is the discharge unit which is composed of $R3$, $P2$ and $C2$. After Doppler cooling, the MOT current switch will be turned off and optical pumping will apply to prepare the state to be $|2, 2\rangle$. The $|2, 2\rangle$ atoms will be transferred to the round quadruple trap by turning on the B-switch. When the B-switch is on, $C2$ will discharge. This provides the initial fast ramping. Without such a part, the ramping speed will be about $2ms$ in stead of $1ms$.

One thing needs to be emphasized is that the power supply $P1$ on the circuit Fig. 2.17 is composed of two car batteries. The reason to choose battery is to exploit its quiet property so that we can reduce noise. On the other hand, since we only need a high current for a short time, it can be used for months before recharge.

Experimentally we observe more than 40% transfer efficiency from MOT to round quadruple (first such test was done on June 2004). This is estimated by holding atoms in the quadruple for $100ms$ and compare number of atoms left with number
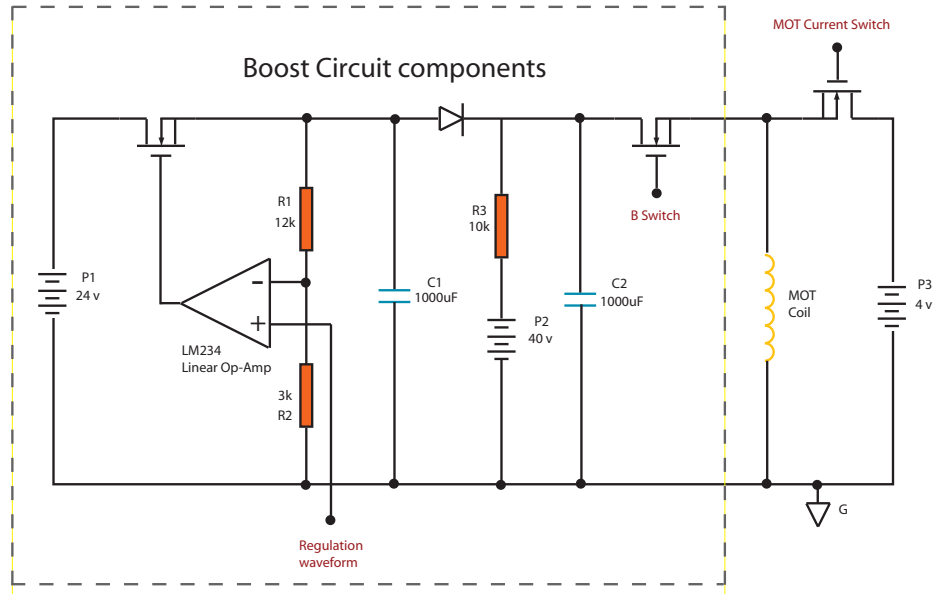
Figure 2.17: Current circuit for MOT coil

of atoms before transfer. This means in the experimental sequence, the efficiency is even higher.

Transfer between quadruple traps

After atoms are transferred to the round quadruple coil, the current in the round coil is ramped down and current in the lower rectangular is ramped up to spatially move the atoms upward. In the same way, atoms are transferred to the upper rectangular trap. The current ramping sequence is illustrated in Fig. 2.16. By this way, the atoms are moved upward for about $2cm$.

Spatially transfer atoms using quadruple trap is a standard technique. Here I want to mention four things to help increase transfer efficiency:

- The shape of the rectangular trap is to adiabatically elongate the shape of atom cloud before being inserted into the Mini-trap through the pinch coil on the bottom for better a mode match.

- Both rectangular traps sit on a translation stage. This ensures that we can tweak the planar position for a better transfer.

- The whole Mini-Trap is mounted on three micrometers which can be used to tweak the orientation of the Mini-Trap. They have also been used to scan for the best transfer efficiency.

- The center of upper rectangular is put a little higher than the center of the Mini-Trap. In this way, we can vertically position the cloud by changing the transferring time.

In the experiment, we tested the transfer efficiency among quadruple traps by transferring atom cloud up and back. Even with the situation that some atoms may hit the medal boundary of the Mini-Trap tip and get lost, we have more than 80% transfer efficiency between quadruple traps.
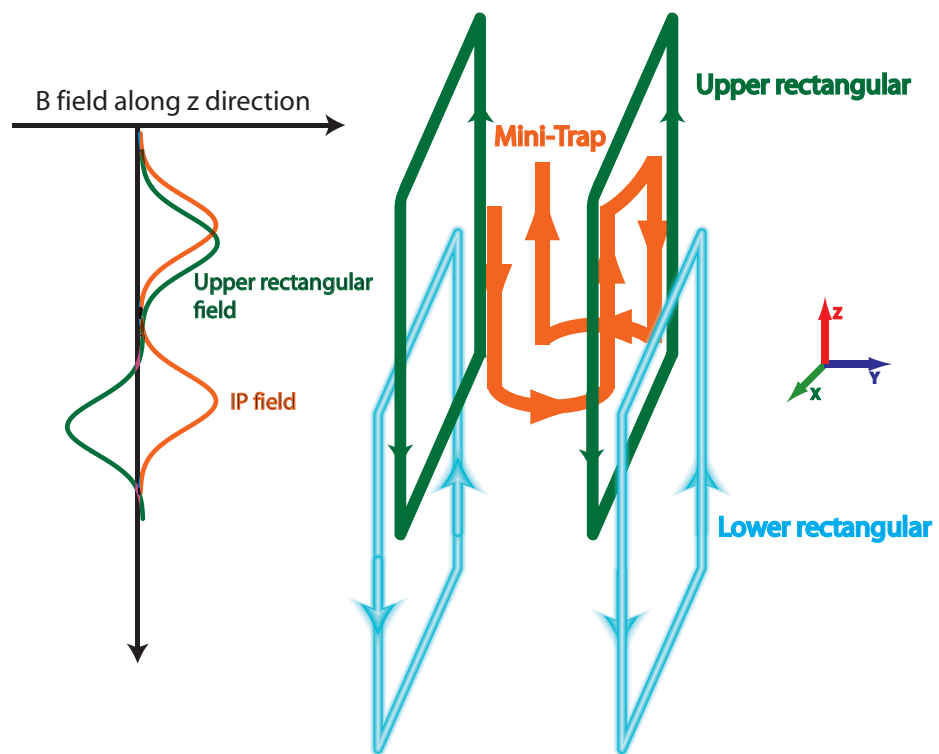
Figure 2.18: Current scheme in quadruple traps and Mini-Trap

Transfer from quadruple trap to Mini-Trap

In this part, we will discuss a technique called *semi-adiabatic* transfer. Since quadruple trap and Mini-Trap have different topographical structure, it is not possible to adiabatically transfer between them like what we do for transfer between quadruple traps.

In Fig. 2.18, we showed the direction of currents in different trap. In x and y direction, the current scheme is about the same for all three coils and it is also the same for the round MOT coil. Along z direction, the Mini-Trap has different field structure compared with quadruple traps due to the Helmholtz setup of pinch coil. On the left side of the same figure, we plot the magnetic field distribution along the z direction for the upper rectangular coil and Mini-Trap both of which are the concerns for final transfer. We notice that the superposition of the fields from the two coils will cancel each other at some area and this will result in a big hole during transfer with a large loss expected.

To solve such a problem, we would expect the transfer to finish as fast as possible so that the loss can be minimized. On the other hand if the transfer is not adiabatic, we will heat the cloud and lose phase space density before evaporation. The solution for this is to exploit the features of our anisotropic traps. Along the axial direction, z direction on the figure, the trapping frequency is much lower than the tight radial direction. If we ramp the current of upper rectangular and Mini-Trap with speed faster than the axial oscillation and longer than the radial oscillation, we would have adiabatic transfer in the radial direction with tight confinement. At the same time, we can also do it so fast that the loss in axial direction can be ignored. This scheme is called semi-adiabatic transfer. In the experiment, we manage to transfer with $1ms$, which is about $1kHz$. Considering the radial trapping frequency is about $3kHz$ and axial trapping frequency about $50Hz$, this is right in between. Experimentally we manage to transfer more than 25% atoms from upper rectangular trap to the Mini-Trap.

The current directions for rectangular coils and Mini-Trap are very important. If we reverse one or two of them, we will experience serious loss during transfer. For instance, if we run the current in rectangular traps reversely, we will lose all atoms

in the Mini-Trap in a few seconds.

2.6.2 Mini-Trap Lifetime Measurement
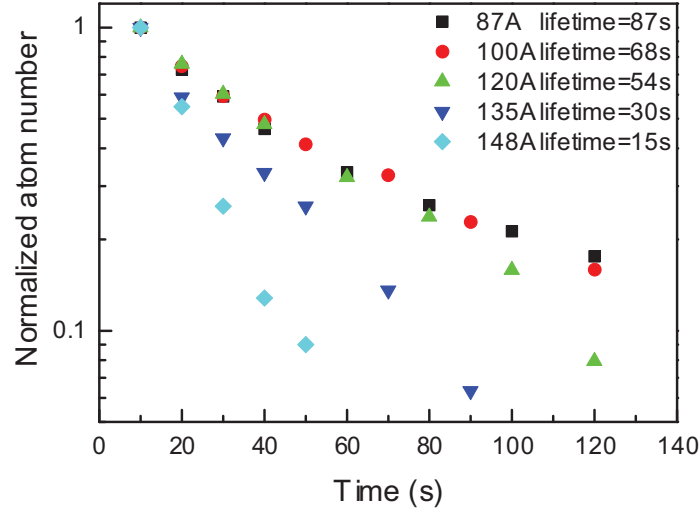
Figure 2.19: Trapping lifetime for different trapping current

A good trapping lifetime is the key for the success of evaporative cooling. Since our trap sits inside the vacuum, the heating due to current running through will deteriorate the vacuum. One great feature of Mini-trap is its low power dissipation. Due to the small resistance, the power cost is only $7W$ for $100A$ trapping current and the thermal conductive ceramic chip ensures that the generated heat is well dumped by the cooling water on the top. Although theoretically we could use more aggressive cooling scheme with liquid Nitrogen, experimentally we find that water cooling is sufficient for our experimental purpose.

Fig. 2.19 displays a trapping lifetime measurement for different trapping current. We can see that with a $100A$ current, the trapping lifetime is about $70s$. The lifetime doesn't change much when the current is below $120A$. When the current is higher than $135A$, we can see dramatic drop in lifetime. This is due to the heating-induced vacuum deterioration.

To test the robustness of the trap with a high current, we ran $150A$ through the

trap for 90 seconds. We can still see trapped atoms at the end of such a long period. The vacuum recovers after 5 to 10 minutes without running.

2.6.3   Mini-Trapping Depth Measurement
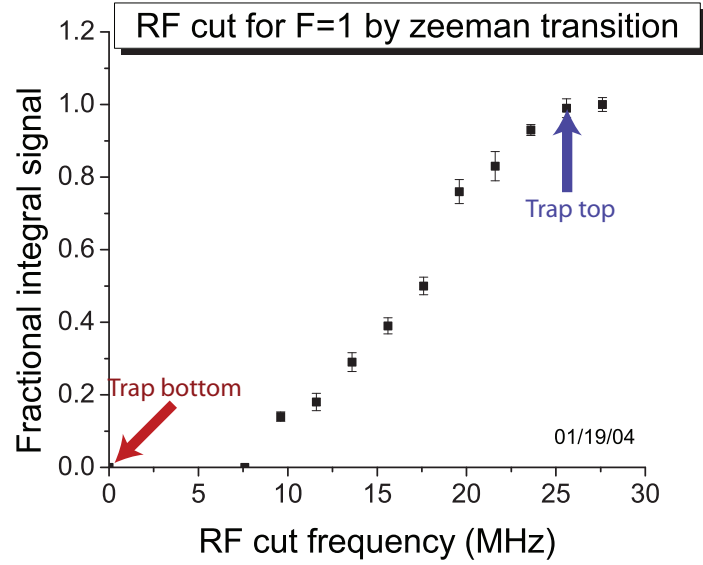
Figure 2.20: RF cut for F=1 state for trap depth measurement

It is not a easy task to measure the trap depth for such a small device as Mini-Trap sitting inside vacuum. To have an experimental measurement rather than theoretical calculation alone, we use a simple sequence with the help of short time RF evaporation.

A typical RF cut plot is shown in Fig. 2.20. The x axis is the applied RF frequency minus trap bottom and the y axis is the percentage of atoms left after applying such a RF to atoms that will be there without RF. RF lasts for 4 seconds. The picture for different RF level is like this:

- When the RF cut is higher than the highest energy of atomic cloud, almost all atoms will be intact. we will have 100% left in the trap after RF.

- By lowering RF, the hot atoms will be thrown out and colder ones will be left. By continuously lowering RF, the percentage of atoms left will decrease till zero.

- In the end when RF is below the trap bottom, no atom will be affected and we will measure a 100% left again after RF. The RF level for this to happen is the trap bottom.

For a deep trap that atoms don't fill up, our measurement detects the highest energy of atom cloud and trap bottom. To apply this technique to measure the top of the trap, we use a low trapping current so that after transfer the whole trap is filled up. In such a situation, the highest energy of atom cloud is also approximately the trap top.

In the experiment, we measure the trap depth with different trapping currents, $29A$ and $36A$. The trap depth is measured to be about $70G$ consistently when scaled for $100A$ trapping current. This is consistent with our theoretical calculation. The emphasis is that $70G$ trap depth is as high as conventional gigantic trap can provide, which needs kilo-watts power supply.

2.6.4 Mini-Trapping Frequency Measurement

Beside trapping lifetime, power dissipation and trap depth, another important parameter for a magnetic trap is the trapping frequency. High trapping frequency will ensure short-time evaporation and reduce the vacuum requirement. Here I will present three independent ways to measure and verify the trapping frequency for Mini-Trap.

Spacial oscillation measurement immediately after transfer

When the atoms are transferred from upper rectangular coil to the Mini-Trap, initial oscillation will occur due to axial misalignment and initial momentum. This is shown on Fig 2.21. To have a good transfer, we would like to minimize this kind of oscillation by tweaking the time when the upper rectangular coils will be off and the time when Mini-Trap current will ramp up. Here we would like to use such a oscillation to calculate the trapping frequency.

After the transfer, without evaporation, the cloud is still very hot, meaning $k_B T \gg \mu_m B_0$, so we are in the linear regime. The oscillation frequency, $43Hz \pm 1Hz$ shown on the figure, is the frequency for atoms to bounce back and forth in the trap. Although it is not in the harmonic regime yet, this frequency indicates the order of our trapping frequency in axial direction. Actually, since this oscillation frequency is quite close to the real trapping frequency in axial direction, we can say that in a large range the trap is close to a harmonic trap in axial direction.

Oscillation in single well after kick

The experiment is done on May 2nd, 2006. Two arbitrary waveform generators(AWG) are combined by a T connector to independently control the current in the upper rectangular coil. One of the AWG is used to generate the pulse for magnetic elevator and the other one is used to generate the momentum kick. After evaporative cooling down to $805Mhz$ for $|2, 2\rangle$ state, a fix length, $5ms$, and fixed current, $11.3A$, pulse is applied on the upper rectangular trap. After the pulse, a variable amount of holding
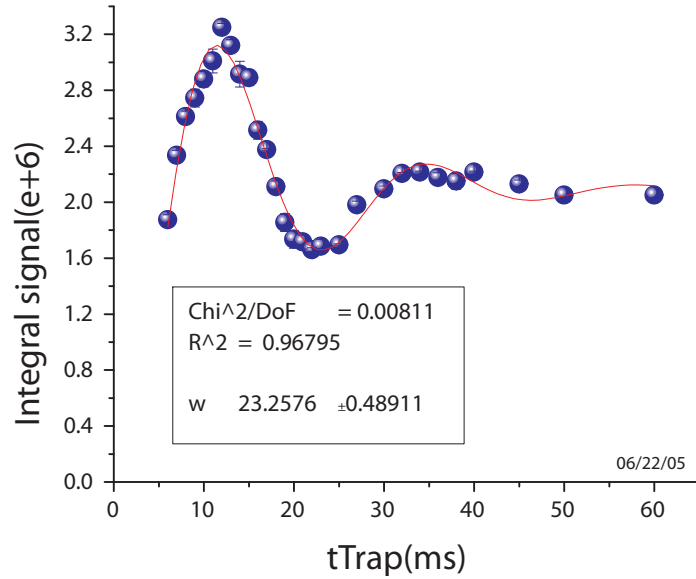
Figure 2.21: Oscillation in axial direction after transfer

time is used to observe the atom motion. During the whole process, the IP current is constant at $100A$ and the trap bottom is set at $0.4G$. When the atom gains a momentum, it will swing in the axial direction, which has been observed and shown in Fig. (2.22). The fitted oscillation frequency is $54 \pm 1Hz$.
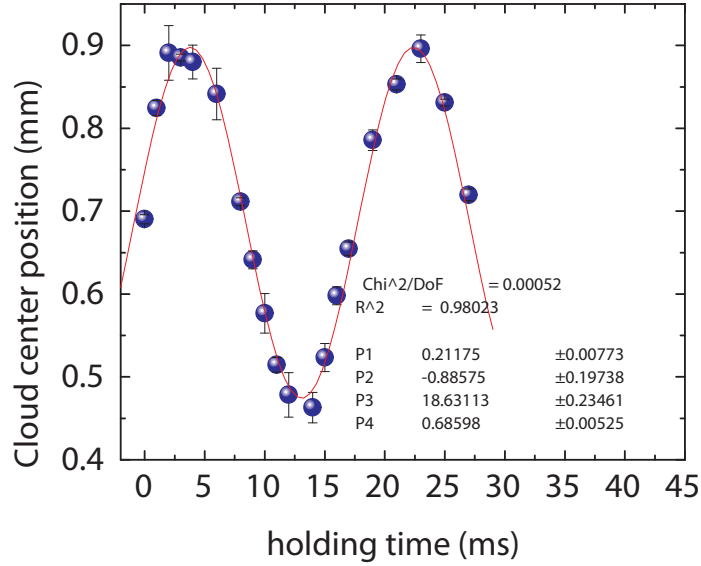
Figure 2.22: Oscillation in axial direction after momentum kick in the single trap

In this case, after evaporation down to $6\mu K$, we are already in the harmonic regime, the measured frequency is what we expect for axial direction. This value is also close to the prediction of theoretical model.

The reason to use the upper rectangular coils instead of lower rectangular coils for the momentum kick is that their center are closer so that we don't disturb the cloud too much. This has been experimentally verified.

Parametric heating measurement

Spatial oscillation, as we have discussed, is a convenient and easy way to measure the trapping frequency in axial direction but we cannot use it to measure the frequency in the radial direction. First, because the trapping frequency is quite high, it is hard
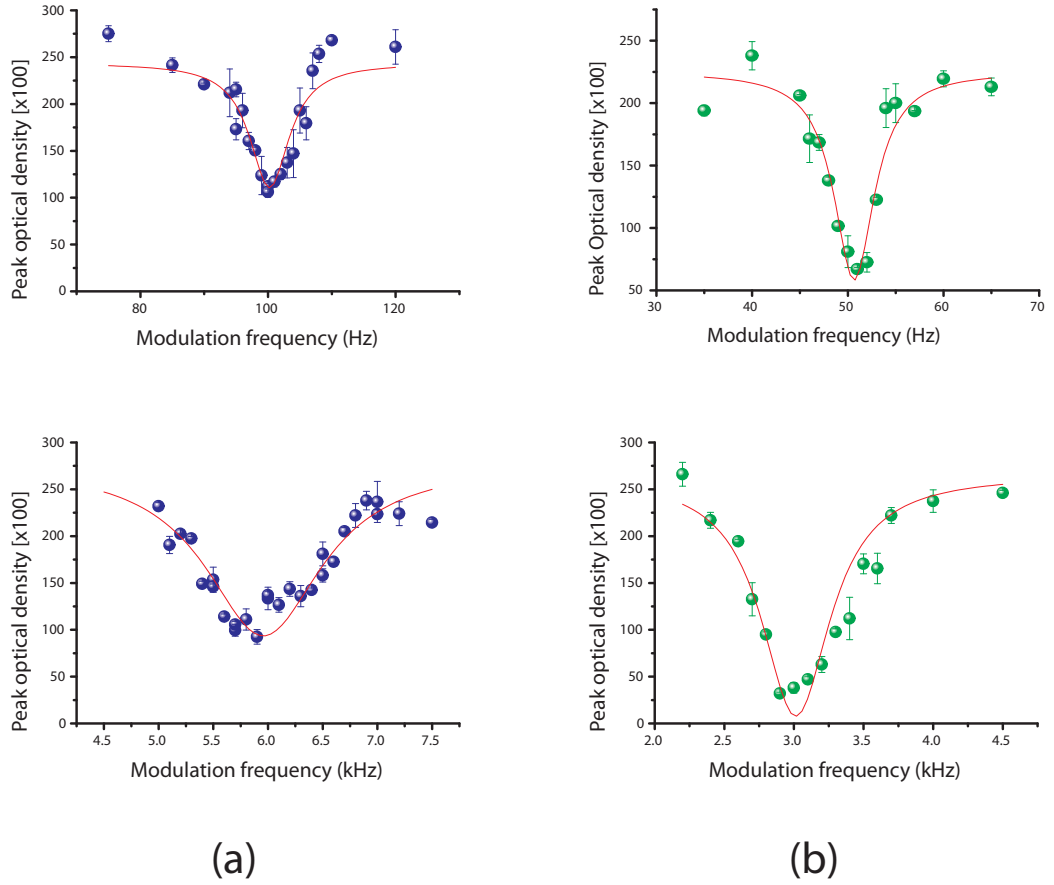
Figure 2.23: Parametric heating to measure trapping frequency. The top row is for axial direction and the bottom row is for radial direction. (a) $\omega = 2\omega_0$ for n=1, in blue; (b) $\omega = \omega_0$ for n=2, in green

to observe that. Second, we don't have access along the axial direction to see that. One of the alternatives is to use parametric heating, which has been widely used in cold atoms research [51, 52].

After evaporation down to $6\mu K$, we superpose $3A$ single frequency AC current with the $100A$ trapping current for $10S$ and keep the trap bottom fixed at about $0.4G$. Thus we modulate both the trap depth and trapping frequency. If we suppose the modulation frequency is ω and the trapping frequency is ω_0, when the condition $\omega = 2\omega_0/n, n = 1, 2, ...$ are satisfied [53], the parametric process will heat up the atom cloud and hot atoms will escape from the trap. This means there will be a dip on the absorption image when the resonant condition is satisfied.

Fig. 2.23 shows the dips observed in the experiment. We can clearly see that there is one dip around $100Hz$ and the other is around $6kHz$ with Lorentzian fitting. Since we know from spatial oscillation that the axial trapping frequency is around $50Hz$, we can conclude that we observed the $2\omega_0$ resonant condition for axial and radial direction. The axial trapping frequency is $\omega_\parallel = \omega_z = 2\pi \times 50$ Hz and the radial trapping frequency is $\omega_\perp = \omega_x = \omega_y = 2\pi \times 3$ kHz for $100A$ trapping current and $0.4G$ trap bottom. The higher order parametric heating is also observed and shown on the figure.

Along the axial direction, assume harmonic trapping, we have:

$$\frac{\partial^2 B}{\partial z^2} = \frac{m\omega_\parallel^2}{m_F g_F \mu_B}$$

where $m_F = 2$ and Landé factor $g_F = 1/2$. From this formula we can calculate the radial curvature as $120G/cm^2$. From equation 2.4, we have:

$$\frac{\partial^2 B}{\partial r^2} = \frac{B_r'^2}{B_0} - \frac{B_z''}{2}$$

Plug in the axial gradient, we can calculate the radial gradient as $\frac{\partial B}{\partial r} = 420G$, which is quite close to our theoretical calculation.

2.6.5 Temperature measurement with TOF
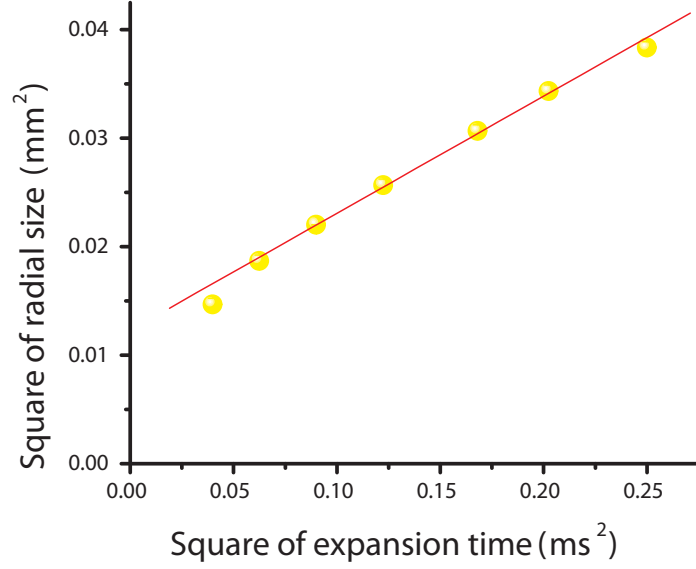
Figure 2.24: Typical time of flight plots. x axis is the square of time for expansion and y axis is the square of cloud size with Gaussian fit.

Time of flight(TOF) is one of the standard techniques in cold atom experiments to map out the momentum distribution of the atom cloud by turning off the trapping field. This is impossible for permanent magnetic trap [54]. In absence of collision, when the field is off, each atom will fly with the momentum of that moment. When the cloud grows much larger than the initial size, the initial size can be ignored and it is well approximated by momentum distribution. For classical gas with momentum $\overrightarrow{p}$, temperature T and mean velocity $v = \sqrt{k_B T/m}$, this is Boltzmann distribution:

$$
\begin{aligned}
n_p(\overrightarrow{p}) &= n_0 exp\left(\frac{-E}{k_B T}\right) \\
&= n_0 exp\left(\frac{\frac{-p^2}{2m}}{k_B T}\right) \\
&= n_0 exp\left(\frac{-(mv)^2}{2mk_B T}\right) = n_0 exp\left(\frac{-(mx)^2}{2mk_B Tt^2}\right)
\end{aligned}
$$

$$= n_0 exp\left(-\frac{x^2}{2\sigma^2}\right) \tag{2.10}$$

thus we have:

$$T = \frac{m\sigma^2}{k_B t^2} \tag{2.11}$$

where σ is the gaussian fitted size and t is the expansion time.

A typical TOF figure is shown in Fig. 2.24 According to equation 2.11, the square of radial/axial size versus the square of expansion time is linear and the slope indicates the temperature of the cloud.

It is important that the turning-off speed of the trap is faster than the oscillation speed for atoms so that we will not modify the atomic distribution. In the experiment we manage to turn off the trap within $50\mu S$, which is much higher than our kHz level trapping frequency. The reason for such a fast turn off is the very low conductance of the trap.

2.6.6 Tweaking Trapping Properties

In the experiment to measure the trap bottom, we have used Zeeman transition for $F = 1$ state. The reason to use $F = 1$ in stead of using $F = 2$ state is to take advantage of only one trapping state for $F = 1$, $|1, -1\rangle$. That way we will have simplified situation. One Zeeman transition will get atoms out of the trap. For $F = 2$, both $|2, 2\rangle$ and $|2, 1\rangle$ are trapped states. Zeeman transition within hyperfine state will not work well. For such a state we would need a hyperfine transition which will flip atoms from trap state $|2, 2\rangle$ to un-trapped state $|1, 1\rangle$.

Experimentally we have observed as clear RF cut as for $F = 1$ state, which has been shown in Fig. 2.25. Trap bottom is identified for certain trapping current when we scan the RF frequency. The measurement is very precise with accuracy of $5mG$.

At $100A$ the trap bottom is $7G$. This is much smaller than theoretical calculation which is about $17G$. One explanation for this is the current leads. The current leads are brazed on the arc traces and part of the current flows in these traces. This current runs in opposite direction with the pinch coil field so that the pinch coil magnetic field
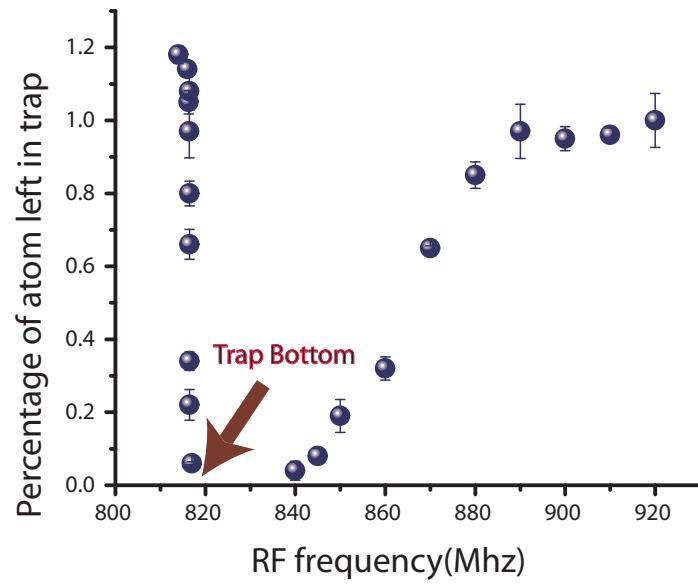
Figure 2.25: Trap bottom bottom measurement with hyperfine transition
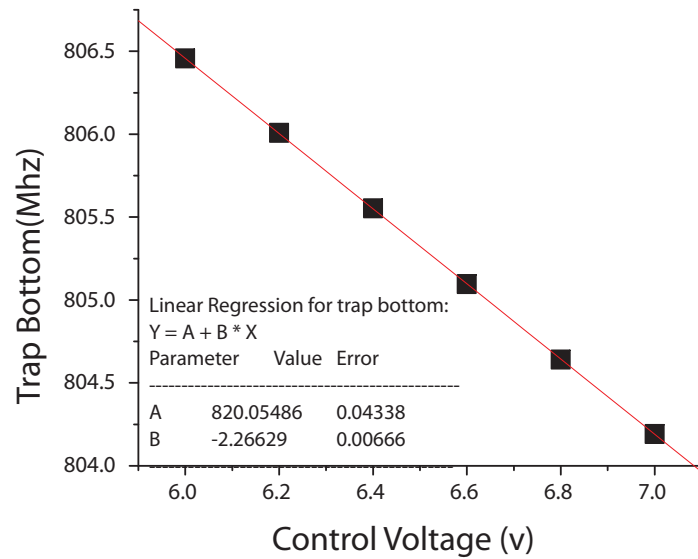
Figure 2.26: Trap bottom versus bias coil control voltage

is reduced. In our theoretical model, this was not counted in the calculation. An off-line test trap has been done and the effect of current in arc traces has been measured. we find that magnetic field in the center can be easily reversed when enough reverse current exists.

Although the axial curvature is not dependent on the trap bottom and neither is the axial trapping frequency, it is not the case for radial direction. From equation 2.5, we know that the radial trapping frequency can be adjusted by the trap bottom. $7G$ trap bottom can be easily tweaked by using a single multi-turn rectangular coil which generates an opposite magnetic field to the pinch coil field. The $10cm \times 18cm$ rectangular coil is placed about $20cm$ below the Mini-Trap. This geometric setup is far enough to ensure that the applied field in the small space of center within the trap is uniform.

The current in the bias coil is provided by a power supply programmed by a waveform generator. When constant control voltage applied, the trap bottom is set at certain level. This is clearly displayed in Fig. 2.26. The precise linear fit on the figure demonstrates our accurate control over the trap bottom and the uniformity of our bias field.

2.7 Integrated data analysis environment

Most of our data are images from absorption imaging. We have discussed the image acquisition process in the optical imaging section. Here we present the data analysis system.

In most cases we will deal with Gaussian shape clouds or clouds with dips or peaks. To speed up data analysis process, we created an integrated data analysis environment on top of Matlab, as shown in Fig. 2.27. The program can zoom out interest area and select cross section by choosing the center. Horizontal and vertical cross sections will be displayed and various fitting functions can be applied. Different fitting functions can be added by including extra code into the Matlab file.

Batch jobs can also be done with this program to work with multi files. Fitting results could be saved to an Excel file by selecting the option.
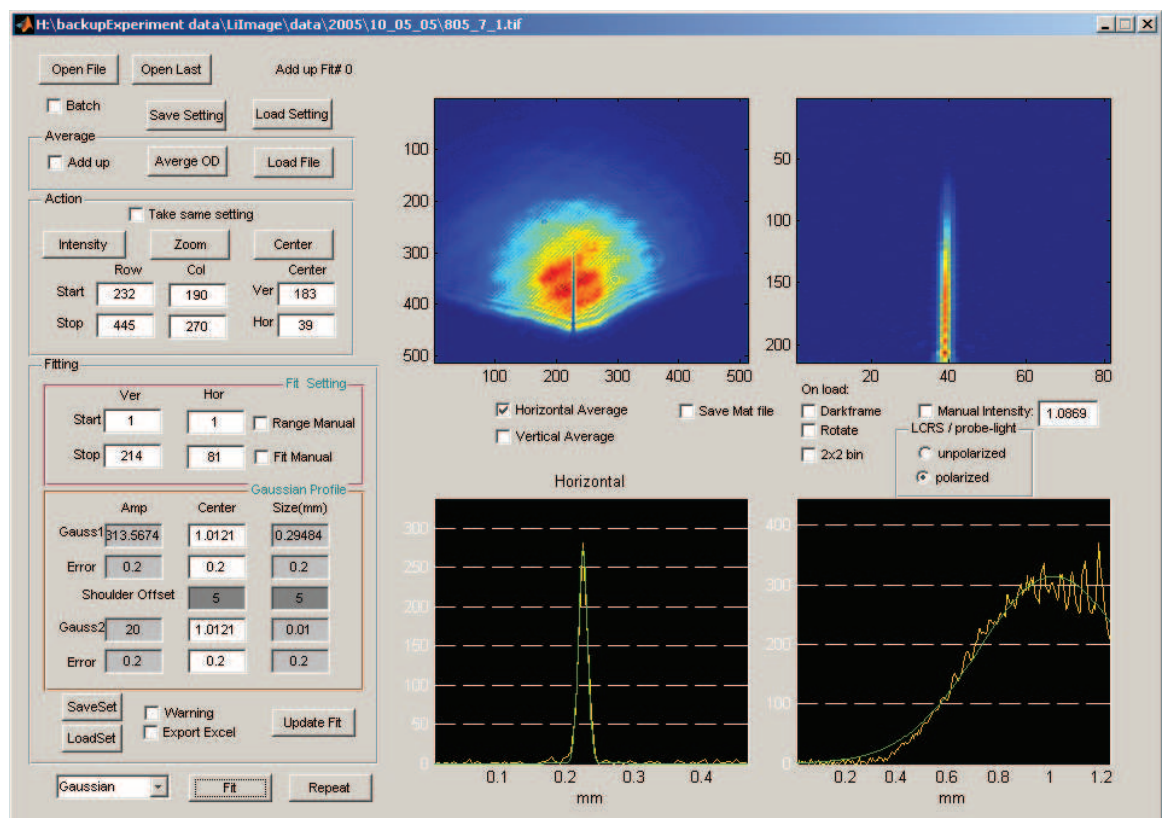
Figure 2.27: Integrated data analysis environment on the Matlab platform

2.8   What key features should be remembered for Mini-Trap?

In the end of this chapter, after presenting the apparatus setup, trap design and realization, I would like to emphasize a few facts about our system compared with other approaches. The main experimental purpose for Mini-Trap is to find a good way to create a system that optimizes key parameters for BEC experiment. It is also kept in our mind to pave the road for a portable interferometry platform for future experiments that can be carried out on a car, ship or satellite.

To demonstrate how well Mini-Trap works by comparing with other approaches, we present a table as below:

	Mini-Trap	Traditional Trap	Micro-Trap
Trapping lifetime	Excellent	Excellent	Bad
Trapping depth	Excellent	Excellent	Bad
Trapping frequency	Excellent	Good	Excellent
Trapping Volume	Excellent	Excellent	Bad
Power dissipation	Excellent	Bad	Excellent
Optical access	Excellent	Excellent	Bad
Portability	Excellent	Bad	Excellent
Control and tweaking	Good	Excellent	Excellent

From the table, we can see that compared with other magnetic trapping schemes, Mini-Trap outperforms in major features that are important for BEC experiment. Since a single current runs through the whole IP trap for our Mini-trap, we cannot independently tweak trapping frequency in each direction at will. But with the help of external bias field, this is no longer a problem as we have discussed before.

It is all these excellent merits of our Mini-Trap that make us confident to use it to achieve quantum degeneracy for ^7Li which is experimentally very hard to achieve.

Chapter 3

Quantum degeneracy of Lithium in Mini-Trap

3.1 Quantum Degeneracy in single Mini-Trap

Achieving quantum degeneracy for Lithium has been a long time pursuing goal. The first BEC state was observed in 1997 [54]. As we have discussed in the first chapter, the attractive interaction limits the number of atoms in BEC state. The growth and collapse for BEC has also been observed [55]. With the help of Feshbach resonance [56], bright soliton was observed [21]. Using sympathetic cooling, BEC state for $|1, 1\rangle$, whose scattering length is too small for direct evaporative cooling, has also been realized [57].

Unlike Rubidium and Sodium, the evaporation cooling for Lithium is a challenging task. As we have discussed in Chapter 1, this sets higher requirements on the apparatus and it is like a touchstone for the system.

3.1.1 Metastable BEC with Attractive Interaction

In evaporative cooling section of Chapter 1, we have argued that the only state that can be directly evaporative down to BEC state is $|2, 2\rangle$. For this state, its scattering length $a = -27a_0 < 0$. According to mean field theory, there is an upper limit of

number of atoms that could be in BEC state by equation 1.3. For our trap with axial frequency $\omega_z = 2\pi \times 50$ and $\omega_\perp = 2\pi \times 3$ kHz for $100A$, this corresponds to roughly 550 atoms.

3.1.2 Experimental Results in simple harmonic trap

After MOT loading for 35 seconds, we collect about 2×10^9 atoms. More atoms can be trapped in MOT with longer loading time but we find that this will not change the final evaporation results too much. These atoms, after molasses cooling and optical pumping to $|2, 2\rangle$, are transferred through series of quadruple trap and finally into Mini-Trap as we have discussed in Chapter 2. After $100ms$ trapping in the Mini-Trap, we still have 2×10^8 atoms left for further evaporation.

The very hot atoms, which cannot be trapped, fall out of trap. In this sense, the transfer is also kind of evaporation cooling. The $35s$ forced evaporation cooling is applied $5ms$ after the current in the Mini-Trap rises up. The $5ms$ time window is used to make sure the RF will not disturb the transfer. Normally $100A$ trapping current is applied and the trap bottom is precisely controlled by to bias coil to set at $0.4G$. Due to the small value of trap bottom, an external stray magnetic field will influence our experiment. We used a magnetometer to observe the magnetic field from environment.

Evaporation has been optimized piecewise with linear ramp in each segment(cite hulet paper). The intermediate frequencies and temporal positions are chosen to maximize the final phase space density. The typical absorption images after TOF at the final stage of the evaporative cooling are shown in Fig. 3.1. Because almost all of the upper half of the Mini-Trap is hidden by the edge of the vacuum chamber, we can only see half of the atom cloud. The absorption image is cut at the center. When the cloud is sufficiently small, we can see the whole atom cloud, as shown in the bottom picture. The RF frequency at the end of ramp and the temperature of the cloud are also shown on the picture.

The cloud is fitted with Gaussian shape. The temperature is calculated using
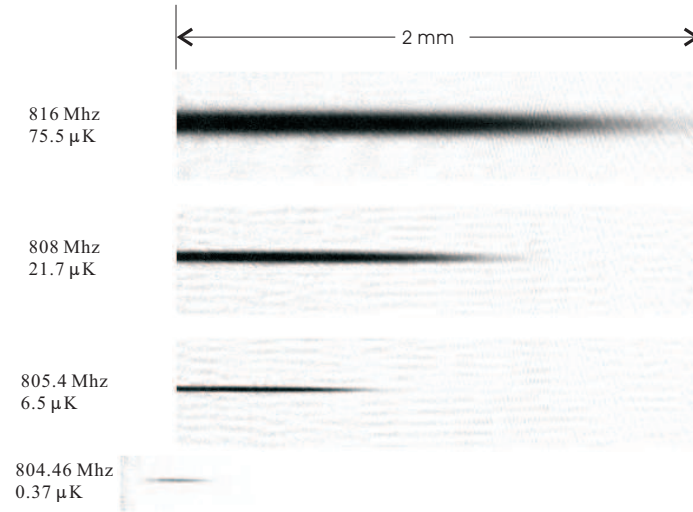
Figure 3.1: Typical absorption image during evaporation for relatively high phase space density
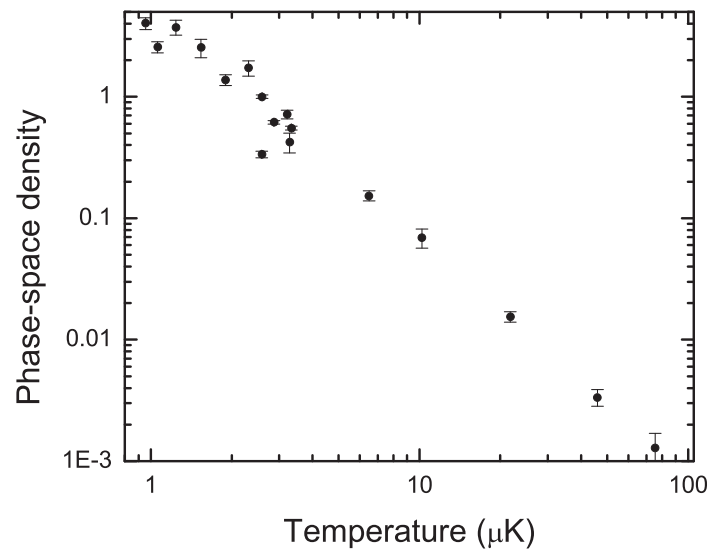
Figure 3.2: Phase space density versus temperature

equation 2.11. When the size of the cloud is large, the radial size is used for the calculation. For a short expansion time, this is about the same size as in-situ measurement. When the cloud gets colder,the radial size can change a lot during expansion and the axial size is used for the calculation. At this time, the whole cloud is in the view field. Number of atoms and phase space density can also be calculated. For different final RF cutting level, the relation between PSD and final temperature is shown in Fig. 3.2. The relation of PSD with number of atoms in the trap shown in Fig. 3.3.

Let's define the speed of evaporative cooling $\gamma = dlog(\rho)/dlog(N)$ with ρ as PSD and N as number of atoms in the cloud. The slope of PSD versus number of atoms, γ, in Fig. 3.3 is 2 in the region when PSD is between 10^{-3} and 10^{-1}. This is consistent with other group's observations [58]. With continuous lowering of the RF, we can see a reduced speed for γ to be 1. We interpret this as the dipolar loss [59, 60], which slows down the evaporative cooling. On the other hand, it also indicates that the system goes into quantum degeneracy system with higher density.

It seems the system passes the critical point, PSD=2.612, when the number of atoms is still 6×10^4. This is larger than the amount of atoms that the trap can
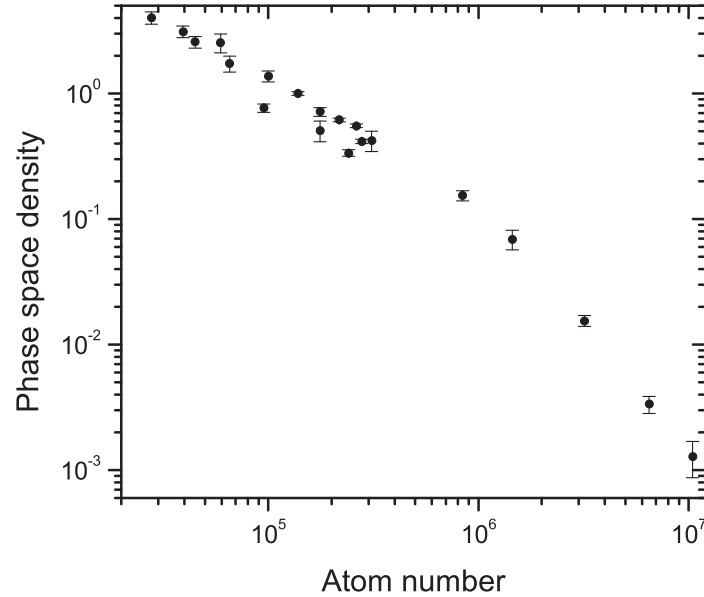
Figure 3.3: Phase space density versus atom number

support. This is because we use the same calculation for thermal cloud as well as for atoms at the time when quantum degeneracy happens. This is justified by the fact that most of the atoms are still in thermal state and it presents global trends for RF cut with the same standard. On the other hand, it is not possible to distinguish a few hundred atom from such a dominant thermal cloud. To clearly see BEC, we need to continue the RF cut much closer to the trap bottom. This is what we will do next.

(a) 2D image in false color

(b) Horizontal intersection

(c) Vertical intersection
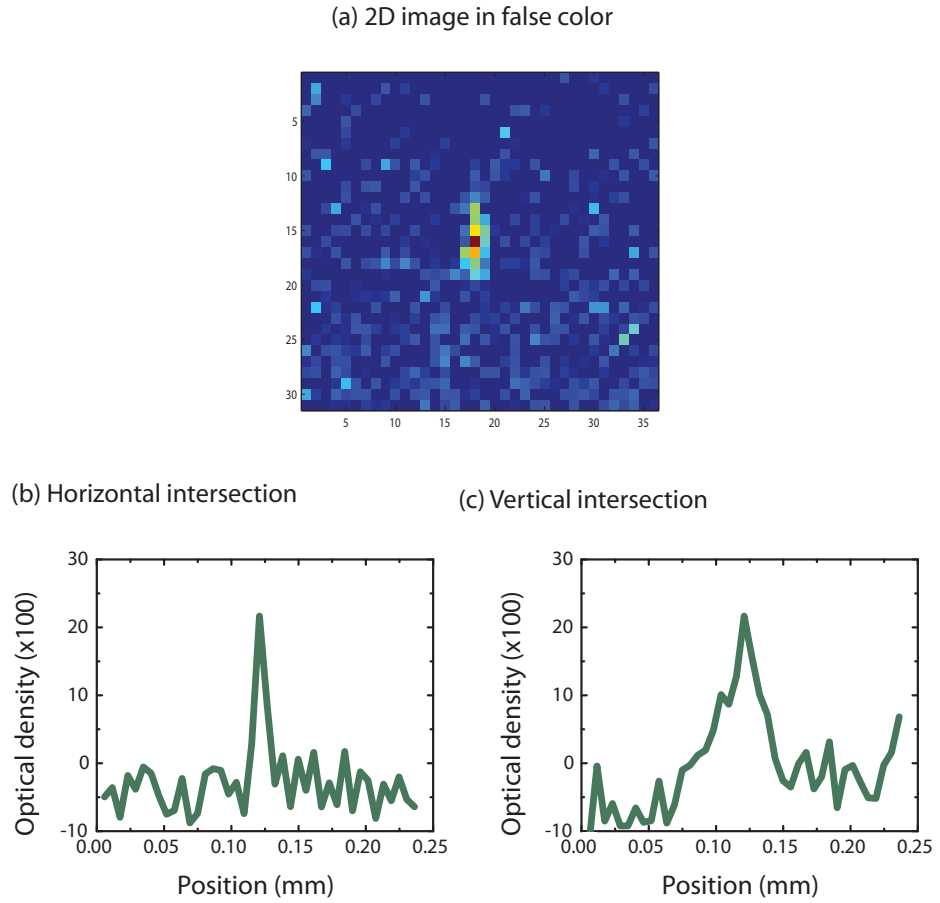
Figure 3.4: (a) Single pixel image with false color; (b) 1D cross-section along horizontal direction; (c) 1D cross-section along vertical direction

As we have discussed in Chapter 1, in free space there will be no stable BEC state for attractive interaction. It is the positive kinetic energy that is used to balance the

negative energy from interaction to ensure a meta-stable BEC state. To observe this, we can only use in-situ imaging. This means we will take pictures when the cloud is still trapped.

Experimentally, after carefully control the parameters, with RF cutting level only about $40kHz$ away from trap bottom, we can observe single pixel image, as is shown in Fig. 3.4. This image corresponds to about 100 atoms with a temperature estimated to be around $20nK$. If we consider the convolution with the imaging lenses [54], the fitted size of the cloud is about the size of a ground state with the same trapping constant. This makes it an evidence of first direct observation of Lithium BEC.

3.1.3 Two-step time of flight
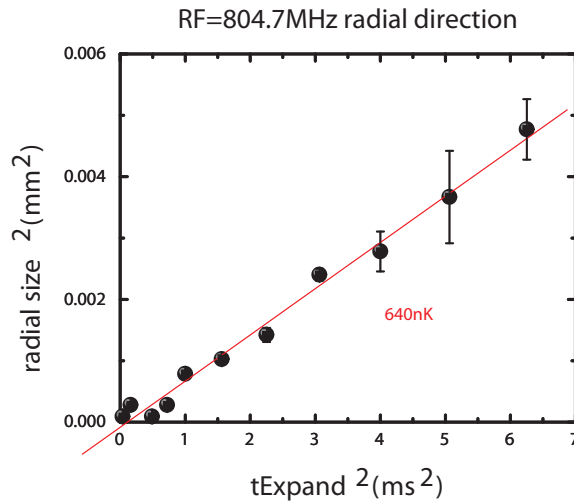
Figure 3.5: Time of flight for RF cut equals

A time of flight measurement at the final RF cut value of $804.7Mhz$ is shown in Fig. 3.5. The temperature measured is about $640nK$ for 6×10^5 atoms. This is normal as we have expected. After a sufficiently long time of expansion, the image will fill up the whole camera view field. This can introduce errors during fitting, which is shown by the error bars on the figure.

If we continue to ramp down the final RF level to produce even colder cloud,
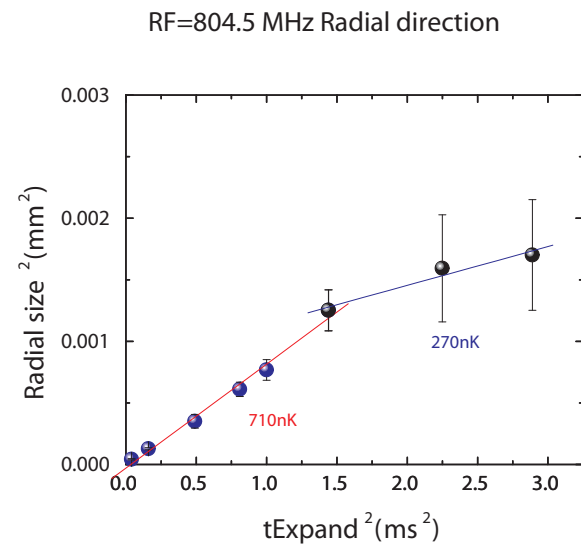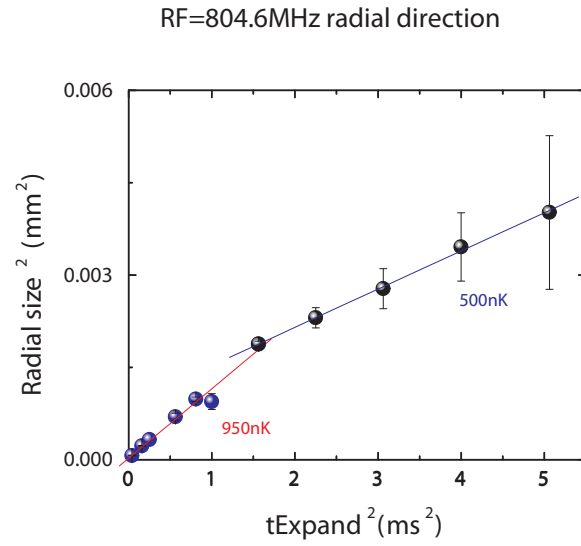
Figure 3.6: Two-step time of flight in quantum degeneracy

we can see a two-steps evaporation. The evaporation for RF level of $804.6Mhz$ and $804.5Mhz$ is shown in Fig 3.6 and the temperatures for different period are also listed on the graph. For $804.6Mhz$ there are 3×10^5 atoms and for $804.5Mhz$ there are 1.5×10^5 atoms. It can be seen from the two figures that at the beginning of the expansion the temperature is higher and this temperature atoms cool down later.

Interestingly, in the paper that describes the dynamic collapse and explosion [61], the authors observed bursts of cloud due to attractive interaction induced collapsing. For our measurement, we believe there could be a similar process. When time of flight starts, the trapping potential is gone. This means that there is no kinetic energy to balance the interaction energy. This energy is released and the atom explodes with a higher momentum. After collision with other thermal atoms, the small portion of atoms are slowed down and we observe reduced average temperature. During the process, three body collision could induce atom loss which will not be observed.

The error bars in Fig. 3.6 for the longer time of flight is due to the reduction of cloud density, which introduces fluctuation on fitting. We can ramp the RF even lower for smaller, the cloud is too dilute to be observed after TOF so it is not presented.

The two-steps TOF doesn't appear for higher RF cut, for instance $RF = 804.7Mhz$, before we get into quantum degeneracy regime. This abnormal TOF, on the other hand, is an evidence of the play of interaction and the sign for quantum degeneracy regime.

3.2 Collisional experiment in a double well

Although we have seen very interesting physics in our Mini-Trap due to the attractive interaction, more experiments can be done when we have other "knobs" to tweak. One obvious upgrade would be to divide the trap into two traps using a optical dipole trap. As we have discussed in Chapter 1, a blue-detuned gaussian shaped laser beam can be used as a potential bump to divide the magnetic trap. The good optical access of Mini-Trap makes this possible. But on the other hand, spatially aligning a μm focused laser beam with a μm size atom cloud in free space is technically very challenging. At the same time the mechanical stability for the system is required.

3.2.1 Dimple beam setup
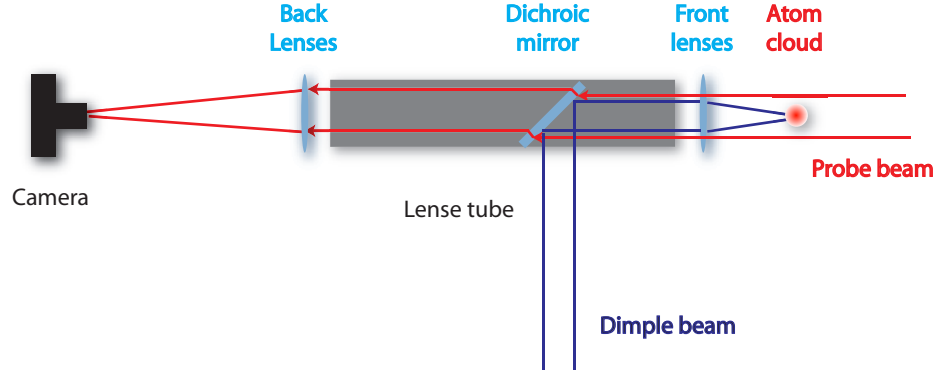
Figure 3.7: Optical alignment of dimple beam and probe beam in lens tube

The laser we used for the blue-detuned laser light, also called dimple light, is generated from Verdi laser of Coherent Inc. The single frequency laser has a wavelength of $532nm$ and powers up to $10W$. We used a half wave-plate and a polarization cube to roughly adjust the power output from laser. Two Acousto-optic modulators(AOM) is used to fine tune the power. The two AOMs are used before coupling into fiber. This ensure that we can turn off by dimple light in a fast way. A blitz shutter is used to make sure complete shut off during imaging.

The dimple beam is guided through a $5m$ fiber to the dark box where the chamber stand. The fiber is polarization maintaining and its length helps damping higher optical modes. The linear polarized beam is first collimated by a lens to diameter of $2cm$. Reflection mirrors are used to guide the beam. The dimple beam focuses at the center of Mini-Trap using the front imaging lens, the one closer to chamber. The front imaging lens should be on focal position due to our $f - 2f - f$ imaging alignment. This ensures that the beam waist hits the atom cloud. Since our dimple beam and imaging beam share the same path through the front lens, a Dichroic is used in the lens tube that holds the imaging lenses. The probe beam can go through the Dichroic and hit the camera while the dimple beam will be reflected into the chamber. This is shown in Fig. 3.7.

3.2.2   Off-line measurement of dimple beam size
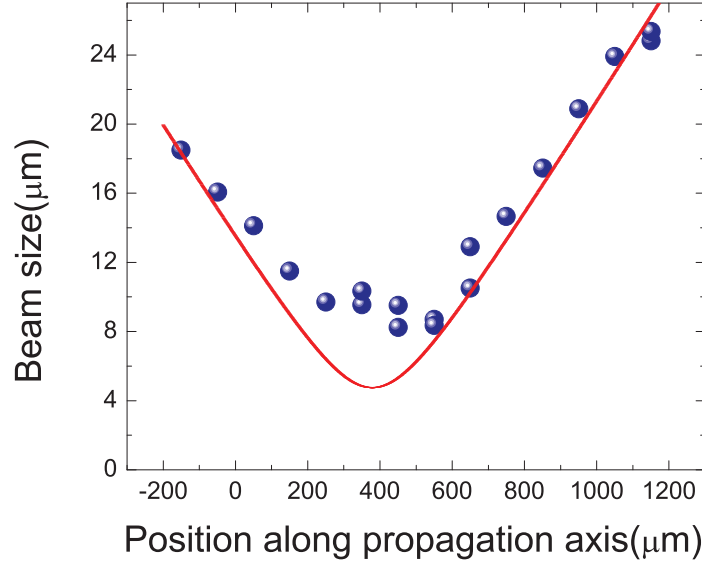
Figure 3.8: Off line measurement of dimple beam waist

Before we send the dimple beam into the chamber, we want to make sure we can tightly focus the beam with our lens. An off-line measurement was taken to measure the beam size after the focus lens. At one position along the gaussian beam propagation, we used a razor blade to partially block the beam and use photodiode to measure the power after the razor blade. This way we will have an error function after the scan. By fitting this error function for that location, we can calculate the beam size at that position. In the same way, multiple positions were measured and beam sizes at that positions have been calculated. The scan is shown in Fig. 3.8. Gaussian beam propagation function can be used to fit out this curve 1.5. Due to the scattering of the razor blade, the size we measured on the beam waist is bigger than its real value. Its size is then calculated by fitting the data on the shoulder of the curve, which is $4.56 \mu m$. If we consider the beam we send into the lens has waist about $W_{input} = 3.2mm$, the relation for gaussian beam through a lens

$$W_{output} = \frac{f\lambda}{W_{input}}$$

is satisfied, where W_{output} is the beam waist on the focal point of the lens.

The beam size has also been double-checked by using a CCD camera and the result is consistent. So we have the capacity to focus the beam down to $5\mu m$ on the focal point of the lens.

a) Dimple scheme

Atom cloud
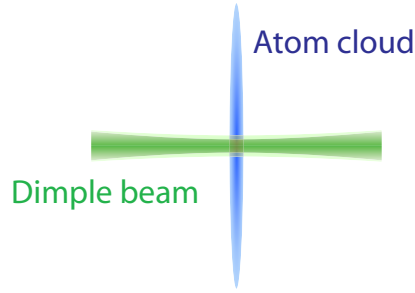
Dimple beam

b) On resonant dimple
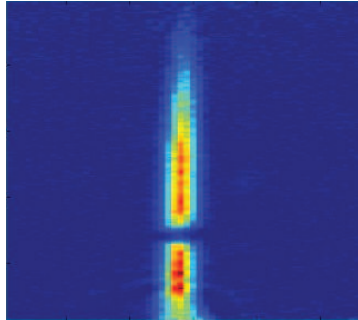
c) Blue-detuned dimple
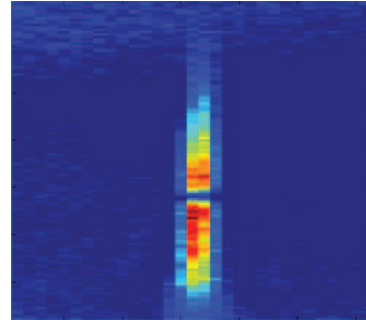
Figure 3.9: (a) Dimple scheme; (b) Atom cloud hit by on resonant laser light; (c) Atom cloud is divided by the blue-detuned dimple beam.

The dimple beam is aligned so that the focus cuts through the center of the cloud as shown in Fig. 3.9(a). To align the laser beam, we used two gimbal reflection mirror mounts with excellent mechanical stability. The distances of the guiding mirrors are set so that we can control the position of the laser beam as accurate as $1\mu m$. As I said in the beginning of this section, to coincide two μm size objects in a free space

is almost technically impossible. To do this, we followed a three-step procedure.

Since the dimple beam uses the same optical path as the probe beam to another direction, as shown in Fig. 3.7. The first rough alignment was done by aligning these two beams. This is achieved by reflecting back the residual light of dimple beam that passes the Dichroic. Although this is very small amount of light, it is enough for our CCD camera. The dimple beam is then aligned to be coincident with probe beam on the camera. After the rough alignment, a resonant light, $671nm$, is fed into the fiber. The blue-detuned dimple light can only divide the atom cloud when it is quite cold and small while resonant light can heat up and kick plenty of atoms out of trap when it is still hot and big. In this way, we reduce the alignment difficulties. A typical cut by resonant light is shown in Fig. 3.9(b). After this alignment, we are sure that the dimple beam and atom cloud overlap. The final step is to exchange the resonant light to blue-detuned laser, $532nm$ and finish the fine tuning. A typical cut is shown on Fig 3.9(c). Before the output fiber tip of the dimple laser, there is a translation stage holding the collimation lens. This was also tweaked for the smallest size of the dimple cut so that we are sure it is on focus.

3.2.3 Dimple beam stability test

The stability of the dimple pointing is a big concern. If the beam vibrates too much it will disturb the small atom cloud which will change the whole physics. To make sure the system is mechanically stable. We did an off-line test and paid attention to fix tilting freedom with strong mountings.

The off-line measurement is done by using Michelson interferometry to ensure the stability of mirror holders and also the angular resolution, which should be at level of $2ArcSec$. This is necessary to achieve $1\mu m$ accuracy with our front one-inch lens of $f = 90mm$.

The optics for dimple beam sit on a small table mount with 4 solid optical pillars. The table is as close as possible to the chamber to ensure common vibrating mode. The lens tube is fixed by two clamps onto a mounting board which sits on a strong translation stage for focal tweaking. The clamps are put at the closest distance to

the tip of the lens tube to reduce vibration.

After we have aligned the dimple beam, we measured the stability of the dimple beam with atoms, Fig 3.10. The atom profile and the dimple cut were fitted with gaussian function. Their respective centers were recorded. With increase of the power of dimple light, we can see that the center of the cloud moves. This is because the existence of dimple beam changes the potential minimum when it does not exactly coincide with the center of magnetic harmonic trap. On the other hand, we can see that the center of dimple beam doesn't change. Its center is fixed with better than $1\mu m$ accuracy. The durability of the alignment has been checked weeks after. The small migration due to mirror mount can be easily corrected.

Besides mechanical stability, the power stability is ensured by using a feedback loop to digitally program the power of the laser beam. A pickup mirror is used to pick up some light from the dimple beam after the fiber and this signal is used to feedback control the setting of AOMs before the fiber to adjust the power.
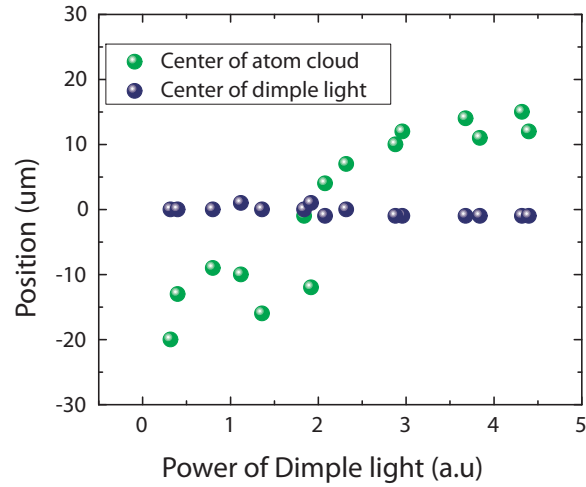
Figure 3.10: Stability test of dimple light on the apparatus

3.2.4 Collisional experiment setup and results

Armed with the well-aligned dimple beam, we can do some experiments in such a double well. Here we will talk about a classic collisional experiments. This experiment demonstrates our good control over the double well, presents an interesting phenomenon for attractive interaction and can also be used as a tool of calibration for the Schrödinger cat experiment we will discuss in next chapter.

To do the collisional experiment, we need to move the cloud along the axial axis by giving it a momentum kick. The momentum is applied by using the upper rectangular quadruple trap whose center is a little higher than the center of the Mini-Trap. A $5ms$ pulsed current runs through the quadruple trap which will temporarily change the center of the Min-Trap and move the atom cloud upwards with certain momentum. The amplitude of this kick is controlled by an waveform generator that program the current in the quadruple trap. This is shown in Fig. 3.11(a)

After the atoms slide to one side of the harmonic trap, the dimple beam is turned on to divide the trap into a double well. Without such a bump, the cloud will slide back and forth with axial trapping frequency. This is what we have used to measure the trapping frequency in Chapter 2. With the presence of such a bump, the atom cloud will collide on the barrier when it slides back and split as in Fig. 3.11(c). Hot atoms will go over to the other side of the bump and cold atoms will be bumped back. The two components will slide and collide as shown in Fig. 3.12.

A interesting phenomenon is the collision between to the two separated components in the double well. After the first collision with the dimple barrier, the two
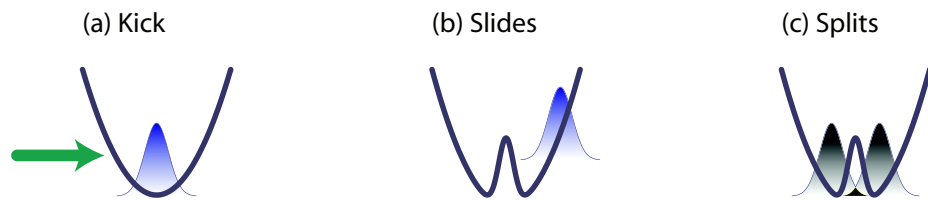
Figure 3.11: Scheme of momentum kick in a double well
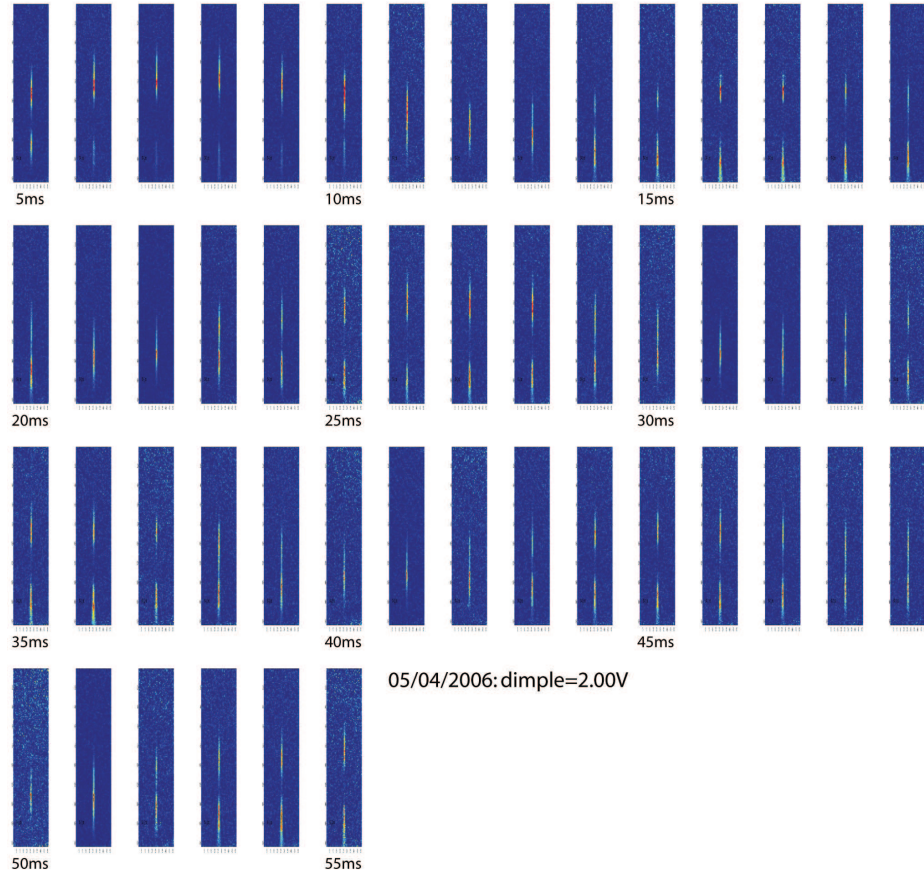
Figure 3.12: Oscillation in double well after momentum kick. RF=804.4Mhz; Dimple control voltage=2V

(a)
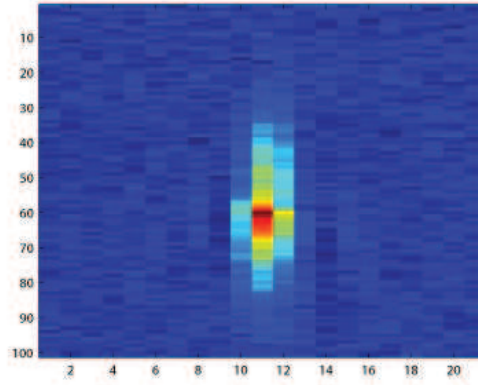
(b)
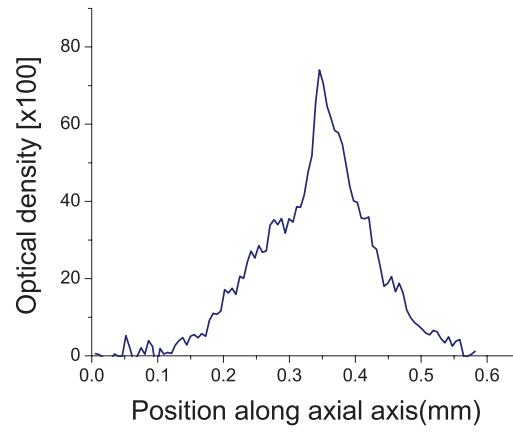
Figure 3.13: Collision of two atom clouds. (a) False color 2D image; (b) 1D cross section along axial direction

components gain momentum with different directions. After a half oscillation period, they will come back and collide. The collision of the two clouds produces a peak on top of gaussian shape, which is shown in Fig. 3.13. Similar dynamics has been discussed theoretically in [62] but no detailed calculation has been done on this. The dynamics involved during the collision process is very interesting because of the attractive interaction. This can be an object for future theoretical investigation [63].

The barrier height is estimated by the temperature of the atom cloud and the distance the cloud slides away from the center. The atom cloud be can treated with Boltzmann distribution. This is used as reference calibration for the experiment in next chapter.

Chapter 4

Schrödinger Cat: alive or dead

4.1 Schrödinger Cat

Quantum mechanics has been the most precise description of the physics world. It is not only a theory but also a whole new way to look at the world. Since it was born, it has been very successful to interpret the physics in the microscopic world(for instance, single electrons, atoms, or molecules that cannot be explained by classical pictures). But on the other hand, quantum mechanics is not so successful for the physics in the macroscopic world. Physicists have two different perspectives on this. One is to find a new way to re-interpret quantum mechanics so that macroscopic phenomena are included and the other perspective is to confine quantum mechanics in microscopic scale and find an alternative for macroscopic phenomenons. Both of these perspectives depend on a deep understanding about the special properties that can differentiate quantum mechanics from classical one.

Among all the quantum views of the world that are classically counterintuitive, two of them are especially interesting:

- Entangelment and Einstein-Podolsky-Rosen (EPR) paradox

- Non-realization and Schrödinger's Cat paradox

Entanglement, which is associated with the famous EPR experiment [64], points out that the objective local theory is a wrong concept if we keep some basic assumption

like causalities. The surprising consequence of entanglement is that we cannot assign quantum state to an individual particle or subsystem. In another words, we have to believe that an individual subsystem doesn't possess its properties by its own. Entanglement has played an important role in the emerging quantum information field, including quantum encryption, teleportation and computation [65].

Non-realization is associated with the famous Schrödinger's Cat experiment. In this chapter, we will confine our discussion to this phenomenon.

In 1935, when quantum mechanics was just born, in order to demonstrate the limitations inherent in using quantum mechanics to describe everyday phenomena, Erwin Schrodinger proposed an experiment [66]. A cat is put in a dark box with an unstable nuclei that can trigger a deadly poison. If standard quantum mechanics still holds, it will allow the cat to enter a "superposition" state of being dead and alive. This is the famous Schrödinger's Cat paradox.

$$|\Psi\rangle = \frac{1}{\sqrt{2}}(|\uparrow, \circ\rangle + |\downarrow, \bullet\rangle)$$

As an reaction to this logically untenable gedanken experiment, an idea of "decoherence" came out[67]. It proposes that the macroscopic body interacts with its "environment" so much that the quantum state gets entangled with that of the environment almost instantaneously. In quantum mechanics, superposition is valid for systems that are closed. For a real system, it always couples to the external environment which normally consists a large number of degrees of freedom. So it is not realistic to say that the cat is in a superposition of being "dead" and "alive". Instead we should consider that the state of the cat is entangled with the state of the nuclei. For such an entangled state, standard quantum mechanics tells us that any measurement on the cat *alone* will give statistical results, which is identical like a classical probabilistic mixture of two states. This means that there will be no quantum interference effect for detection after decoherence. In this sense, all predictions by quantum mechanics are indistinguishable from those made by macro-realistic scenarios which say that the "cat" is in one state or the other but not superposition of both before we open the box. Should we believe quantum mechanics or macrorealism?

Decoherence has been solidly proved in theory and with different experiments. The existence of decoherence has made people believe that the macroscopic superposition state is not observable. The question is then about what if the dissipative coupling between the system and the environment can be well controlled [68]. Can we see a macroscopic superposition state in such a case or can we see a quasi-cat? What is the well defined boundary between a 'classical' level of reality and an underlying which is governed by the quantum mechanics? At the same time, since a cat state is very sensitive to decoherence, the preparation of such a state can demonstrate good control on quantum system.

In recent years, there have been great progress on the study of macroscopic superposition, which expand people's understanding about quantum mechanics. In this chapter, I will first discuss some other systems that have pursued the cat states and then I will discuss the specialty of cat experiment based on a BEC experiment. With a numerical simulation, I will show that our system can be used as the platform for a cat state and discuss three different detection schemes to distinguish the cat state from classical mixtures. After that, I will go over the experimental set up and preliminary data we have gotten on such an experimental setup.

4.2   Other Schrödinger Cat experiments

Achieving macroscopic superposition has been a main effort in the last twenty years. Many different systems have been proposed and tested, such as photons in a microwave cavity [69], laser cooled trapped ions [70], superconductors [71, 72], C_{60} molecules [73] and nano-scale magnet [74]. In this section I will review a few experiments and discuss different approaches that have created the superposition in macroscopic or mesoscopic level. I will also discuss the way coherence has been detected and the dynamics of decoherence in each individual system. This is going to serve as a reference for our system design and considerations.

The first experiment will show the decoherence induced by measurement. The second experiment will show an elegant way to couple internal and macroscopically external freedom with Raman laser beam. The third experiment spectroscopically

demonstrated macroscopic superposition in a qubit-like system.

4.2.1 Mesoscopic quantum coherence in cavity QED

When we use a macroscopic "meter" or "cat" to measure a quantum system, the quantum superposition will be turned into a statistical mixture from which we can gather information. The macroscopic meter can be considered as a large reservoir of microscopic states. This macroscopic coupling or superposition makes the decoherence happen too fast to be observed in the lab but mesoscopic coupling with a few quanta are expected to decohere in a time scale that can be possibly observed.

In the experiment [69], an "atom-meter" system was set up and the decoherence process due to coupling to an adjustable mesoscopic "meter" was observed. The system involved a two level Rydberg atom that was coupled to a quantum oscillator. The quantum oscillator was used as the "meter", which was in a coherent state [75]. The quantum oscillator is in the cat-like state. In the experiment it was a radiation in a cavity. The entangled state has been defined as:

$$|\Psi\rangle = \frac{1}{\sqrt{2}}(|e, \alpha e^{i\phi}\rangle + |g, \alpha e^{-i\phi}\rangle)$$

In the equation $|e\rangle$ and $|g\rangle$ are the state for the atom. $|\alpha| = \sqrt{n}$ is the amplitude of the coherent state where n is the oscillator quanta and ϕ is the phase.

Essentially, this is like a double slit interference experiment for a single atom with a "meter", a "cat", which can determine which "path" the atom is taking. The stronger coupling, the more degree of freedom of the reservoir is involved and the more information we can extract from the "meter". The interference will disappear when this coupling is strong enough and available for measurement even when there is no measurement. When the coupling is weak, we have a "cat", which is the radiation in the cavity, in a mesoscopic superposition state. The coherence between the atom and the meter was checked by a double atoms experiment. This experiment demonstrated a way to control the strength of the coupling between environment and the quantum system and allowed continuous scan from microscopic to macroscopic.

4.2.2   Mesoscopic quantum coherence in a harmonic trap

Creating a Schrödinger Cat in a harmonic oscillator has the advantage that the dispersion of the wave packet can be neglected. In the experiment [70], a cat state by superposition of two coherent motional wave states in a harmonic trap for an ion was demonstrated. The process to create cat state is shown in figure 4.1. (A) Single ion is
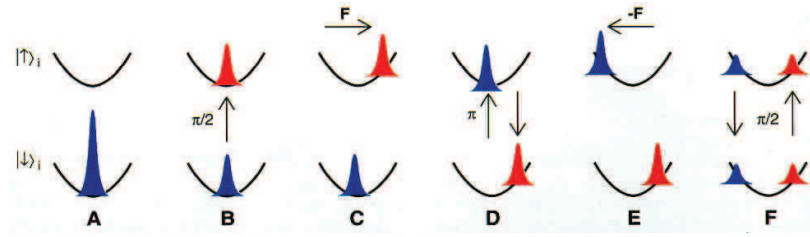
Figure 4.1: Evolution of the position-space atomic wave packet entangled with the internal states (C. Monroe et al. 1996).

laser cooled to the ground state of the RF harmonic trap. (B) a $\pi/2$ pulse entangles the internal state $|\uparrow\rangle$ and $|\downarrow\rangle$ with the ground state $|0>$ to $\frac{\sqrt{2}}{2}(|\uparrow,0\rangle + |\downarrow,0\rangle)$. (C) A raman beam working as selective displacement operator changes the spatial ground state to motional coherent state which entangles with the internal state $|\uparrow\rangle$. (D) A π pulse swaps the internal state. (E) A reversed displacement operator is applied. (F) A $\pi/2$ pulse splits the states for final detection.

After step D, the state is in a traditional Schrödinger Cat state with the motional coherent state as the mesoscopic "cat". The step E is used to detect such a state. After step E, the system is in:

$$|\Psi\rangle = (|\downarrow\rangle_i|S_-\rangle_e - i|\uparrow\rangle_i|S_+\rangle_e) \tag{4.1}$$

where

$$|S_\pm\rangle_e = \frac{|\alpha e^{-i\phi/2}\rangle_e \pm e^{i\delta}|\alpha e^{i\phi/2}\rangle_e}{2}$$

In the formula, i and e are used to indicate internal and external freedom respectively. From equation(4.1) we can see that the mesoscopic states de-entangled with the microscopic internal states. When we select the event of one of the internal state, for

instance $|\uparrow\rangle$, the system is still in a superposition of two mesoscopic states. This is *indeed* a state of superposition of two mesoscopic states. The parameters α, ϕ, δ are experimentally tweakable. When $\delta = 0$ and $\phi = \pi$, the state $|S_\pm\rangle_e$ is the even and odd cat state respectively.

Unconditional probability measurement for the atom in one of the internal state has been shown to change according to the phase parameter ϕ. Interference pattern has been used to verify that the state has coherence instead of a probabilistic mixture.

For such an ion system, decoherence has also been observed [76]. Different from cavity experiment [69], where the decoherence is induced by coupling with ambient reservoirs, the decoherence can be controlled and designed. Recently a six-atom Schrödinger cat hsa also been realized in an ion system [77].

This experiment demonstrated an elegant way to couple the internal freedom with external ones by Raman beams. This technique can also apply into our system.

4.2.3 Macroscopic quantum coherence in superconductor

The previous two experiments can be well used as demonstrations of superposition for two mesoscopic states but it is hard to define them as macroscopic experiments. To discuss macroscopic superposition, we will discuss some qubit [78] experiments with superconductors.

The behavior of electron superfluid is completely determined by a single wavefunction. The two primary types of superconducting qubit, charge qubit [79] and flux qubit [71, 72], are directly related to the amplitude and phase of the wavefunction.

For a Josephson Junction that connects between superconductors, Fig. 4.2, two kinds of energy should be considered. $E_C = 4e^2/2C$ is the Coulomb charging energy and E_J is the strength of the coupling across the junction. When $E_C > E_J$, local interaction dominates tunneling, the circuit tends to fix the number of Cooper pairs. This is a charge qubit. When $E_C < E_J$, tunneling dominates and the total phase difference around a close loop in the circuit must be a multiple of 2π. This is a flux qubit.

For both the charge qubit and flux qubit, under proper conditions, the potential

energy of the system looks like a double well. Fig. 4.3(A) shows the effective potential energy changes according to the circulating current in a flux qubit. $|1\rangle$ and $|2\rangle$ are the two lowest energy levels. When the trap is asymmetric, the two states localize to a prospective well. One state corresponds to clockwise circulation and the other corresponds to counterclockwise circulation. When the trap is symmetric, due to the tunneling, the energy eigenstate becomes the superposition of the localized states and the lowest two energy levels are shown in Fig. 4.3(B). When tunneling is zero, as the yellow line in Fig. 4.3(A), the two line in Fig. 4.3(B) should cross. It is tunneling
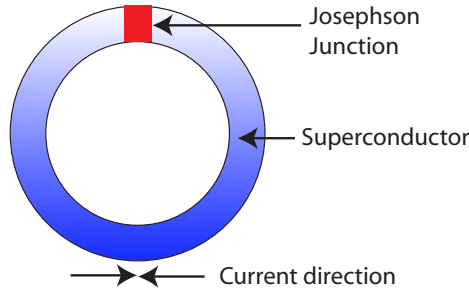
Figure 4.2: A schematic of the superconducting quantum interference device(SQUID) device.
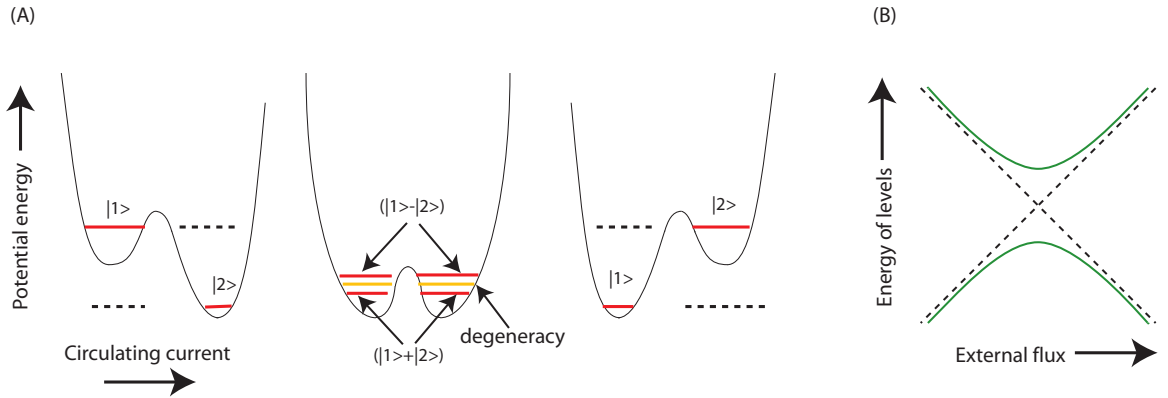
Figure 4.3: (A)The variation of the potential energy with current at three different values of the external magnetic flux through the ring. (B)The energy levels of the two lowest energy levels of the system (y-axis) as a function of the externally applied flux

that induces the energy "splitting" so that the crossing is avoided. The superposition state will manifest itself as a coherent oscillation in time domain. The oscillation frequency is related to energy splitting. The similar arguments apply to charge qubit.

Since the system involves billions of electrons, apparently it is a macroscopic system. The spectroscopic experiments [71, 72] have observed the variation of the energy splitting, which provide a strong evidence for macroscopic superposition. But still we cannot definitely rule out the view of macrorealism. A time domain measurement will be needed to verify whether the "cat" is dead already before we open the box.

We will find that the situation in superconductor is closely analogous to our double well system that we will discuss later.

4.3   Atomic Schrödinger Cat

We have talked about decoherence in a cavity system, cat state with an ion and cat state with superconductor systems. The first two is mesoscopic but we can apply elegant control to couple the internal freedom with macroscopic states. The superconductor superposition is macroscopic, although a time domain observation is still needed, but we don't have exquisite precision control. BEC is a good candidate for setting up a cat state since it possesses spatial and temporal coherence and it is macroscopic(or mesoscopic). The reason for a macroscopic cat to be important is that the utility of a cat state increases with the number of particles [80]. On the other hand, as we have discussed, the closer to macroscopic, the more rapidly decoherence will happen and the state will be more fragile. Although this kind of fragility can be used as sensor to test external perturbation, it also puts a huge amount of challenge to create such a state.

Since the creation of BEC and the demonstration of its coherent properties [11, 81, 82, 83, 20, 19], it has been actively discussed to use BEC as the working horse for a Schrödinger Cat. Spatial double well BEC [84, 85], overlapping BEC with different hyperfine states [86, 87, 88, 89], continuous quantum measurement to drive into superposition [90, 91], attractive system in 1D optical lattice [92] and cat states in momentum space [93] have been theoretically explored. There are also many concerns

about the decoherence and how to make the cat more robust [94]. In this section, we discuss theoretically and experimentally about a textbook simple way to create a cat system with negative interaction BEC and ways to detect such a state.

In this section we will discuss basic physics pictures, numerical simulation, concern about adiabatic process and methods of detection. This is going to serve as the theoretical background of our experimental design.

4.3.1   Basic picture: Bose-Hubbard model in double well

Bose-Hubbard model has been successful to describe the dynamics in an optical lattice [95], where a simplified model for a double well system with two mode approximation [96, 97] has been used. The two-mode approximation neglects all modes except the condensate modes. This means that we will ignore the atoms which have left the condensate mode due to collisions at zero temperature. The basic underlying physics is the competition between tunneling across the barrier of the double trap and the interaction between bosons in the trap. This is very similar to the superconductor system that we have discussed before.

Consider the atoms are loaded into a symmetric double well potential and the hamiltonian can be written as:

$$\hat{H} = \int d^3r \hat{\Psi}^\dagger(r)[-\frac{\hbar^2}{2m}\nabla^2 + V_{trap}(r)]\hat{\Psi}(r) + \frac{U_0}{2}\int d^3r \hat{\Psi}^\dagger(r)\hat{\Psi}^\dagger(r)\hat{\Psi}(r)\hat{\Psi}(r) \quad (4.2)$$

where $\hat{\Psi}$ is the annihilate field operator for atoms in Heisenberg picture, m is the mass of the boson, and V_{trap} represents the potential of the double well. The interaction between atoms is characterized by $U_0 = 4\pi a\hbar^2$, where a is the two body s wave scattering length.

Standard quantum mechanics tells us that the wave functions in a double well for the single atom ground state and first excited state are symmetric and anti-symmetric respectively. We can denote them as $\psi_s(r)$ and $\psi_a(r)$. The energy gap between this two states depends on the tunneling for a single atom from one side to the other. When the barrier is thick or high enough, the tunneling is compressed and there will be an energy degeneracy. Suppose the tunneling frequency is γ. Since the energy

$\hbar\gamma$ is much less than the gap between the first and second excited states, we only consider the two modes, the ground state and the first excited state. Assuming two localized states ψ_L and ψ_R,

$$\psi_L(r) = \tfrac{1}{\sqrt{2}}[\psi_s(r) + \psi_a(r)]$$
$$\psi_R(r) = \tfrac{1}{\sqrt{2}}[\psi_s(r) - \psi_a(r)]$$

(4.3)

We can expand $\hat{\Psi}(r)$ with these two modes and we have:

$$\hat{\Psi}(\mathbf{r}, t) = \hat{c}_L(t)\psi_L(r) + \hat{c}_R(t)\psi_R(r)$$

(4.4)

where $\hat{c}_L$ and $\hat{c}_R$ are the bosonic atom-annihilation operators for left and right modes. If we insert equation (4.4) into the many body hamiltonian (4.2), we arrive at the two mode Bose-Hubbard model:

$$\hat{H} = -\hbar\gamma(\hat{c}_L^\dagger \hat{c}_R + \hat{c}_R^\dagger \hat{c}_L) + \frac{\hbar g}{2}(\hat{c}_L^{\dagger 2}\hat{c}_L^2 + \hat{c}_R^{\dagger 2}\hat{c}_R^2)$$

(4.5)

where $g = \frac{U_0}{\hbar} \int d^3r |\psi_L(r)|^4$ describes the two-body interaction inside trap and $\gamma = \int d^3r\psi_L(r)\left[-\frac{\hbar^2}{2m}\bigtriangledown^2 + V_{trap}(r)\right]\psi_L(r)$ denotes the tunneling frequency. It has been assumed that the atomic oscillation can be neglected in the overlapping regions for the double well. $n_L = \hat{c}_L^\dagger \hat{c}_L, n_R = \hat{c}_R^\dagger \hat{c}_R$ and $n_L + n_R = N$ with N as the total number of atoms in the trap are also assumed.

For such a system, the Hilbert space can be written as:

$$|q\rangle = |n_L, n_R\rangle = |\frac{N}{2} + q, \frac{N}{2} - q\rangle = \frac{\hat{c}_L^{\dagger n_L}\hat{c}_R^{\dagger n_R}|0\rangle}{\sqrt{n_L! n_R!}}$$

(4.6)

where $q \subset [-\frac{N}{2}, \frac{N}{2}]$. Note that we can write the operator for the total number of atoms and operator for half of the number difference between two modes as:

$$\hat{N} = \hat{c}_L^\dagger \hat{c}_L + \hat{c}_R^\dagger \hat{c}_R$$
$$\hat{n} = \tfrac{1}{2}(\hat{c}_L^\dagger \hat{c}_L - \hat{c}_R^\dagger \hat{c}_R)$$

(4.7)

With these notations we have:

$$\hat{N}|q\rangle = N|q\rangle \quad \hat{n}|q\rangle = q|q\rangle.$$

So $|q\rangle$ is the eigenstate for the operator $\hat{n}$ and q is the eigenvalue.

If we expand the wavefunction with respect to the Fock states basis we have:

$$|\Psi\rangle = \sum_q \Psi_q |q\rangle \tag{4.8}$$

And we know that:

$$\hat{c}_L^\dagger |n_L, n_R\rangle = \sqrt{n_L + 1}|n_L + 1, n_R\rangle \quad \hat{c}_L|n_L, n_R\rangle = \sqrt{n_L}|n_L - 1, n_R\rangle$$
$$\hat{c}_R^\dagger |n_L, n_R\rangle = \sqrt{n_R + 1}|n_L, n_R + 1\rangle \quad \hat{c}_R|n_L, n_R\rangle = \sqrt{n_R}|n_L, n_R - 1\rangle \tag{4.9}$$

If we assume equation (4.8) is an eigenstate with energy E and apply the hamiltonian in equation (4.5) we will have a matrix in the Hilbert space as:

$$\frac{E\Psi_q}{\hbar} = -\gamma(t_{q-1}\Psi_{q-1} + t_q\Psi_{q+1}) + gq^2\Psi_l \tag{4.10}$$

It can be easily verified that $t_q = \sqrt{\frac{N}{2}(\frac{N}{2} + 1) - q(q + 1)}$.

Before we proceed to solve this simple two-mode model for the system, we can consider some simple cases.

In the extreme case, when there is no atomic interactions, the ground state of the Hamiltonian (4.2) is a coherent[1] state [98]. It can be written in our Hilbert Fock states basis as:

$$|g\rangle = 2^{-N/2} \sum_{-N/2}^{N/2} \sqrt{\binom{N}{q}} |q\rangle$$

This is a binomial distribution of the Fock states. When the number of atoms is large, this is going to approximate a Gaussian distribution with $\sigma_c = \sqrt{N/2}$ and

---

[1]For a confined system, it is not strictly correct to define a coherent state since the number of atoms is fixed. For large number of atoms, this required fluctuation is small and can be ignored. So we can approximately say that it is a coherent state. In the later of this chapter, the same convention applies.

$\Psi_q^C \approx \left(\frac{2}{N\pi}\right)^{1/4} e^{-q^2/N}$

Consider another extreme case that the tunneling frequency is zero and there is only interaction term. The system Hamiltonian (4.2) now becomes $\hat{H} = \frac{\hbar g}{2}(\hat{c}_L^{\dagger 2}\hat{c}_L^2 + \hat{c}_R^{\dagger 2}\hat{c}_R^2)$. With definition of (4.7) and after ignoring a constant term, the system hamiltonian can be written as:

$$\hat{H} = \hbar g \hat{n}^2.$$

Since $\hat{n}^2|q\rangle = q^2|q\rangle$, For $U > 0$, the lowest energy is for the case when $q = 0$ which corresponds to a single Fock state $|0\rangle = |N/2, N/2\rangle$. For $U < 0$, the lowest energy is for the case when $|q| = max(|q|) = N/2$. This corresponds to a doubly degenerate state which can be written as:

$$\frac{1}{\sqrt{\alpha^2 + \beta^2}}(\alpha|N/2\rangle + \beta|-N/2\rangle)$$

where α and β are arbitrary complex numbers. When $\alpha = \beta$ we have the maximized Schrödinger cat state:

$$|SC\rangle = \frac{1}{\sqrt{2}}(|N/2\rangle + |-N/2\rangle)$$

A general argument can apply to equation (4.10). Due to the quadratic term of $\hat{n}$ in the Hamiltonian, we will find that for a positive interaction system, where $a > 0$, the system is in favor of lower number for $|q| = 0$. On the other hand, for negative interaction system, where $a < 0$ the system is in favor of large number for $|q| = \frac{N}{2}$. A general ground state of our simple two-mode model when both tunneling and interaction exist is somewhere in between of the two extreme cases we have described. As pointed out in [96], for $U > 0$, by minimizing the mean-energy of Hamiltonian, the ground state for "repulsive family" can be approximated by a single Gaussian-like distribution:

$$\Psi_q^+ = G_\sigma(q), \quad \frac{2}{\sigma^2} = \left(\frac{1}{N^2} + \frac{U}{tN}\right)^{1/2} \tag{4.11}$$

where the wavefunction is $G_\sigma(q) = e^{-l^2/2\sigma^2}/(\pi\sigma^2)^{1/4}$. The center of the distribution is around $q = 0$. When $U \gg t$, the spread σ approaches zero and the wave function

is close to delta function. This corresponds to the Fock state $|N/2, N/2\rangle$ as shown in Fig. 4.4(b). It is also know as fragmentation Ref. [98]. Note that this is a single state and there is no split in the Hilbert space. For $U < 0$, the ground states can be approximated by [96]:

$$\Psi_q^- = Q(\Psi_q^L + \Psi_q^R) \tag{4.12}$$

where Q is the normalization constant, $\Psi_q^R = G_\sigma(q - q_0)$ and $\Psi_q^R = \Psi_{-q}^L$. This is a superposition of two Gaussian distributions, each of which is coherent and Fock-like state $\Psi_q^- = Q(|L\rangle + |R\rangle)$:

$$|L\rangle = \sum_q G_\sigma(q)|\tilde{q}\rangle_{N_+,N_-} \quad |R\rangle = \sum_q G_\sigma(q)|\tilde{q}\rangle_{N_-,N_+} \tag{4.13}$$

where $|\tilde{q}\rangle_{N_+,N_-} = |N_+ + q, N_- - q\rangle$, $N_\pm = \frac{N}{2} \pm q_0$. We can obtain the minima center q_0 and the spread of the wave package σ by minimizing mean energy of the Hamiltonian. When $q_0 > \sigma$, the wave packet will split in Hilbert space and we will have a cat-like state that has superposition of two well-separated components as shown in Fig. 4.4(c).

4.3.2 Numerical analysis

We have had qualitative discussion about the dynamics with a simple spacial double well system. To quantitatively solve such a system so that the properties we discussed can be demonstrated, one way is to numerically solve the nonlinear Schrödinger equation in 3D or under some approximation [99]. Here we present a simple method by

(a)   (b)   (c)
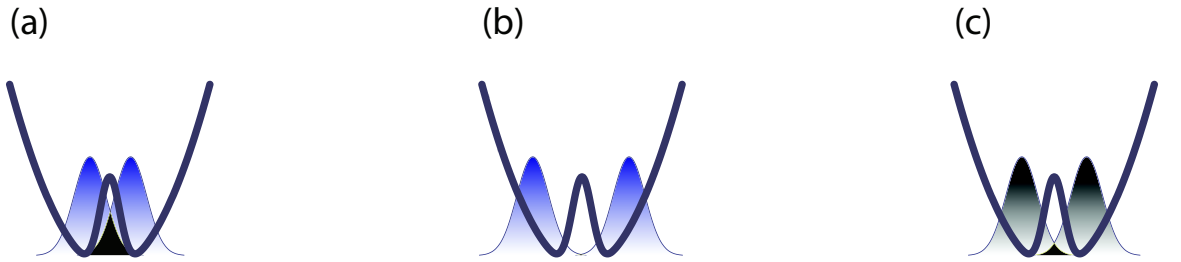
Figure 4.4: (a) Coherent state in single trap; (b) Fock state in double trap for $a > 0$; (c) Cat state in double trap for $a < 0$

diagonalizing the matrix of the Hamiltonian(4.10) in the Hilbert space. By doing that we can solve the wave function and calculate the necessary properties for the experiment. Although this is not an ultimately accurate solution, it presents simple and clear pictures for the problem.

The interaction term in(4.10) is density dependent, which means it is a function of the number of atoms in the trap. Although this doesn't effect the basic physics, we would like to have a numerical estimate before plugging the interaction coefficient into the Hamiltonian. To do this, we follow the recipe from Baym and Pethick [98], which gives a general calculation for ground state properties of interactive system.

Standard quantum mechanics tells us that when there is no interaction, the single particle wavefunction inside a cigar shaped harmonic trap can be written as:

$$\phi_0(\vec{\mathbf{r}}) = \frac{1}{\pi_{3/4}a_\perp a_z^{1/2}}e^{-m(\omega_\perp^0 r_\perp^2 + \omega_z^0 z^2)/2\hbar} \tag{4.14}$$

where $\omega_\perp^0$ and ω_z^0 are the trapping frequency in the radial direction and axial direction. The characterized length is defined as:

$$a_\perp = \sqrt{\frac{\hbar}{m\omega_\perp^0}} \quad a_z = \sqrt{\frac{\hbar}{m\omega_z^0}}$$

Due to the interaction, the wavefunction is modified. For the repulsive interaction, the atom cloud spread outs. This results in a reduced effective trapping frequency. For attractive interaction, to the opposite, we will have an increased effective trapping frequency. This is intuitively right. To quantitatively calculate the change of wavefunction due to the interaction, let's assume that the ground state is still approximately gaussian shape. By using trial function we can minimize the system energy so as to get the effective wavefunction and then get the chemical potential of the system.

In the Hartree approximation, the ground state energy is given by GPE [100]

function:

$$E(\psi) = \int d^3r \left[\frac{\hbar^2}{2m} |\nabla \psi(\vec{r})|^2 + \frac{m}{2}[(\omega_\perp^0)^2 r_\perp^2 + (\omega_z^2)^2 z^2] \times |\psi(\vec{r})|^2 + \frac{2\pi\hbar^2 a}{m} |\psi(\vec{r})|^4 \right]$$
(4.15)

Consider the ground state is in the form:

$$\psi(\vec{r}) = N^{1/2} \omega_\perp^{1/2} \omega_z^{1/4} \left(\frac{m}{\pi\hbar} \right)^{3/4} e^{-m(\omega_\perp r_\perp^2 + \omega_z z^2)/2\hbar}$$
(4.16)

where $\omega_\perp$ and ω_z are the parameters for the trial function. This trial waveform satisfies the integration requirement $\int d^3r |\psi(\vec{r})| = N$. If we plug wave equation (4.16) into equation (4.15), we will have the ground state energy as:

$$E(\omega_\perp, \omega_z) = N\hbar \left(\frac{\omega_\perp}{2} + \frac{(\omega_\perp^0)^2}{2\omega_\perp} + \frac{\omega_z}{4} + \frac{(\omega_z^0)^2}{4\omega_z} + \frac{Nam^{1/2}(2\pi\hbar)^{1/2}}{\omega}_\perp \omega_z^{1/2} \right)$$
(4.17)

Note that the equation (4.17) is a function of both $\omega_\perp$ and ω_z. Let's suppose $k_0 = \frac{Na\sqrt{n}}{\sqrt{2\pi m}}$. If we take differentiation of E with respect $\omega_\perp$ and set it equal to zero, we will have:

$$E'(\omega_\perp, \omega_z) = \frac{1}{2} - \frac{(\omega_\perp^0)^{1/2}}{2\omega_\perp^2} + k_0 \omega_z^{1/2} = 0$$

Define a new parameter as:

$$\triangle = \left(1 + 2k_0 \omega_z^{1/2} \right)$$
(4.18)

After solving the simple equation above with the newly defined parameter, we will have the simplified form for the radial frequency:

$$\omega_\perp = \frac{\omega_\perp^0}{\triangle}$$

With this new parameter for the trial function, the ground state energy (4.17) ends up as:

$$E(\omega_z) = N\hbar \left[\omega_\perp^0 \triangle + \frac{\omega_z}{4} + \frac{(\omega_z^0)}{4\omega_z} \right]$$
(4.19)

Equation (4.19) is one of the key results. After a long way, we minimized the ground state energy to appear to be only axial frequency dependent($\triangle$ is a function

of ω_z). In the same spirit, we can continue to minimize the energy by finding out the effective axial frequency and ground state energy for different numbers of atoms in the system. This can be easily done with Matlab. Fig. 4.5 shows the numerical results.
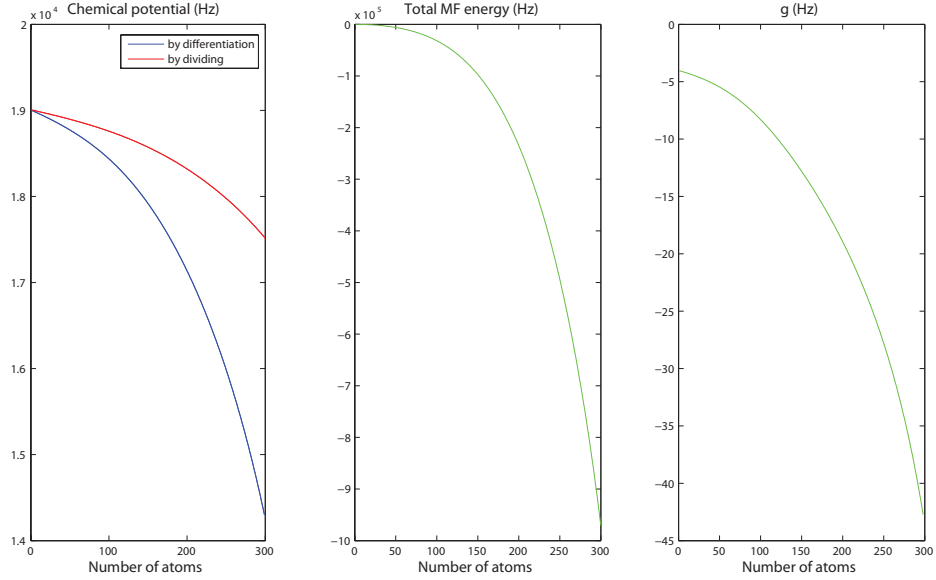
Figure 4.5: From left to right, chemical potential per particle; mean field interaction energy; Bose-Hubbard model g coefficient.

The left plot demonstrates the change of chemical potential energy with respect to the change of the number of atoms in the trap. The chemical potential energy as been defined as $\mu = \frac{dE}{dN}$ and $\mu = \frac{E}{N}$ respectively. We can see that the two definitions give close but different results. The middle plot corresponds to the total mean field energy for different number of atoms. We can see the mean field energy drops as more atoms are added due to the negative interaction. The right plot gives the relation between $g = \frac{d^2E}{dN^2}$ and atom number. This g has the same meaning as in equation (4.5) and (4.10). A polynomial fit is used to extract the relation between interaction coefficient g and number of atoms N. This fitted curve is the key result for this session and is used for the future calculation.

Before we move to calculate the Hamiltonian, we need to notice that there is an
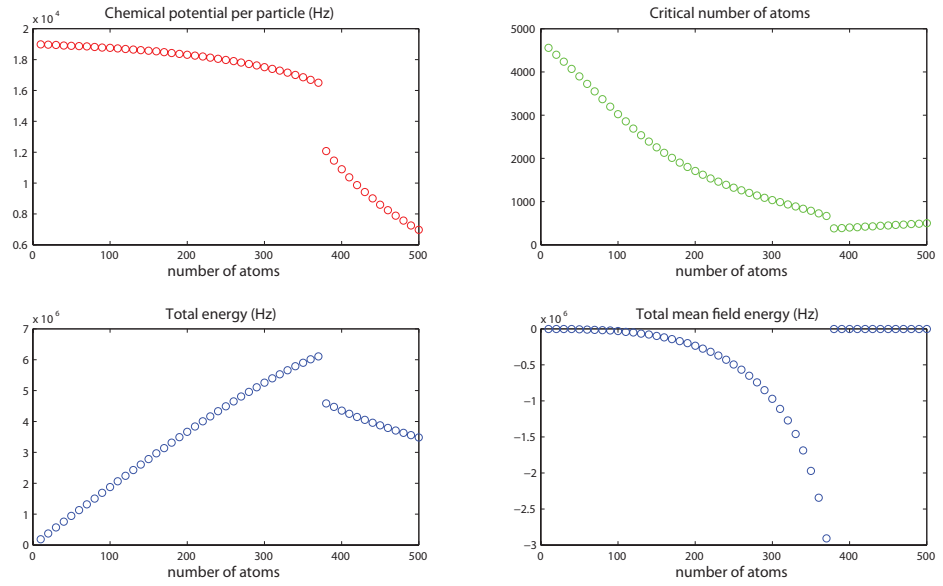
Figure 4.6: Upleft, chemical potential per particle $\mu = \frac{E}{N}$; Upright, upper limit of number of atoms can be hold when there are N atoms in the trap; Downleft, total system energy wrt number of atoms in the trap; Downright, total mean field energy wrt number of atoms in the trap

upper limit for the number of atoms so as to keep equation (4.18) valid. Here we get another way for the calculation of the critical point for our attractive system. Plug in the definition of k_0, we will have:

$$\triangle^2 = 1 - \sqrt{\frac{2}{\pi}} \frac{N|a|}{a_\perp} \sqrt{\frac{\omega_z}{\omega_\perp^0}}$$

Apparently to have valid value for $\triangle$ we need to have

$$N \le \sqrt{\frac{\pi}{2}} \frac{a_\perp}{|a|} \sqrt{\frac{\omega_\perp^0}{\omega_z}}$$

where ω_z can be obtained by minimizing the ground state energy for the number of atom in the trap as before. From Fig. 4.6, we can see that there is a phase jump at number of atoms around 375 when the critical number of atoms equals the number of atoms inside the trap. This is the upper limit of the number of atoms that we can hold in the trap before collapse. So our fitting curve for the interaction coefficient is valid for less then 375 atoms in the trap.

After armed with the estimation of interaction strength, we can solve the wavefunction in the Hilbert space by diagonalizing the system Hamiltonian.

By using the $|q\rangle$ representation in the Hilbert space with equation (4.6), we have seen a clear Gaussian distribution in the Hilbert space which characterizes the basic physics for different interactions, equation (4.11,4.12). To do the numerical analysis, we use the same representation but with a minor change.

Consider the two-mode system as in the $|q\rangle$ representation, $|q\rangle = |n_L, n_R\rangle = |n, N - n\rangle$. Where n denotes n atoms in the left mode with $n \subset [0, N]$ and $N - n$ denotes that N-n atoms in the right. As before, for any wavefunction we can expand it in this basis as in equation (4.8). We then have:

$$|\Psi\rangle = \sum_q \Psi_q |q\rangle = \sum_q \Psi_q |n_L, n_R\rangle = \sum_q \Psi_q |n, N - n\rangle \qquad (4.20)$$

Apply the Hamiltonian (4.5) to the wavefunction (4.20), with the help of equation

(4.9), we will arrive at:

$$\frac{E\Psi_q}{\hbar} = -\gamma(t_{n-1}|n-1, N-n+1\rangle + t_n|n+1, N-n-1\rangle + \frac{g}{2}(n^2 + (N-n)^2)|n, N-n\rangle$$

(4.21)

where $t_n = \sqrt{(n+1)(N-n)}$. The Hamiltonian matrix in this representation looks like:

$$\mathbf{H} = \begin{pmatrix} \frac{g}{2}(0^2 + N^2) & \gamma\sqrt{1*N} & 0 & 0 & 0 & \dots \\ \gamma\sqrt{1*N} & \frac{g}{2}(1^2 + (N-1)^2) & \gamma\sqrt{2*(N-1)} & 0 & 0 & \dots \\ 0 & \gamma\sqrt{2*(N-1)} & \frac{g}{2}(2^2 + (N-2)^2) & \gamma\sqrt{3*(N-2)} & 0 & \dots \\ \vdots & \vdots & \vdots & \vdots & \vdots & \ddots \end{pmatrix}$$

We can set up the Hamiltonian matrix using Matlab with $g = g(N)$ that we have gotten from previous curve fitting. After diagonalizing the matrix, we can get the eigenvalue and eigenstate in the Hilbert space. The lowest energy state is the ground state we look for. One thing needs to be noticed is that when there is degeneracy the ground state should be the symmetric superposition of the first two states so it is important to detect degeneracy in the calculation code. A typical system evolution is shown in Fig. 4.7. The number of atoms we used is $N = 100$. The system evolves when we change the tunneling frequency γ. We can see in the figure that with the increase of tunneling frequency, the system proceeds from pure cat state to deep cat state, quasi-cat state and then coherent state. This checks with our qualitative discussion before. With the probability distribution which is calculated by the square of ground state wavefunction, we can calculate the number variance for that specific state. For a coherent state, the number variance is in the order of $N/4$ and the number standard deviation is in the order of $N/\sqrt{2}$. For a cat-like state the number variance is in the order of $N^2/4$ and the number standard deviation is in the order of $N/2$. The large value of variance is one of the signature for a cat state.

A complete scan of the number variance and energy gap between the first two states versus tunneling frequency is shown in the Fig. 4.8. We can clearly see on the figure that when the tunneling frequency is relatively high, the energy gap is quite obvious and the number variance is low. With tunneling frequency decreases, the
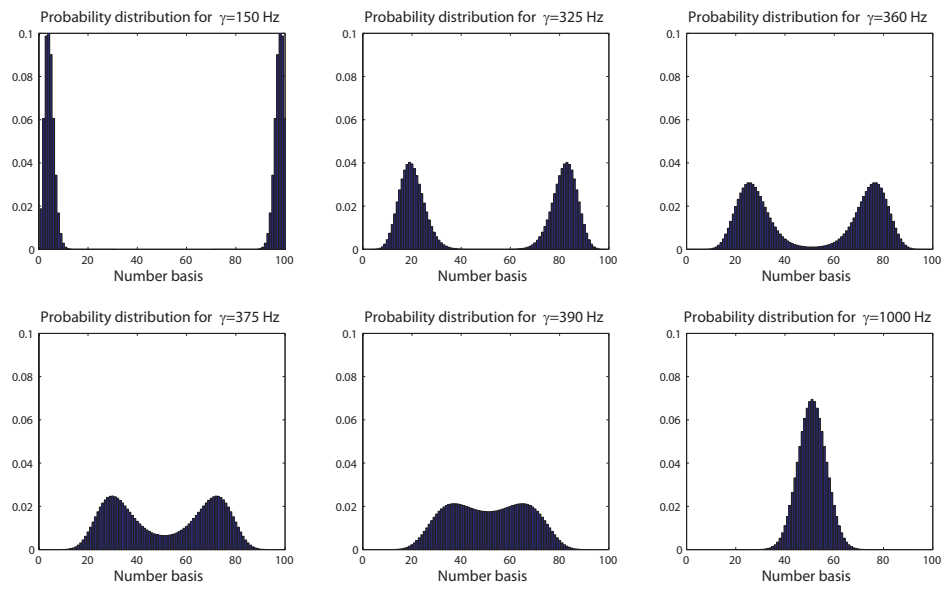
Figure 4.7: System evolves with increase of tunneling frequency from left to right and up to down

energy degeneracy kicks in and we see an increase of number variance where we get into a cat-like state. The same picture is also shown on the figure for those changes versus Ng/γ, which is a close to the unity value. Note that the spike on the curve for number variance is due to the cut-off computation error.
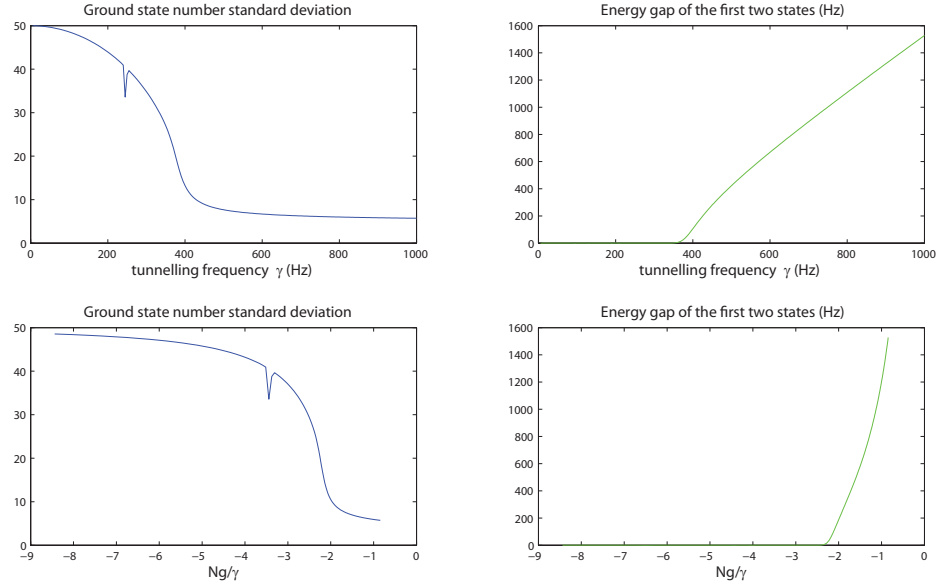
Figure 4.8: Number standard deviation and energy gap versus change of tunneling frequency and NU/γ

Similar results have been obtained by the authors in [86, 96, 92]. Different from our two-mode method, an approach with numerical calculation for GPE that is solely for ^{7}Li in the spatial double well can be found at [101]. In that paper, GPE is solved on a discrete space lattice and lowest energy is evaluated. After that a two-mode approximation is chosen to reproduce the stable numerical solution. It also demonstrates the feasibility of the macroscopic quantum coherence.

4.3.3 Something about adiabatic process

As pointed out in [97], It can be quite hard to adiabatically tweak the collision cross section from positive to negative to ramp the system into a cat state [86] because

the cat state appears when energy degeneracy happens. When the energy difference between teh symmetric state and asymmetric state is close, any small perturbation will mix the two states. In this sense, a quasi-cat will be more stable and easy to achieve than a pure cat state.

In the paper [85], the author proposes to adiabatically imprint a π phase shift across the barrier to ramp the system into a cat state. According to similar argument as above, since the energy difference is quite small, the phase shift could result in a random superposition of the two states, which will lose the coherence and act as a collapsed cat state.

In a word, adiabatic creation of pure cat state could require exponentially long time, which is experimentally not possible, so we need to stay in the regime for a quasi-cat.

4.3.4   Detection: catch the cat

We have seen in the cavity experiment that decoherence will happen when we try to get state information. This means that detection could also introduce decoherence if we extract much information through the "observation". It could be quite challenging to do a non-demolishing measurement on our system, for instance, using a far detuned laser light to do the phase contrast imaging. In stead, what we are currently doing is to destructively measure each identically prepared system and see the statistically results. This means that we create a cat state and then open the box to measure the cat. For each measurement, apparently we should have statistically results of the distribution. When we have such results, it is the required condition in stead of necessary condition to claim a cat state but it is a good signature to start with.

Beside the detection-induced decoherence, the environment-induced decoherence can also put a macroscopically superposition states into the classical mixture. It is a challenge to the experimentalist to distinguish these two kinds of situations which, as we discussed in the beginning of this chapter, will generate the same statistical results for a destructive detection. Experimentally it is also important to determine the characteristic time for decoherence for a cat state before it loses coherence to be

a statistical mixture. This time scale is important for the potential application to use cat state as precision measurement and quantum information process.

Here we will discuss three ways to differentiate a quantum cat state from the classical probability mixture in experiment, coherent mode oscillation, interference pattern and phase revival.

Coherent oscillation between two modes can be a key signature for cat states. Consider a prepared cat ground state. Measurement will collapse the atom cloud onto one peak of two possible states with energy minima. If the energy transfer during the measurement is not too large so that we only populate the first excited state we then have the superposition of ψ_0 and ψ_1, which is symmetric and antisymmetric respectively with energy difference $\hbar\omega_f$. We have assumed a proper phase so that ψ_0 and ψ_1 are real functions. At time zero immediately after measurement, the new state $\psi_0 + \psi_1$ has only one probability peak. After $t = \frac{\pi}{2\omega_f}$, the state becomes $\psi_0 - i\psi_1$, which has two probability peaks. After $t = \frac{\pi}{\omega_f}$ we will have a probability peak on the other side and so on. Observing such a coherent oscillation will be a strong evidence for the creation of cat state. This requires continuous measurement which will not disturb the system evolvement. Phase contract imaging can be a good candidate for this although technically it is quite challenging. If we could control the initial phase well [102, 20] so as to have a well defined initial state, a destructive imaging can also work. For different holding time, we will expect spatially always right, half left half right and always right for the distribution for every experimental shot. Since the detection depends on spatially differentiating two modes, good spatial resolution is needed. Another thing needs to consider is that to experimentally observe such an oscillation the oscillation frequency cannot be two low since a too long holding time will make the observation impossible. This indicates that for the initial state we need to stay in the quasi-cat state regime.

As pointed out by the author of [101], coherence is quite robust against atom loss for a quasi-cat. For instance, when $\omega \sim 25Hz$, for a typical system, the number loss can be ignored for decoherence.

The phase coherence of BEC atoms are well proved and the interferometry for BEC atoms is also observed [14, 83, 20, 18, 103]. So it is naturally a good consideration to

use interferometry to verify cat state. Can we do it?

Due to the projective nature of measurement process that will collapse a coherent state into a Fock state, as pointed out by a few authors [104, 105], coherent state and Fock state cannot be distinguished by measuring the interference profile for two overlapping condensate which are separated initially. As pointed out in [96], those authors didn't derive the spatial pattern for interference.

Consider a series of D detectors that are located at x_i. The joint probability to detect k particles with k_i and location x_i and $\sum_{i=1}^{D} k_i = k$ is [96]:

$$P(k_i) = \frac{(N-k)!}{N!} \frac{k!}{\prod_{i=1}^{D} k_i!} ||\hat{O}|\Psi\rangle_N||^2 \tag{4.22}$$

where $\hat{O} = \prod_i \hat{\psi}^{k_i}(x_i)$ is the operator to remove k_i particles at location x_i. The measured density profile at x_i is the one with most probability set $\bar{k}_i$ to optimize $P(k_i)$. For a cat state like equation (4.12) we will have:

$$P(k_i) = Q^2 \left[P_L(k_i) + P_R(k_i) + P_{LR}(k_i) \right]$$

where $P_{(L,R)} \sim \langle (L,R)|\hat{O}^\dagger \hat{O}|(L,R)\rangle$ and $P_{LR} \sim \langle L|\hat{O}^\dagger \hat{O}|R\rangle + c.c.$ As we discussed before, cat state appears when $q_0 > \sigma$. In such a situation the cross term can be ignored since it depends on the overlap of $|L\rangle$ and $|R\rangle$, which is small. The resulted interference pattern is proportional to $\bar{k}_j^{\,L} + \bar{k}_j^{\,R}$.

Consider a coherent state:

$$|\alpha, \beta\rangle_N = \frac{1}{\sqrt{N!}} \left(\mu c_L^\dagger + \nu c_R^\dagger \right)^N |0\rangle \tag{4.23}$$

where $\mu = e^{-i\alpha/2} cos\frac{\beta}{2}, \nu = e^{i\alpha/2} sin\frac{\beta}{2}, cos^2\frac{\beta}{2} = \frac{N_+}{N}, N_\pm = N/2 \pm q_0$. The author of [96] shows that the measurement will project the state $|L\rangle$ to a coherent state $|\alpha^*, \beta\rangle$. As the state becomes more cat like, we will have the most probable set:

$$\bar{k}_i^{\,L} = \bar{k}_i^{\,R} = \lambda \left[1 + sin\beta cos \left(\frac{2Mx_0 x}{\hbar t} - \alpha^* \right) \right] \tag{4.24}$$

where λ is a constant and M, x_0, t are defined in a non-interacting particles expansion. For expansion time $t > 0$, $\hat{\psi}(x,t) = \sqrt{\frac{m}{i2\pi\hbar t}} \int ds e^{iM(x-s)^2/2\hbar t} \hat{\psi}(s)$, where $\psi(s) \approx \gamma \left(e^{i\zeta(x)/2} c_L + e^{-i\zeta(x)/2} c_R \right)$, $\zeta(x) = (2x_0 M/\hbar t)x$ and $\gamma = \sqrt{\frac{m}{i2\pi\hbar t}} e^{iM(x^2+x_0^2)/2\hbar t}$. c_L and c_R are Wannier states localized at $\pm x_0$.

Notice that the interference fringe has a sinusoidal oscillation with spatial frequency $\frac{\hbar t}{2Mx_0}$. When the system is deeper in cat state with higher barrier in double-well system, $N_+ \sim N$ so $cos^2\frac{\beta}{2} = \frac{N_+}{N} \sim 0$. The amplitude of the oscillation $sin\beta$ will decrease as the system is more in cat like state. This is different from a positive system where the contrast of interference fringe will not depend on the barrier height.

Number squeezing will randomize the phase for fragmented Fock state in lattice [14]. As pointed out by the author in [106, 103], number squeezing can also help increase the coherence time by reducing uncertainty of interaction energy in each well so as to reduce phase diffusion [107]. For a negative interaction system, squeezing corresponding to a deep cat state. Whether the interference fringe changes as the theory predicts when we drive the system into such a regime is an open question and it is important for us to understand the many body interaction and phase coherence.

We have discussed coherent oscillation and interference to detect cat state. Now let's talk about phase revival process.

We have discussed that it is quite hard to adiabatically cool the system down to cat state where cat state is the ground state of the Hamiltonian. A few authors have discussed dynamic evolution to generate cat state. As pointed out in the paper [87], for a double component BEC in a trap, the interplay between Josephson coupling and collisional effect will drive the system from a coherent state into a cat state under unitary evolution. Under proper parameters, there will be an oscillation between coherent state and cat state. In the paper [97], the authors have pointed out a way to create a cat state with sudden change of the sign of scattering length from positive to negative by Feshbach resonance [56] in a spatially double well. They have theoretically demonstrated a periodic creation of cat state.

As we have discussed before, the dynamics of our system is the balance between tunneling and interaction. This is very similar to the discussion in [87, 97]. After we created BEC for a single well, when we raise up the barrier adiabatically, the coherent

state is not the ground state any more and it will then start a dynamic evolution under the new Hamiltonian. When we are not in a deep cat state and the tunneling is kept strong enough, the system will have a phase revival oscillation between cat state and coherent state as in [97]. To create the cat state, we need to increase the barrier height and freeze out the evolution when the system is at the cat state point. For the purpose of destructive detection, different from the coherent oscillation, we shall see single peak in the center of the trap at time zero for coherent state, probabilistic distribution at time of $t = \frac{\tau}{2}$, where τ is oscillation period, and single peak at $t = \tau$. The ramping speed and height of barrier are critical and needed to be scanned in the experiment.

4.4 Experimental Results

4.4.1 Setup and procedure

A double well provides platform for theoretical model testing due to its simple geographic set-up. There are quite a few ways that people use to set up a double well. For instance use a blue-detuned dimple light [12], different laser frequency through AOM [83] or Radio frequency induced an adiabatic double well [18, 103]. In our system, due to the accessibility concern, we upgrade our single trap system to a double well by shining a single blue-detuned laser light through the magnetic trap to divide the trap into two. The amplitude of the dimple light is controlled by a feedback circuit and the position is controlled by ultra stable kinetic mirror mount. The first experiment to observe BEC interference [12] used similar approach. According to [83], that experiment suffers from variation and fluctuation of the laser beam which introduce random phase noise for the interference. We had paid a lot attention, as discussed in previous chapter, to stabilize the dimple beam.

The procedure for the cat experiment has been shown in the Fig. 4.9. $|2, -2\rangle$ atoms are loaded into the mini-trap. After the transfer, 35 seconds standard evaporation is applied as before to achieve quantum degeneracy. At the end of evaporation, dimple beam is adiabatically ramped. The ramping and amplitude of the peak are

controlled by a feedback circuit and the wave form is modulated by an arbitrary wave-form generator. Variable holding time can be applied. $20\mu s$ on resonance absorption probing takes place after variable time of flight(TOF).

As we have discussed, the fragility of the cat state makes the creation and detection a huge challenge. Demonstration of a cat state is hard because we are working with a small number of atoms,~ 100. At the same time, as we mentioned in the imaging technique section, due to the property of Lithium, no close transition makes it very hard to get good signal noise ratio. We spent a lot of time to optimize the imaging system and reduce the noise.

4.4.2   Observation and interpretation

In the theoretical discussion, we mentioned that the speed of ramping and the amplitude of the barrier will influence the final result. Before we spent time to search for such an optimized parameters, with destructive imaging, we should see statistical behavior for rather high barriers when we ramp close to cat state. This is like to open the dark box to observe the status of the cat. Sometimes the cat is dead and sometimes it is alive.

In the experiment, the RF was ramped down to about $30kHz$ to the trap bottom. At this time, there are about 100 atoms in the trap with temperature of about $20nK$.
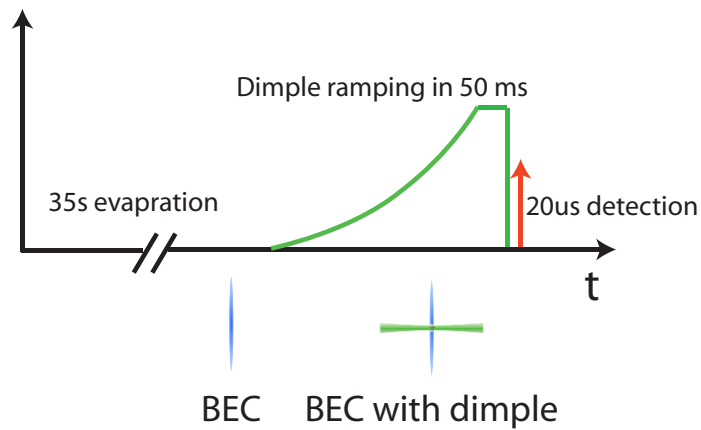

Figure 4.9: Schematic of experimental sequence

The barrier height was set at $5kHz$, which corresponds to about $500nK$. We did see statistical behaviors for each shot. Fig. 4.10 shows two typical shots. One shows that the atom cloud concentrates on the left and the other shows that the concentration is on the right of the barrier. The blue bars show the relative positions of the dimple light with respect to the atom cloud. In that figure I have also included intersection in the radial direction of the cloud, which is used to show a good signal noise ratio. (Here we should also include on this figure for false color atom cloud distribution)
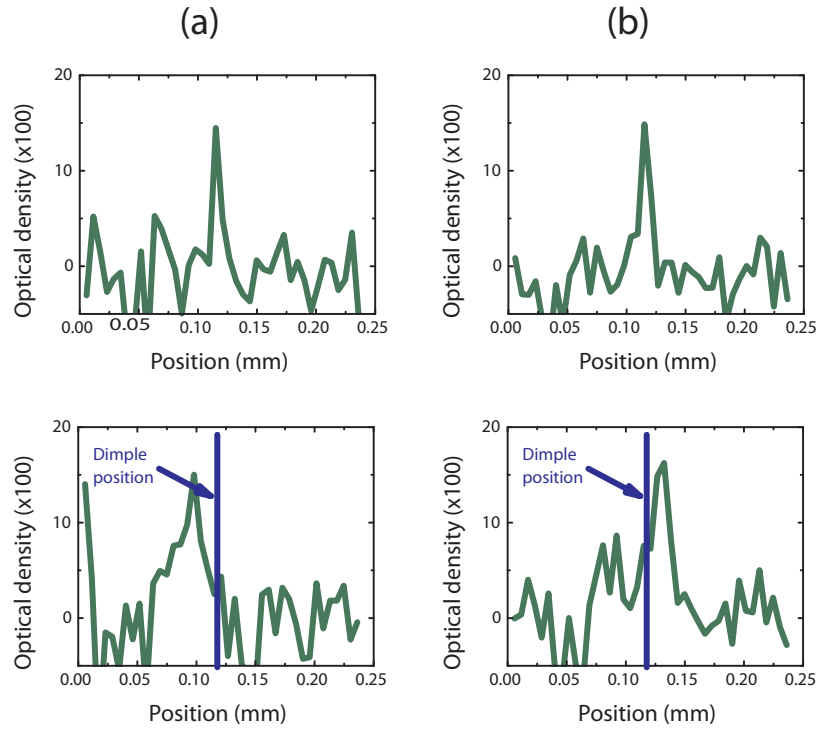
Figure 4.10: Two typical shots with statistical behaviors. Top row is the intersection in radial direction and the lower row is the intersection in axial direction. (a) peak at the left of the dimple barrier; (b) peak at the right of the dimple barrier

A statistical result for one fixed barrier position is shown in Fig. 4.11, where the x axis represents the unevenness of number distribution $\frac{N_L - N_R}{N_L + N_R}$. N_L is the number of atoms on the left of the barrier and similar for N_R. The y axis shows number of shots that have those unevenness. From this figure we can see that at such a barrier

position we have seen a statistical mixture, which means sometimes we got most of the atoms on the left and sometimes we got them on the right.

Figure 4.11: Statistical results for a fixed barrier position

To demonstrate taht the statistical behavior is a quantum behavior, we adjusted the barrier position relative to the cloud. At each such position we t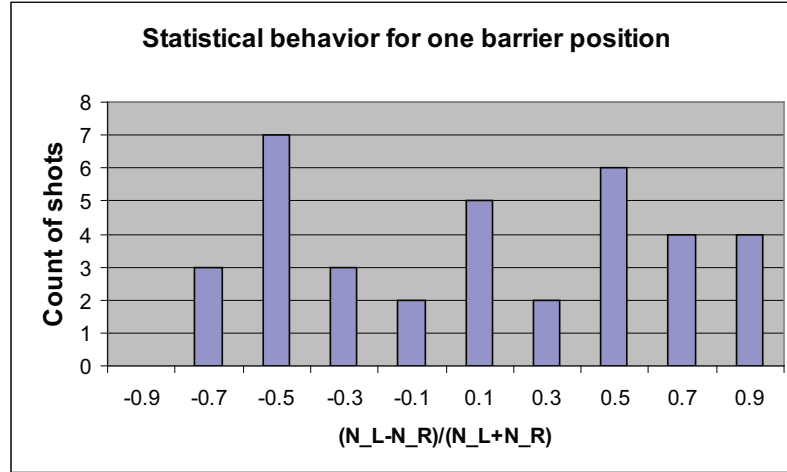ook a bunch of shots and got statistics like Fig. 4.11. The calculated number variance in one of the well for this measurement is $\langle(\Delta N_1)^2\rangle = 800$. For 100 atoms, this is much closer to the variance for a cat state, $N^2/4 = 2500$ than to the variance of a coherent state, $N/4 = 25$.

In Fig. 4.12 we show the relation between the statistics and different barrier positions. A blue bar is used to indicate the position of the barrier relative to the gaussian shape of the atom cloud. As we can see on this figure, when the center of the cloud is on the left/right of the barrier before we raise up the barrier, most of the atoms will stay on the left/right due to self trapping. When the barrier position is close to the center, the appearance is quite random. For a positive interaction system or even a thermal system, when such a high barrier raise up, we would expect fragmentation on both side of the barrier which means the distribution is still centered around zero. What we have seen indicates that the quantum behavior changed physics.

As we have seen that in the experiment we saw random peaks on the left and

right of the dimple barrier. To firmly proof that this is the unique phenomenon for the negative interaction system, we would like to run the same sequence for a positive interaction state, $|1, -1\rangle$ for ^7Li. For such a state we would expect stable double peaks when the dimple barrier is present.

To observe the quantum behavior for $|1, -1\rangle$ state, we need to create BEC for such a state. Although the scattering length for this state is positive, which means we can have a stable BEC, its amplitude is very small. $a_s(|1, -1\rangle) = 5.1a_0 = 0.27nm$, where a_0 is Bohr radius. This is about 400 times smaller than ^{87}Rb. We would need extremely long direct evaporation time to achieve BEC for such a state. For instance, if you can achieve BEC in $5s$ for ^{87}Rb, you would need at least $2000s$ for ^7Li in such a state. This is experimentally impossible. So there is hardly any way to achieve BEC with direct evaporation.

Two other groups who have realized BEC on $|1, -1\rangle$ for ^7Li employ combined techniques. Salomon's group used Fermion to sympathetically cools the boson [108] and Hulet's group used Feshbach resonance to tweak the scattering length [21]. Since we have a better starting point with high phase space density and number of atoms, we would like to adopt a new way by pumping atoms adiabatically from $|2, 2\rangle$ state to $|1, -1\rangle$ state. This should be done when most of the evaporation has finished and
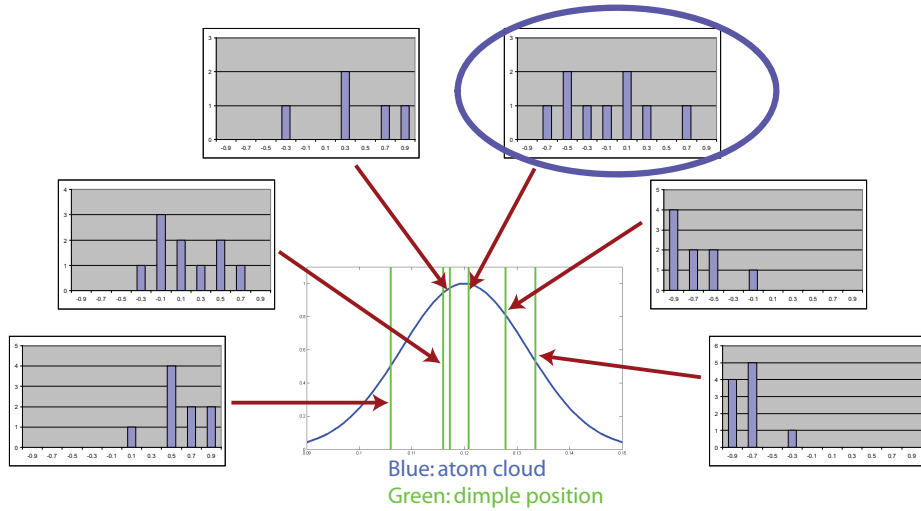

Figure 4.12: Statistics at different barrier position

the atom cloud is in high phase space density(PSD). When the transfer is done well and close to adiabatic [43], we wouldn't loose much PSD and thus it is not far from quantum degeneracy. Then a not too long evaporation for $|1, -1\rangle$ would suffice to achieve BEC.

While I am working on the thesis, the team is still pursuing a good demonstration of cat state by first achieving a stable BEC state on $|1, -1\rangle$. The adiabatic transfer has been demonstrated and parameters are being optimized.

To completely verify that we have a cat state, further experiments should be carried out, as we have discussed, to observe either coherent oscillation, interference pattern or phase revival. Due to the time constraint of this study, these tasks are left for the near future.

As we have discussed before, coupling the internal freedom with external modes can also help the creation of cat state. [87, 88, 89]. It would be interesting to have a positive and negative components coupled together, which has not been theoretically discussed by anyone. This is one of the open questions that can be potentially tested with our apparatus.

Bibliography

[1] S. N. Bose. *Z. Phys.*, 26, 1924.

[2] M. H. Anderson and *et al.*. Observation of bose-einstein condensation in a dilute atomic vapor. *Science*, 269:198–201, July 1995.

[3] C. C. Bradley, C. A. Sackett, and R. G. Hulet. Bose-einstein condensation of lithium: Observation of limited condensate number. *Phys. Rev. Lett.*, 78(6):985–989, Feb 1997.

[4] K. B. Davis and *et al.*. Bose-einstein condensation in a gas of sodium atoms. *Phys. Rev. Lett.*, 75(22):3969–3973, Nov 1995.

[5] F. London. On the bose-einstein condensation. *Phys. Rev.*, 54(11):947–954, Dec 1938.

[6] Willian C. Stwalley and L. H. Nosanow. Possible "new" quantum systems. *Phys. Rev. Lett.*, 36(15):910–913, Apr 1976.

[7] Dale G. Fried and *et al.*. Bose-einstein condensation of atomic hydrogen. *Phys. Rev. Lett.*, 81(18):3811–3814, Nov 1998.

[8] Steven Chu. Nobel lecture: The manipulation of neutral particles. *Rev. Mod. Phys.*, 70(3):685–706, Jul 1998.

[9] Franco Dalfovo, Stefano Giorgini, Lev P. Pitaevskii, and Sandro Stringari. Theory of bose-einstein condensation in trapped gases. *Rev. Mod. Phys.*, 71(3):463–512, Apr 1999.

[10] Anthony J. Leggett. Bose-einstein condensation in the alkali gases: Some fundamental concepts. *Rev. Mod. Phys.*, 73(2):307–356, Apr 2001.

[11] Mark A. Kasevich. Coherence with atoms. *Science*, 298(5597):1363 – 1368, Nov 2002.

[12] M. R. Andrews and *et al.*. Observation of interference between two bose condensates. *Science*, 275:637, Jan 1997.

[13] B. P. Anderson and M. A. Kasevich. Macroscopic quantum interference from atomic tunnel arrays, 1998.

[14] C. Orzel and *et al.*. Squeezed states in a bose-einstein condensate. *Science*, 291:2386, Mar 2001.

[15] Markus Greiner and *et al.*. Quantum phase transition from a superfluid to a mott insulator in a gas of ultracold atoms, 2002.

[16] Markus Greiner and *et al.*. Collapse and revival of the matter wave field of a bose-einstein condensate., 2002.

[17] S. Jochim and *et al.*. Collapse and revival of the matter wave field of a bose-einstein condensate., 2003.

[18] T. SCHUMM and *et al.*. Matter-wave interferometry in a double well on an atom chip. *Nature(London)*, 1:57, Sep 2005.

[19] G.-B. Jo and *et al.*. Long phase coherence time and number squeezing of two bose-einstein condensates on an atom chip. *Physical Review Letters*, 98(3):030407, 2007.

[20] Michael Albiez and *et al.*. Direct observation of tunneling and nonlinear self-trapping in a single bosonic josephson junction. *Physical Review Letters*, 95(1):010402, 2005.

[21] Kevin E. Strecker and *et al.*. Formation and propagation of matter-wave soliton trains. *Nature(London)*, 417:150–153, May 2002.

[22] S. Tung, V. Schweikhard, and E. A. Cornell. Observation of vortex pinning in bose-einstein condensates. *Physical Review Letters*, 97(24):240402, 2006.

[23] Martin W. Zwierlein and *et al.*. Direct observation of the superfluid phase transition in ultracold fermi gases, 2006.

[24] GT; McGuirk JM; Kasevich MA Fixler, JB; Foster. Atom interferometer measurement of the newtonian constant of gravity, 2007.

[25] K. Huang. *Statistical Mechanics, 2nd*. John Wiley & Sons, New York, 1987.

[26] C. J. Pethick and H. Smith. *Bose Einstein Condensation in Dilute Gases*. Cam-bridge University Press, Cambridge, 2002.

[27] E. P. Gross, 1961.

[28] L. P. Pitaevskii, 1961.

[29] P. A. Ruprecht, M. J. Holland, K. Burnett, and Mark Edwards. Time-dependent solution of the nonlinear schrödinger equation for bose-condensed trapped neutral atoms. *Phys. Rev. A*, 51(6):4704–4711, Jun 1995.

[30] Hans A. Bethe and Edvin E. Salpeter. *Quantum Mechanics of One- and Two-Electron Atoms*. Springer-Verlag, Berlin, 1957.

[31] J. P. Gordon and A. Ashkin. Motion of atoms in a radiation trap. *Phys. Rev. A*, 21(5):1606–1617, May 1980.

[32] D. J. Wineland and Wayne M. Itano. Laser cooling of atoms. *Phys. Rev. A*, 20(4):1521–1540, Oct 1979.

[33] Paul D. Lett and *et al.*. Observation of atoms laser cooled below the doppler limit. *Phys. Rev. Lett.*, 61(2):169–172, Jul 1988.

[34] C. Cohen-Tannoudji and W. Phillips. New mechanisms for laser cooling. *Physics Today*, 43(33), Oct 1990.

[35] E. L. Raab, M. Prentiss, Alex Cable, Steven Chu, and D. E. Pritchard. Trapping of neutral sodium atoms with radiation pressure. *Phys. Rev. Lett.*, 59(23):2631–2634, Dec 1987.

[36] Steven Chu, J. E. Bjorkholm, A. Ashkin, and A. Cable. Experimental observation of optically trapped atoms. *Phys. Rev. Lett.*, 57(3):314–317, Jul 1986.

[37] Rudolf Grimm, Matthias Weidemuller, and Yurii B. Ovchinnikov. Optical dipole traps for neutral atoms. *MOLECULAR AND OPTICAL PHYSICS*, 42:95, 2000.

[38] E. L. Raab and *et al.*. Trapping of neutral sodium atoms with radiation pressure. *Phys. Rev. Lett.*, 59(23):2631–2634, Dec 1987.

[39] Harold J. Metcalf and Peter van der Straten. *Laser Cooling and Trapping.*

[40] J. J. Sakurai. *Modern Quantum Mechanics (2nd Edition).* 1994.

[41] C. R. Monroe and *et al.*. Measurement of cs-cs elastic scattering at t=30 μk. *Phys. Rev. Lett.*, 70(4):414–417, Jan 1993.

[42] Wolfgang Ketterle and N.J. Van Druten. Evaportive cooling of trapped atoms. *Advances in atomic, molecular, and optical physics*, 37, 1996.

[43] Florian Schreck. *Mixtures of ultracold gases: Fermi see and Bose-Einstein Condensate of Lithium isotopes.* PhD thesis, 2002.

[44] E. R. I. Abraham and *et al.*. Triplet s-wave resonance in ^6li collisions and scattering lengths of ^6li and ^7li. *Phys. Rev. A*, 55(5):R3299–R3302, May 1997.

[45] Fabio Mibielli Peixoto. *Enhanced Loading of a Lithium 7 Magneto Optical Trap using Transverse Cooling and Frequency Spread Light.* PhD thesis, 2002.

[46] Ruquan Wang. *Approaching Lithium BEC with a Mini Trap.* PhD thesis, 2006.

[47] Wolfgang Petrich and *et al.*. Stable, tightly confining magnetic trap for evaporative cooling of neutral atoms. *Phys. Rev. Lett.*, 74(17):3352–3355, Apr 1995.

[48] T. Bergeman and *et al.*. Magnetostatic trapping fields for neutral atoms. *Phys. Rev. A*, 35(4):1535–1546, Feb 1987.

[49] M.-O. Mewes and *et al.*. Bose-einstein condensation in a tightly confining dc magnetic trap. *Phys. Rev. Lett.*, 77(3):416–419, Jul 1996.

[50] W. Hänsel and *et al.*. Boseeinstein condensation on a microelectronic chip. *Nature(London)*, 413:498–501, October 2001.

[51] S. Friebel, C. D'Andrea, J. Walz, M. Weitz, and T. W. Hänsch. co_2-laser optical lattice with cold rubidium atoms. *Phys. Rev. A*, 57(1):R20–R23, Jan 1998.

[52] Vladan Vuletić and *et al.*. Degenerate raman sideband cooling of trapped cesium atoms at very high atomic densities. *Phys. Rev. Lett.*, 81(26):5768–5771, Dec 1998.

[53] E. I Butikov. Parametric excitation of a linear oscillator. *Eur. J. Phys.*, 25:535, 2004.

[54] C. C. Bradley, C. A. Sackett, and R. G. Hulet. Bose-einstein condensation of lithium: Observation of limited condensate number. *Phys. Rev. Lett.*, 78(6):985–989, Feb 1997.

[55] Kevin E. Strecker and *et al.*. Formation and propagation of matter-wave soliton trains. *Nature(London)*, 408:692–695, Dec. 2000.

[56] S. J. J. M. F. Kokkelmans and *et al.*. Resonance superfluidity: Renormalization of resonance scattering theory. *Phys. Rev. A*, 65(5):053617, May 2002.

[57] F. Schreck, L. Khaykovich, K. L. Corwin, G. Ferrari, T. Bourdel, J. Cubizolles, and C. Salomon. Quasipure bose-einstein condensate immersed in a fermi sea. *Phys. Rev. Lett.*, 87(8):080403, Aug 2001.

[58] F. Schreck, G. Ferrari, K. L. Corwin, J. Cubizolles, L. Khaykovich, M.-O. Mewes, and C. Salomon. Sympathetic cooling of bosonic and fermionic lithium gases towards quantum degeneracy. *Phys. Rev. A*, 64(1):011402, Jun 2001.

[59] J. M. Gerton, C. A. Sackett, B. J. Frew, and R. G. Hulet. Dipolar relaxation collisions in magnetically trapped ^7li. *Phys. Rev. A*, 59(2):1514–1516, Feb 1999.

[60] A. J. Moerdijk and B. J. Verhaar. Collisional two- and three-body decay rates of dilute quantum gases at ultralow temperatures. *Phys. Rev. A*, 53(1):R19–R22, Jan 1996.

[61] Simon L. Cornish Jacob L. Roberts Eric A. Cornell Elizabeth A. Donley, Neil R. Claussen and Carl E. Wieman. Dynamics of collapsing and exploding bosee-instein condensates. *Nature(London)*, 412:295–299, Jul. 2001.

[62] L. Tribe W. Zhang, K.-P. Marzlin and B.C. Sanders. *Directions in quantum optics: a collection of papers dedicated to the memory of Dan Walls, H. Carmichael, R. Glauber, and M. Scully(Eds.)*, 2001.

[63] Karl-Peter Marzlin.

[64] B. Podolsky A. Einstein and N. Rosen. Can quantum-mechanical description of physical reality be considered complete? *Phys. Rev.*, 47:777, 1935.

[65] M.Nielsen and I.Chuang. *Quantum computation and quantum information.* Cambridge University Press, Cambridge, UK, 2000.

[66] E. Schrödinger. Die gegenwartige situation in der quantenmechanik. *Naturwissenschaften*, 23:807–812; 823–828; 844–849, 1935.

[67] W. H. Zurek. *Phys. Today*, 44(10):36, 1991.

[68] Leggett and *et al.*. Dynamics of the dissipative 2-state system. *Rev. Mod. Phys.*, 59:1, 1987.

[69] M. Brune and *et al.*. Observing the progressive decoherence of the ιmeterɟ in a quantum measurement. *Phys. Rev. Lett.*, 77(24):4887–4890, Dec 1996.

[70] C. Monroe *et al.* Schrödinger cat superposition state of an atom. *Science*, 272:1131–1136, Jan 1996.

[71] Jonathan R. Friedman *et al.* Quantum superposition of distinct macroscopic states. *Nature*, 406:43–46, Jul 2000.

[72] Caspar H. van der *et al.* Quantum superposition of macroscopic persistent-current states. *Nature*, 290:773 – 777, Oct 2000.

[73] Markus Arndt *et al.* Wave-particle duality of C_{60} molecules. *Nature*, 401:680–682, Oct 1999.

[74] W. Wernsdorfer and *et al.*. Macroscopic quantum tunneling of magnetization of single ferrimagnetic nanoparticles of barium ferrite. *Phys. Rev. Lett.*, 79(20):4014–4017, Nov 1997.

[75] Roy J. Glauber. Coherent and incoherent states of the radiation field. *Phys. Rev.*, 131(6):2766–2788, Sep 1963.

[76] C. J. Myatt *et al.* Decoherence of quantum superpositions through coupling to engineered reservoirs. *Nature*, 403:269–273, Jan 2000.

[77] D. Leibfried1 *et al.* Creation of a six-atom 'schrödinger cat' state. *Nature*, 438:639–642, Dec 2005.

[78] Benjamin Schumacher. Quantum coding. *Phys. Rev. A*, 51(4):2738–2747, Apr 1995.

[79] Y. Nakamura *et al.* Coherent control of macroscopic quantum states in a single-cooper-pair box. *Nature*, 398:786–788, April 1999.

[80] Tobias J. Osborne and Michael A. Nielsen. Entanglement in a simple quantum phase transition. *Phys. Rev. A*, 66(3):032110, Sep 2002.

[81] D. S. Hall, M. R. Matthews, C. E. Wieman, and E. A. Cornell. Measurements of relative phase in two-component bose-einstein condensates. *Phys. Rev. Lett.*, 81(8):1543–1546, Aug 1998.

[82] Franco Dalfovo and *et al.*. Theory of bose-einstein condensation in trapped gases. *Rev. Mod. Phys.*, 71(3):463–512, Apr 1999.

[83] Y. Shin and *et al.*. Atom interferometry with bose-einstein condensates in a double-well potential. *Physical Review Letters*, 92(5):050405, 2004.

[84] S. Raghavan and *et al.*. Transitions in coherent oscillations between two trapped bose-einstein condensates. *Phys. Rev. A*, 60(3):R1787–R1790, Sep 1999.

[85] K. W. Mahmud, H. Perry, and W. P. Reinhardt. Phase engineering of controlled entangled number states in a single component bose-einstein condensate in a double well. *J.PHYS.B*, 36:L265, 2003.

[86] J. I. Cirac, M. Lewenstein, K. Mølmer, and P. Zoller. Quantum superposition states of bose-einstein condensates. *Phys. Rev. A*, 57(2):1208–1218, Feb 1998.

[87] D. Gordon and C. M. Savage. Creating macroscopic quantum superpositions with bose-einstein condensates. *Phys. Rev. A*, 59(6):4623–4629, Jun 1999.

[88] A. Sørensen and *et al.*. Many-particle entanglement with boseeinstein condensates. *Nature(London)*, 409(63):63, Jan 2001.

[89] A. Micheli, D. Jaksch, J. I. Cirac, and P. Zoller. Many-particle entanglement in two-component bose-einstein condensates. *Phys. Rev. A*, 67(1):013607, Jan 2003.

[90] J. Ruostekoski. Schrödinger cat state of a bose-einstein condensate in a double-well potential, 2001.

[91] Janne Ruostekoski and *et al.*. Macroscopic superpositions of bose-einstein condensates. *Phys. Rev. A*, 57(1):511–517, Jan 1998.

[92] Michael W. Jack and Makoto Yamashita. Bose-hubbard model with attractive interactions. *Physical Review A (Atomic, Molecular, and Optical Physics)*, 71(2):023610, 2005.

[93] J. Higbie and D. M. Stamper-Kurn. Generating macroscopic-quantum-superposition states in momentum and internal-state space from bose-einstein condensates with repulsive interactions. *Physical Review A (Atomic, Molecular, and Optical Physics)*, 69(5):053605, 2004.

[94] Diego A. R. Dalvit and *et al.*. Decoherence in bose-einstein condensates: Towards bigger and better schrödinger cats. *Phys. Rev. A*, 62(1):013607, Jun 2000.

[95] D. Jaksch, C. Bruder, J. I. Cirac, C. W. Gardiner, and P. Zoller. Cold bosonic atoms in optical lattices. *Phys. Rev. Lett.*, 81(15):3108–3111, Oct 1998.

[96] Ciobanu CV Ho TL. The schrodinger cat family in attractive bose gases. *JOURNAL OF LOW TEMPERATURE PHYSICS*, 135(3-4):257–266, May 2004.

[97] Y. P. Huang and M. G. Moore. Creation, detection, and decoherence of macroscopic quantum superposition states in double-well bose-einstein condensates. *Physical Review A (Atomic, Molecular, and Optical Physics)*, 73(2):023606, 2006.

[98] R. W. Spekkens and J. E. Sipe. Spatial fragmentation of a bose-einstein condensate in a double-well potential. *Phys. Rev. A*, 59(5):3868–3877, May 1999.

[99] L. Salasnich, A. Parola, and L. Reatto. Effective wave equations for the dynamics of cigar-shaped and disk-shaped bose condensates. *Phys. Rev. A*, 65(4):043614, Apr 2002.

[100] V. L. Ginzburg and *et al.*, 1958.

[101] A. Montina and F. T. Arecchi. Bistability and macroscopic quantum coherence in a bose-einstein condensate of ^7li. *Phys. Rev. A*, 66(1):013605, Jul 2002.

[102] C. Menotti, J. R. Anglin, J. I. Cirac, and P. Zoller. Dynamic splitting of a bose-einstein condensate. *Phys. Rev. A*, 63(2):023601, Jan 2001f.

[103] G.-B. Jo and *et al.*. Phase-sensitive recombination of two bose-einstein condensates on an atom chip. *Physical Review Letters*, 98(18):180401, 2007.

[104] Juha Javanainen and Sung Mi Yoo. Quantum phase of a bose-einstein condensate with an arbitrary number of atoms. *Phys. Rev. Lett.*, 76(2):161–164, Jan 1996.

[105] Yvan Castin and Jean Dalibard. Relative phase of two bose-einstein conden-sates. *Phys. Rev. A*, 55(6):4330–4337, Jun 1997.

[106] Wei Li, Ari K. Tuchman, Hui-Chun Chien, and Mark A. Kasevich. Extended coherence time with atom-number squeezed states. *Physical Review Letters*, 98(4):040402, 2007.

[107] Juha Javanainen and Martin Wilkens. Phase and phase diffusion of a split bose-einstein condensate. *Phys. Rev. Lett.*, 78(25):4675–4678, Jun 1997.

[108] F. Schreck and *et al.*. Quasipure bose-einstein condensate immersed in a fermi sea. *Phys. Rev. Lett.*, 87(8):080403, Aug 2001.